6. SITE 908[1]

Shipboard Scientific Party[2]

HOLE 908A

Date occupied: 11 August 1993

Date departed: 15 August 1993

Time on hole: 3 days, 3 hr, 23 min

Position: 78°23.112′N, 1°21.637′E

Bottom felt (drill pipe measurement from rig floor, m): 1284.5

Distance between rig floor and sea level (m): 10.93

Water depth (drill pipe measurement from sea level, m): 1273.6

Total depth (from rig floor, m): 1629.1

Penetration (m): 344.6

Number of cores (including cores with no recovery): 37

Total length of cored section (m): 344.6

Total core recovered (m): 313.96

Core recovery (%): 91.1

Oldest sediment cored:
Depth (mbsf): 344.6
Nature: silty clay
Earliest age: late Oligocene

HOLE 908B

Date occupied: 15 August 1993

Date departed: 15 August 1993

Time on hole: 9 hr, 15 min

Position: 78°23.125′N, 1°21.644′E

Bottom felt (drill pipe measurement from rig floor, m): 1284.0

Distance between rig floor and sea level (m): 10.96

Water depth (drill pipe measurement from sea level, m): 1273.0

Total depth (from rig floor, m): 1367.4

Penetration (m): 83.4

Number of cores (including cores with no recovery): 10

Total length of cored section (m): 83.4

Total core recovered (m): 78.01

Core recovery (%): 93.5

Oldest sediment cored:
Depth (mbsf): 83.4
Nature: silty clay
Earliest age: Quaternary

Principal results: Site 908 (proposed Site FRAM-2) was drilled on Hovgaard Ridge, which marks the northern boundary of the Boreas Basin. The ridge blocks the deep southern Fram Strait except for narrow channels that have developed between the Greenland continental margin in the West and the Svalbard continental margin in the East, where the northern end of the still active mid-ocean Knipovich Ridge is found. The site on top of Hovgaard Ridge was chosen to determine the age and lithology of sediments in basins on the ridge crest for the purpose of establishing timing and sedimentary processes immediately postdating the opening of Fram Strait and subsidence of Hovgaard Ridge. The location also was planned to be a shallow-water site to investigate the history of water mass exchange between the Arctic Ocean and the Norwegian-Greenland Sea. The age of the sedimentary units on top of the ridge was unknown.

The drilling program consisted of double or triple APC- (to refusal) and XCB-coring of the sedimentary sequence to a depth of 360 mbsf. The available seismic reflection lines established the existence of a strongly stratified, almost 200-m-thick upper sequence of sediments limited by a strong reflector marking the existence of an erosional interface on top of a small sedimentary basin. High gas concentrations and stiff sediments restricted APC-coring to the upper 100 m, and the burned-out shoe of the XCB limited total depth of penetration to 345 mbsf. The coring program was then curtailed because of the difficult stratigraphy of the uppermost sediments and the incomplete record of the entire sequence. The logging program also was limited because of the poor hole qualities around the unconformity caused by rapid swelling of formations, even after reaming.

Two major lithologic units are distinguished according to changes in composition, texture, and the occurrence of dropstones. The boundary between lithologic Units I and II is placed at 185 mbsf, where the biosilica content sharply increases.

Unit I: (0–185 mbsf, Pliocene to Quaternary): Except for a few intervals of foraminifer-bearing clayey or silty mud, which occur in the two uppermost cores, and three distinct ash layers, this unit consists entirely of siliciclastic sediments. Textural changes define a general downward trend in dominant lithology from clayey or silty muds interbedded with minor clayey silts or silty clay, toward homogeneous silty clay. Three subunits can be distinguished on the basis of the occurrence of dropstones (mainly clastic sedimentary rocks), texture, and sedimentary structures.

Unit II: (185–345 mbsf, upper Oligocene): Lithologic Unit II is distinguished by the appearance of biosilica and distinctly greater sediment lithification. The sediments consist primarily of dark olive-gray to dark grayish brown silty clays. Diatoms are the dominant biogenic component and typically constitute 8%–20% of the bulk sediment. Sponge spicules and radiolarians are lesser biogenic components together with few molluscan fragments. Bioturbation is pervasive.

Microfossils recovered reveal a discontinuous stratigraphic sequence of Pliocene to Quaternary and upper Oligocene to possibly lowermost Miocene sediments. An unconformity, clearly visible on the seismic reflection records and identified at the base of Section 151-908A-20X-5 (185 mbsf), separates relatively unfossiliferous Pliocene and Quaternary hemipelagic muds from upper Oligocene diatom-rich muds. Miocene sediments are absent at Site 908, with the possible exception of lowermost Miocene diatom-rich muds in Cores 151-908A-21X and -22X (185–206.3 mbsf). Paleomagnetic studies have yielded an interpretable polarity stratigraphy in the upper 185 mbsf, whereas the magnetostratigraphic temporal control for the sediments below the unconformity at 185 mbsf remains uncertain (but not incompatible with the established biostratigraphy).

[1]Myhre, A.M., Thiede, J., Firth, J.V., et al., 1995. *Proc. ODP, Init. Repts.*, 151: College Station, TX (Ocean Drilling Program).

[2]Shipboard Scientific Party is as given in the list of participants preceding the Table of Contents.

The sediments of Unit I are representative of the glacial Pliocene and Quaternary depositional regime in the southern Fram Strait, with little documentation of alternations between glacial and interglacial faunas and floras. Below Core 151-908A-20X the section is fossiliferous, consists of very dark gray mud(stones), and contains upper Oligocene siliceous microplankton (diatoms, rare radiolarians) and neritic to bathyal benthic foraminifers. The entire section also is rich in terrestrial organic material. Methane increased at 90–100 mbsf and the C_1/C_2 ratios decreased at 120 mbsf, but these were not considered a serious problem because they stabilized below 275 mbsf.

The Hovgaard Ridge section, including fully marine Oligocene sediments without indications of a sea-ice cover, is, at present, unique for the Arctic and subarctic Northern Hemisphere.

BACKGROUND AND OBJECTIVES

Background

The southern opening of the Fram Strait is almost completely blocked by a structural high known as the Hovgaard Ridge. It is bound to the North and South by abyssal plains, to the West by a narrow channel separating it from the Greenland continental margin, and to the East by a depression associated with the northern end of the active spreading center, the Knipovich Ridge (see Fig. 6 of "Introduction" chapter, this volume, and Frontispiece). This structural high is therefore of great importance for the current regimes in the southern Fram Strait. The temperate water masses of the West Spitsbergen Current (WSC) bypass the Hovgaard Ridge at the surface in the East. The cold and mostly ice-covered surface waters of the East Greenland Current (EGC) bypass it in the West, while important quantities of Atlantic waters are recirculated over the ridge to be advected into the EGC (see Fig. 14 of "Introduction" chapter, this volume) (Dickson et al., 1988; Bourke et al., 1987, 1988; Johannessen, 1986). Patterns of deep-water circulation are by no means as clear. In addition, the patterns are complicated by the possibility of runoff of dense brines from the adjacent shelf areas (as observed, for example, farther South on the Barents Sea shelf; Quadfasel et al., 1987).

Site 908 (see Figs. 6 and 17 of "Introduction" chapter, this volume) is located on top of the shallow Hovgaard Ridge in the northernmost Greenland Sea, in 1273.6 m of water. It is 1246 m above Site 909, immediately North of Hovgaard Ridge where the sill between the Arctic Ocean and the Norwegian-Greenland Sea is found. It is also the southernmost site of a transect through the transitional area between the Greenland Sea and the Arctic Ocean, the Fram Strait. These sites were proposed to document the evolution and post-opening tectonic subsidence of the Fram Strait, as well as the history and mode of water exchange through the northern gateway. The Fram Strait, together with the Greenland-Scotland Ridge, is one of the most important submarine topographic constrictions to global oceanic circulation. The opening of the Fram Strait is one of the necessary events for deep-water exchange between the Arctic Ocean, the Norwegian-Greenland Sea, and the Atlantic Ocean. The tectonic evolution of the Fram Strait is therefore a key component in understanding the long-term evolution of both the Northern Hemisphere and global climate change.

The evolution of the area, however, is poorly understood because of the exceptionally smooth magnetic field and lack of well-defined, magnetic seafloor spreading anomalies (see Fig. 11 of "Introduction" chapter, this volume). Furthermore, access to the area is restricted by the ice cover (see Figs. 12 and 13 of "Introduction" chapter, this volume) (Johannessen, 1986); hence, a limited amount of other geophysical and geological data exist. The existing seismic data coverage is mainly in the easternmost ice-free part of the Greenland Sea and Northwest of Svalbard (Austegard et al., in press).

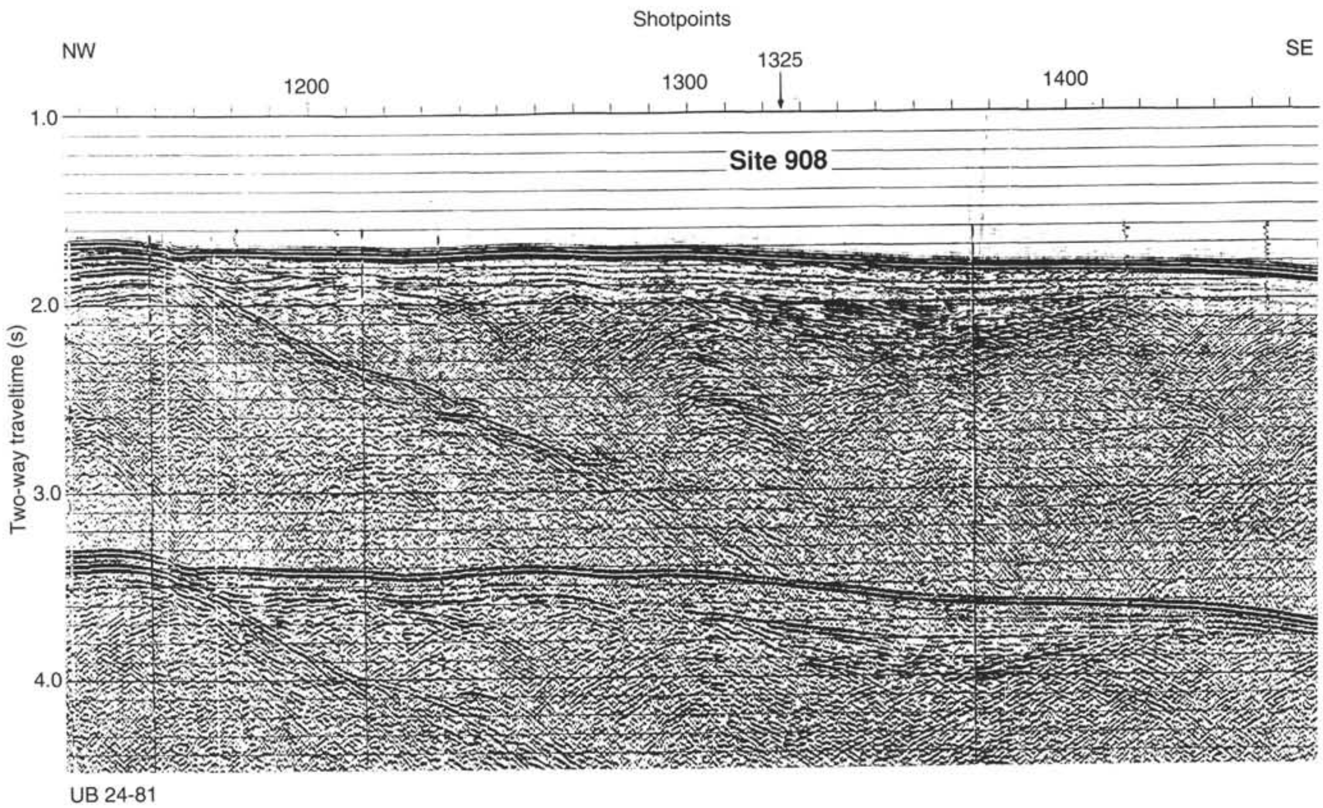

Figure 1. Multichannel seismic line UB-24-81 across the Hovgaard Ridge showing the rift basins cut by the major unconformity and overlain by a sequence of flat-lying undisturbed sediments. Site 908 is located at shotpoint 1325.

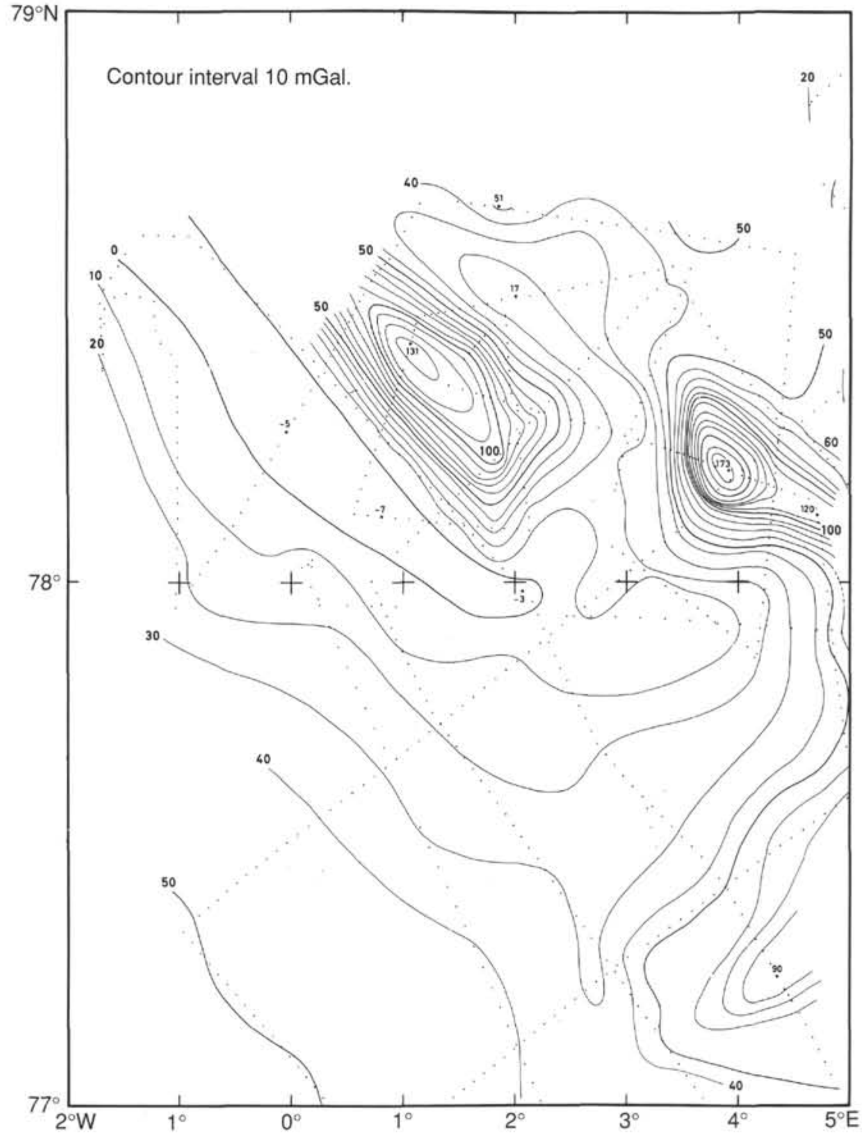

Figure 2. Free-air gravity anomaly map over the Hovgaard Ridge. Points of measurement shown by dotted lines (Eldholm and Myhre, 1977).

As a topographic high, the present-day Hovgaard Ridge is protected from a sediment influx from the surrounding margins and probably has been for some time after breakup. The ridge contains a sedimentary sequence that appears to be related to the pre-, syn-, and early post-rift evolution, indicated by small rift basins overlain by flat-lying sediments and divided by a major unconformity (Fig. 1).

The Hovgaard Ridge was originally defined by Johnson and Eckhoff (1966), who named it the Hovgaard Fracture Zone. The Southeast-trending ridge is situated just North of 78°N and consists of two morphologically different segments offset and separated by a trough. Myhre et al. (1982) and Myhre and Eldholm (1988) suggested the westernmost ridge segment to be a microcontinent cut off from the Svalbard continental margin during the opening of the Greenland Sea. The bathymetric map (Eldholm and Myhre, 1977) shows the northern element with a minimum water depth of 1171 m and the southern with a minimum of 1307 m (see Fig. 8 of "Introduction" chapter, this volume). Furthermore, the northern element appears as an elongated, flat-topped, ridge-like feature with a steep southward-facing escarpment, whereas the southern element is more like a peak. To the South the smooth abyssal plain of the Boreas Basin lies at approximately 3000–3200 mbsl and terminates abruptly against the escarpment of the northern ridge segment (see Frontispiece). The Hovgaard Ridge separates the Boreas Basin from a small basin (or terrace) to the North having an average depth of about 2500 m, the Greenland-Spitsbergen sill (see Fig. 6 of "Introduction" chapter, this volume). The difference in depth between the two basins may be explained by a considerable difference in age. Southeast of the Hovgaard Ridge, local peaks and troughs reflect the proximity to the Knipovich Ridge province. Toward the Northwest, the ridge dips gently and loses its distinct character.

In addition to a detailed bathymetric map, Eldholm and Myhre (1977) presented free-air gravity and residual magnetic maps over the area. The free-air gravity map (Fig.2) reflects the same features as the bathymetric map, with elongate anomalies of more than 100 mGal associated with the two segments. The maximum anomaly is 131 mGal over the western segment and 173 mGal over the eastern. The difference in maximum values between the two ridge segments is probably related to a difference in the densities of the underlying rocks and not to a topographic effect. Gravity modelling of the western segment by Grønlie and Talwani (1982) showed that it does not resemble a typical oceanic fracture zone.

Prominent magnetic anomalies are associated with both of the ridge segments, 663 gamma with the westernmost and 2093 gamma with the easternmost, indicating magnetic bodies within the ridges. Eldholm and Myhre (1977) pointed out that no systematic relationship exists between the free-air gravity and the magnetic maxima. The gravity and magnetic signature of the eastern segment indicates that it is probably different in crustal composition from the western ridge and might be a volcanic feature related to breakup or to the early seafloor spreading process in the area.

The oceanic crust in the Boreas Basin can be followed continuously to the Southwest-facing escarpment of the western ridge and is in places overlain with more than 1.5 s two-way traveltime (TWT) of sediments. On some of the seismic lines the uppermost sedimentary sequence in the Boreas Basin drapes onto the steep slope of the Hovgaard Ridge. On top of the ridge small infilled sedimentary basins are cut by a major unconformity, with a horizontally stratified sequence above. Because of the strong seafloor multiple, only a few short reflector segments can be identified in the deeper part of the rift basins or beneath them. On the northeastern flank, however, rotated fault blocks and sediment-filled half grabens are observed, clearly cut by an unconformity and overlain by a draping stratified sequence.

The Greenland-Spitsbergen sill basin is underlain by a complicated system of basement blocks. Some of the blocks closest to the ridge may consist of thinned continental crust, making it difficult to define the continent/ocean transition between the Hovgaard Ridge microcontinent and the oceanic crust to the North. Two measurements on top of the ridge yield values between 1.94 and 2.36 heat-flow units (HFU) (Langseth and Zielinski, 1974).

Plate tectonic reconstructions indicate that the two segments of the Hovgaard Ridge may be part of a former plate boundary, as the Knipovich spreading axis appears to be a recent feature, perhaps only 5–6 m.y. old (Sundvor and Eldholm, 1979). The complicated pattern of the present-day plate boundary, the Spitsbergen Fracture Zone system, may have extended farther South. Also, the Hovgaard Ridge could have been part of the southern boundary of a complex region that offset the spreading ridge between the southern Greenland Sea and the Arctic Ocean in Oligocene to early Miocene times.

Scientific Objectives

Site 908 was proposed on the crest of the Hovgaard Ridge as part of the northern gateway transect through the Fram Strait, between the northern Greenland Sea and the Arctic Ocean. Site 908 was planned as the southernmost tie point in this transect. Opening and subsidence of the Fram Strait is necessary for deep-water exchange between the Arctic Ocean, the Norwegian-Greenland Sea, and the Atlantic Ocean. Major objectives were to determine the age and nature of the sedimentary processes post-dating the opening of the Fram Strait and to investigate the history of water-mass exchange between the Norwegian-Greenland Sea and the Arctic Ocean.

The small sediment basins on the Hovgaard Ridge might contain sediments documenting the early history of sedimentation after the ridge subsided below shelf depth. As the southernmost site of the transect, Site 908 was chosen to enable us to document the earliest post-opening events, whereas the other sites in the transect are better suited to document the Neogene section.

OPERATIONS

Transit to Site 908 (FRAM-2)

The 729-nmi transit required 84.5 hr for an average speed of 8.6 kt. The seismic survey at Site 908 started at 2115 hr, 11 August, and covered 28 nmi in 4.6 hr at an average speed of 6.1 kt. A Datasonics 354B beacon (S/N 763, 16.0 kHz, 208 dB) was dropped at 0058 hr, 12 August, the seismic gear was retrieved, and the ship returned to location.

The ship was on location in DP mode at 0221 hr; however, the signal from the primary beacon could not be acquired. A second (original backup) Datasonics 354B beacon (S/N 785, 15.0 kHz, 208 dB) was dropped at 0309 hr, 12 August. A third (backup) Datasonics 354B beacon (S/N 751, 14.5 kHz, 208 dB) was dropped at 0408 hr, 12 August.

Hole 908A

Hole 908A was started with an advanced hydraulic piston corer/extended core barrel (APC/XCB) bottom-hole assembly (BHA). The precision depth recorder (PDR) indicated a water depth of 1286.4 mbrf, and Core 151-908A-1H, with a recovery of 5.45 m, established the water depth of Hole 908A as 1273.6 mbsl (78°23.112′N, 1°21.637′E). APC Cores 151-908A-1H through -10H were taken from 0.0 to 90.9 mbsf (Table 1), with 90.9 m cored and 91.86 m recovered (101.1% recovery). APC-coring was terminated after Core 10H because it was the third core with a partial stroke, and recovery

Table 1. Coring summary, Site 908.

Core no.	Date (Aug. 1993)	Time (UTC)	Depth (mbsf)	Length cored (m)	Length recovered (m)	Recovery (%)
151-908A-						
1H	12	0750	0.0–5.4	5.4	5.45	101.0
2H	12	0815	5.4–14.9	9.5	9.93	104.5
3H	12	0845	14.9–24.4	9.5	9.10	95.8
4H	12	0945	24.4–33.9	9.5	9.84	103.6
5H	12	1010	33.9–43.4	9.5	9.93	104.5
6H	12	1035	43.4–52.9	9.5	9.88	104.0
7H	12	1125	52.9–62.4	9.5	9.97	105.0
8H	12	1155	62.4–71.9	9.5	10.11	106.4
9H	12	1230	71.9–81.4	9.5	8.28	87.2
10H	12	1320	81.4–90.9	9.5	9.37	98.6
11X	12	1440	90.9–100.6	9.7	4.55	46.9
12X	12	1535	100.6–110.4	9.8	6.17	62.9
13X	12	1635	110.4–120.0	9.6	9.05	94.3
14X	12	1740	120.0–129.7	9.7	7.02	72.4
15X	12	1850	129.7–139.2	9.5	4.54	47.8
16X	12	2010	139.2–148.7	9.5	6.72	70.7
17X	12	2120	148.7–158.2	9.5	9.65	101.0
18X	12	2235	158.2–167.8	9.6	9.34	97.3
19X	12	2335	167.8–177.4	9.6	8.03	83.6
20X	13	0050	177.4–187.1	9.7	9.64	99.4
21X	13	0210	187.1–196.7	9.6	9.87	102.8
22X	13	0345	196.7–206.3	9.6	8.13	84.7
23X	13	0450	206.3–216.0	9.7	9.07	93.5
24X	13	0555	216.0–225.6	9.6	9.71	101.0
25X	13	0710	225.6–235.2	9.6	8.32	86.7
26X	13	0845	235.2–244.9	9.7	9.33	96.2
27X	13	1015	244.9–254.6	9.7	7.96	82.6
28X	13	1140	254.6–264.2	9.6	9.06	94.4
29X	13	1310	264.2–273.9	9.7	9.90	102.0
30X	13	1415	273.9–283.5	9.6	9.86	102.7
31X	13	1530	283.5–293.2	9.7	9.83	101.0
32X	13	1635	293.2–302.8	9.6	9.84	102.5
33X	13	1745	302.8–312.5	9.7	9.78	100.8
34X	13	1925	312.5–320.2	7.7	8.02	104.1
35X	13	2145	320.2–330.1	9.9	8.44	85.3
36X	13	2315	330.1–340.0	9.9	6.78	68.5
37X	14	0130	340.0–344.6	4.6	3.32	72.2
Coring totals				344.6	313.96	91.1
151-908B-						
1H	15	0500	0.0–3.5	3.5	3.52	100.0
2H	15	0525	3.5–13.0	9.5	2.94	30.9
3H	15	0545	13.0–22.5	9.5	9.67	101.8
4H	15	0610	22.5–32.0	9.5	9.89	104.1
5H	15	0630	32.0–41.5	9.5	9.93	104.5
6H	15	0655	41.5–51.0	9.5	9.81	103.3
7H	15	0720	51.0–60.5	9.5	9.77	102.8
8H	15	0745	60.5–70.0	9.5	8.96	94.3
9H	15	0810	70.0–75.4	5.4	5.45	100.9
10H	15	0840	75.4–83.4	8.0	8.07	100.9
Coring totals				83.4	78.01	93.5

was decreasing in the very stiff clays. Cores were not oriented because of the high latitude. The Adara temperature shoe was run on Cores 4H, 7H, and 10H and established a 55.64°C/km temperature gradient.

Cores 151-908A-11X through -37X were taken from 90.9 to 344.6 mbsf, with 253.7 m cored and 222.1 m recovered (87.5% recovery). XCB-coring was terminated when the hard formation XCB shoe packed off with clay, overheated by friction, and broke circumferentially in the threads. The cutting face was destroyed, and some metal was lost in the hole.

The hole was prepared for logging by circulating the hole clean at 344.6 mbsf, and making a conditioning trip to 83 mbsf. A bridge was tagged at 302.4 mbsf and reamed out, and the hole was cleaned out to total depth (TD). The bit was positioned at 79.33 mbsf for logging, and was spaced out to pick up to 57 mbsf to log the upper hole.

The logs were run as follows:

Log no. 1: NGT-DSI-DIT (+ TLT). Log to 277.5 mbsf in 4.0 hr.
Log no. 2: NGT-CNT-HLDT (+ TLT). Log to 229 mbsf in 3.25 hr.

The hole filled in 118.1 m in 11 hr; therefore, the pipe was run to clean out the hole again. A bridge was reamed out at 197 mbsf, and the hole was cleaned out to TD. The bit was repositioned at 1363.8 mbsl, and logging resumed.

Log no. 3: NGT-FMS. Log to 177 mbsf in 2.75 hr.

The hole continued to fill in rapidly, so logging was terminated. The hole was filled with heavy mud, and the bit cleared the seafloor at 0341 hr, 15 August, ending Hole 908A.

Hole 908B

The ship was moved 20 m North, and Hole 908B was spudded at 0452 hr, 15 August, to provide high-resolution sampling. Core 151-908B-1H established a water depth of 1273.0 mbsl. Cores 151-908B-1H through -10H were taken from 0.0 to 83.4 mbsf, with 83.4 m cored and 78.01 m recovered (93.5% recovery). APC-coring was terminated after Core 10H because it was the third core with a partial stroke. Cores were not oriented, and heat flow measurements were not taken. The bit cleared the rotary table at 1300 hr, 15 August, ending Hole 908B. All three beacons were recovered; therefore, we assumed that the first beacon was turned off inadvertently by the PDR or other ship noise.

LITHOSTRATIGRAPHY

Introduction

The 344.6-m-long section drilled at Hole 908A is dominated by unlithified fine-grained siliciclastic muds and silty clays. Except for rare lighter intervals, a dark to very dark gray color characterizes most of the section.

Two major lithologic units are distinguished by changes in composition, texture, and the presence or absence of dropstones (Table 2). The boundary between lithologic Units I and II is placed at 185 mbsf, where biosilica content sharply increases (Fig. 3). Lithification is also greater in Unit II. Lithologic Unit I is divided into three subunits according to the amount of coarse-grained terrigenous material (particularly dropstones), which is dominant in Subunit IA, common in Subunit IB, and minor in Subunit IC (Fig. 4).

Inorganic calcite-rich layers, which constitute a minor lithology, occur irregularly throughout the hole and are discussed separately at the end of the section.

Descriptions of Lithologic Units

Unit I

Sections 151-908A-1H-1, 0 cm, through 151-908A-20X-5, 150 cm, (0–185 mbsf)
Thickness: 185 m
Age: Pliocene to Quaternary

Except for the three layers of foraminifer-bearing clayey or silty mud, which occur in the two uppermost cores, and three distinct ash layers, lithologic Unit I consists entirely of siliciclastic sediments. Within this unit textural changes define a general downward trend in dominant lithology from clayey or silty muds interbedded with minor clayey silts or silty clays, toward homogeneous silty clay. Although these changes are gradational, three lithologic subunits are distinguished.

Subunit IA: Sections 151-908A-1H-1, 0 cm, through -9H-CC, (0–81.4 mbsf), and Sections 151-908B-1H-1, 0 cm, through -10H-CC, (0–83.4 mbsf)

Lithologic Subunit IA consists predominantly of clayey and silty mud, interbedded with silty clay or clayey silt (Fig. 5). Its lower boundary is defined by the presence of mud as a dominant lithology and by the concomitant downhole decrease in the number of dropstones. Minor lithologies are represented by three thin layers (20, 30, and 15 cm thick) of foraminifer-bearing muds (Sections 151-908A-1H-1, -1H-2, -2H-3, respectively), and by inorganic calcite layers.

The two dominant lithologies only differ in the amount of coarse-grained material. This coarse material is commonly either scattered in a fine-grained matrix or concentrated in pockets and layers (Fig. 6). These layers range from indistinct laminations to discrete centimeter-scale beds. Sand content primarily ranges between 5% and 25%, but fine-scale variability makes it difficult to characterize the lithology. This coarse material includes quartz and feldspar grains, mud clasts, and rock fragments. Coal fragments also were identified (see Table 9 in "Organic Geochemistry" section, this chapter). Dropstones are found in Subunit IA, either isolated in fine-grained intervals or within poorly sorted intervals (Fig. 7 and Table 3). Dropstones

Table 2. Summary of lithologic units in Hole 908A.

Unit	Dominant lithology	Interval, mbsf (thickness, m)	Age	Occurrence (core-section)
I A	Clayey mud, silty mud, silty clay; (erratic) dropstones	0–81.4 (81.4)	Quaternary–Pliocene	1H-1 to 9H-CC
I B	Silty clay and clayey silt; few (erratic) dropstones	81.4–139.2 (57.8)	Quaternary–Pliocene	10H-1 to 15X-CC
I C	Silty clay	139.2–185 (45.8)	Pliocene	16X-1 to 20X-5
II	Biosilica-bearing or biosiliceous silty clay, silty clay, and clay	185–344.6 (159.6)	late Oligocene	20X-6 to 37X-CC

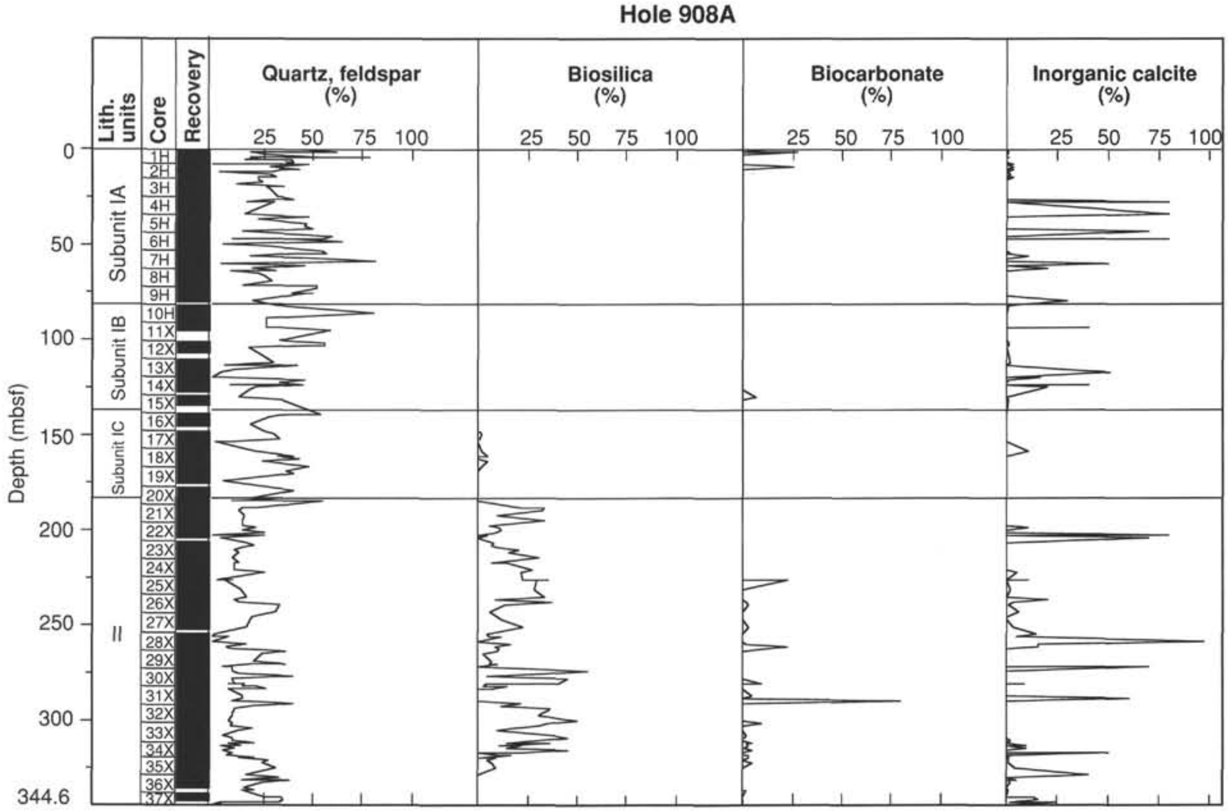

Figure 3. Lithologic units and percentages of the main components observed in smear slides from both major and minor lithologies.

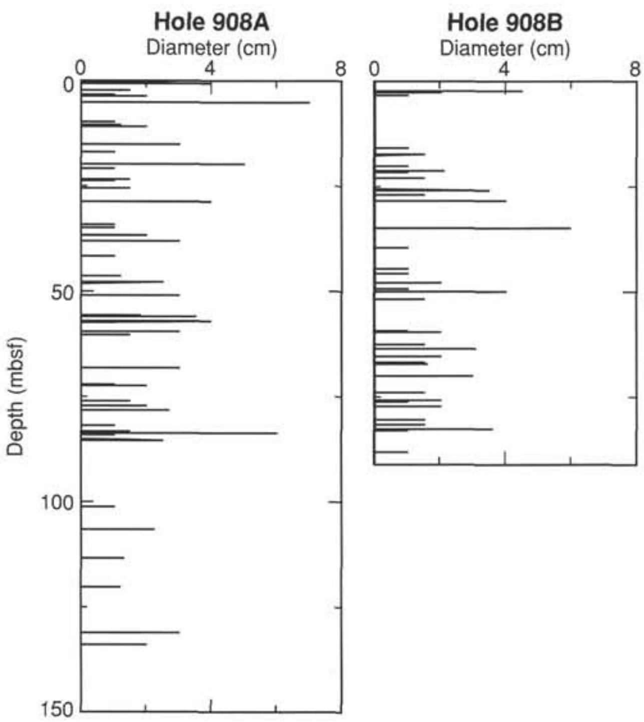

Figure 4. Depth of occurrence and diameter of erratic dropstones larger than 1 cm in Holes 908A and 908B.

consist mainly of clastic sedimentary rocks (siltstone, sandstone, shale).

No clear relationship between color and lithology is present; similar dark gray, dark brown, dark grayish brown, dark olive gray, and very dark gray colors were observed in the muds, silty clays, and clayey silts. However, color changes in the upper two cores (0–15 mbsf) occur in repetitive sequences, from 30 to 100 cm thick. Each sequence begins with a very dark gray interval above a sharp basal contact, and continues upward through a more brownish gray interval to a lighter gray top. Downhole, the brownish shades disappear, but similar sequences of changes in color value occur down to 26 m (Section 151-908A-4H-1). Below this level the sediment is dominated by uniform very dark gray.

Subunit IB: Sections 151-908A-10H-1 through -15X-CC, (81.4–139.2 mbsf)

Lithologic Subunit IB consists predominantly of silty clay and clayey silt. The sediment is largely structureless, with the exception of some burrow infillings and scattered coarse-grained pockets, mud clasts, and dropstones. Color variations are limited, and subtle, very dark to dark gray persists throughout.

Discrete layers of silty muds, 1 to 10 cm thick, constitute a minor lithology present in Subunit IB. These layers are characterized by a sharp basal contact and are largely structureless within.

Subunit IC: Sections 151-908A-16X-1 through -20X-6, (139.2–185 mbsf)

Lithologic Subunit IC is represented by a homogeneous, very dark gray silty clay. Burrows within the subunit typically are filled with friable sand or cemented with pyrite. Faint color banding is present. The bands typically include greenish color shades and contain glauconite in trace amounts.

Minor lithologies include clayey mud, volcanic ash, and silty sands. The clayey mud consists of highly bioturbated centimeter-scale layers (Fig. 8). These layers have gradational contacts at both the base and top. An ash layer (Section 151-908A-17X-4, 3–9 cm) has a sharp base and predominantly flat, colorless, glass shards. Silty sand occurs in two layers (Sections 151-908A-20X-4, 111 cm, through -20X-5, 2 cm, and Section 151-908A-20X-5, 84–150 cm).

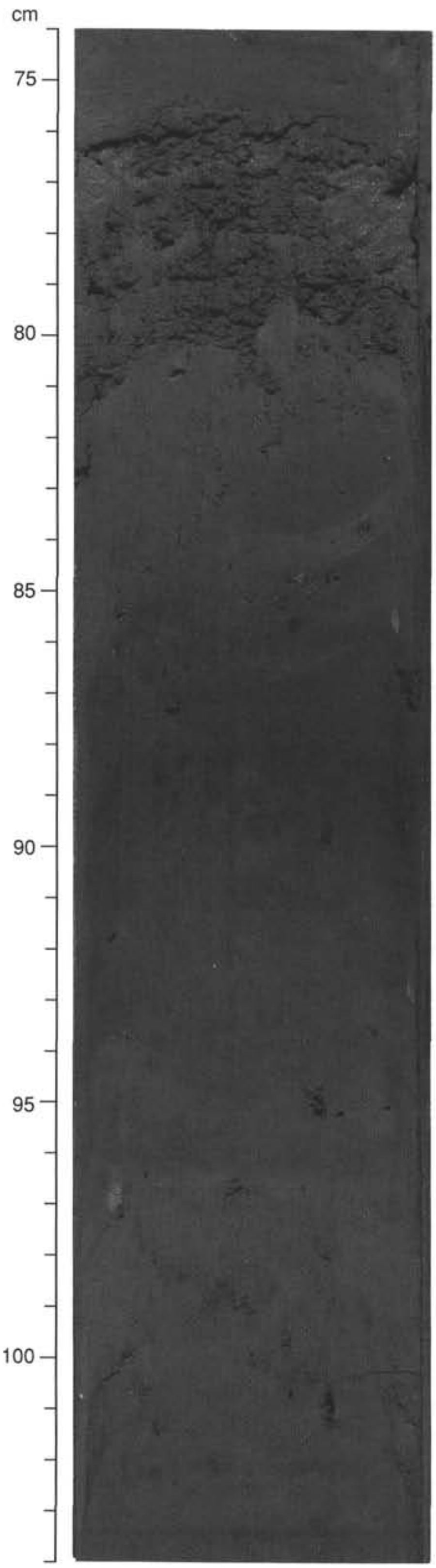

Figure 5. Interval 151-908A-6H-3, 74–104 cm; very dark gray, silty clay interbedded with dark gray silty mud. The silty mud is present in discontinuous pockets (lower part) or concentrated in a distinct layer (upper part).

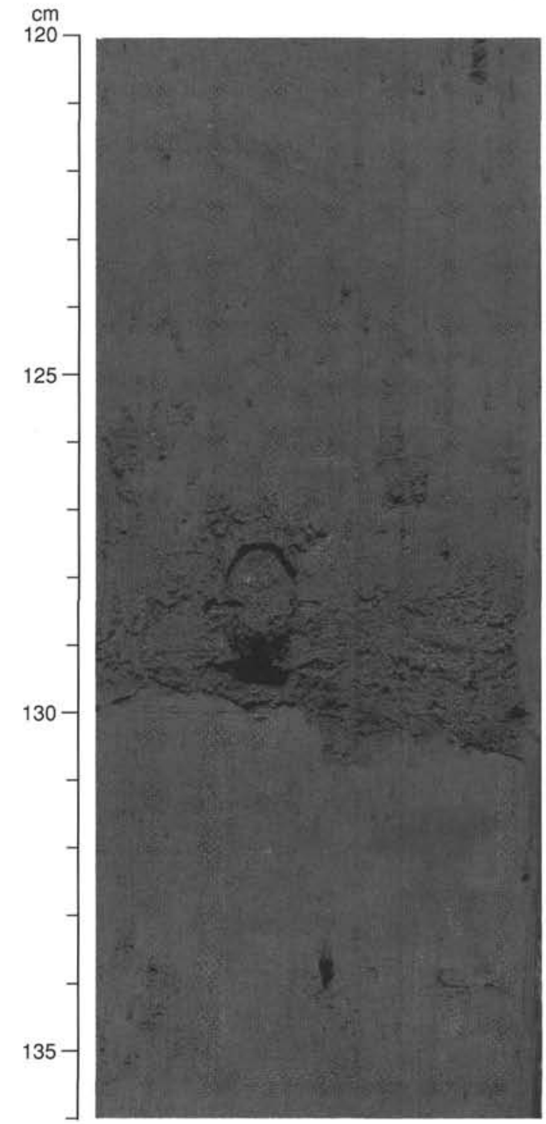

Figure 6. Interval 151-908A-3H-3, 120–136 cm; single bed of coarse sand with a sharp base and a small dropstone in its upper part. The upper contact is gradational and appears partly bioturbated.

Both layers have sharp contacts above and below, and are graded. The deeper bed is bounded at both the base and top by 2- to 4-cm-thick greenish yellow silty mud. Sediment within the layers is very dark greenish gray and contains 60%–70% glauconite. The boundary with lithologic Unit II is placed at the base of the lower silty sand interval.

Unit II

Sections 151-908A-20X-6, 0 cm, through 151-908A-37X (185–344.6 mbsf)
Thickness: 159.6 m
Age: late Oligocene

Lithologic Unit II is distinguished by the presence of biosilica and distinctly greater sediment lithification. The sediment consists primarily of dark olive gray to dark grayish brown silty clay. Diatoms are the dominant biogenic component and typically constitute between 8% and 20% of the sediment. Sponge spicules constitute another

Table 3. Depth, size, and nature of dropstones (>1 cm) recovered from Holes 908A and 908B.

Core, section, interval top (cm)	Depth (mbsf)	Diameter (cm)	Lithology
151-908A-			
1H-1, 14	0.1	3.0	Black siltstone
1H-1, 67	0.7	1.0	Sandstone
1H-1, 77	0.8	4.0	Dark sandstone
1H-2, 72	2.2	1.5	Shale siltstone
1H-3, 12	3.1	1.0	Metamorphic
1H-3, 70	3.7	2.0	Dark siltstone
1H-3, 70	3.7	1.0	Black shale
1H-3, 70	3.7	1.0	Black shale
1H-4, 45	5.0	1.0	Shale siltstone
1H-4, 48	5.0	7.0	Black shale
1H-4, 50	5.0	6.0	Black shale
2H-3, 112	9.5	1.0	Crushed clayey black shale
2H-4, 42	10.3	1.2	Black Shale
2H-4, 42	10.3	1.2	Brown quartzite
2H-4, 101	10.9	2.0	Light brown sandstone
2H-7, 52	14.9	3.0	Gray metamorphic
3H-1, 8	15.0	1.4	nd
3H-2, 63	17.0	1.0	Shale
3H-4, 24	19.7	5.0	Siltstone
3H-4, 127	20.7	1.0	nd
3H-6, 79	23.2	1.5	Sandy mudstone
3H-CC, 22	23.8	1.0	nd
4H-1, 92	25.3	1.5	Metamorphic
4H-3, 125	28.7	4.0	Black quartzite
5H-1, 24	34.1	1.0	Siltstone
5H-1, 95	34.9	1.0	Siltstone
5H-2, 111	36.5	2.0	Mud clast
5H-3, 126	38.2	3.0	Sandstone
5H-6, 10	41.5	1.0	Siltstone
6H-2, 124	46.1	1.2	Sedimentary rock
6H-3, 138	47.8	1.2	Sandstone
6H-3, 145	47.9	2.5	Carbonate
6H-5, 135	50.8	1.5	Amphibolite
6H-6, 5	50.9	1.0	Siltstone
6H-6, 14	51.0	3.0	Slate
7H-2, 134	55.7	1.8	Sandstone
7H-2, 148	55.8	1.5	Fe-rich claystone
7H-3, 6	55.9	3.0	nd
7H-3, 21	56.1	1.0	Red sandstone
7H-3, 23	57.2	4.0	Sandstone
7H-3, 133	56.1	3.5	Sandstone
7H-3, 141	57.3	1.0	Shale
7H-5, 62	59.5	3.0	Shale
7H-5, 135	60.25	1.5	Shale
8H-4, 121	68.1	1.5	Dark sandstone
8H-4, 139	68.3	3.0	Dark shale
8H-7, 62	72.0	1.0	Brown siltstone
9H-1, 63	72.5	2.0	Schist
9H-3, 109	76.0	1.5	Porphyritic basalt
9H-4, 85	77.3	2.0	Sandstone
9H-5, 48	78.4	2,7	Quartz
10H-1, 42	81.8	1.0	Sandstone
10H-2, 45	83.4	1.5	Quartzite
10H-2, 60	83.5	6.0	Basalt
10H-2, 124	84.1	1.0	Basalt
10H-3, 83	85.2	2.5	Basalt
12X-1, 43	101.0	1.0	Black coal clayey shale
12X-CC, 64	106.6	2.2	Quartzite
14X-1, 17	120.2	1.2	Red sandstone
15X-1, 114	130.8	3.0	Siltstone Eocene
15X-CC, 26	134.0	2.0	Siltstone
151-908B-			
1H-2, 62	2.1	4.5	Sandstone
1H-2, 94	2.4	2.0	Limestone
1H-3, 7	3.1	1.0	Black shale
3H-2, 30	14.8	1.0	Shale/slate
3H-3, 12	16.2	1.5	nd
3H-3, 15	18.8	1.5	nd
3H-4, 127	14.8	1.0	nd
3H-5, 79	18.8	2.1	Black shale
3H-5, 79	18.8	1.2	Black shale
3H-5, 80	18.8	1.0	Black shale
3H-5, 84	18.8	1.0	Black shale
3H-5, 90	18.9	1.0	Black shale
3H-6, 98	21.5	1.5	Black shale
4H-1, 140	23.9	2.6	Sandstone
4H-1, 143	23.9	3.5	Siltstone
4H-2, 92	24.9	1.5	nd
4H-4, 35	26.4	4.0	Siltstone
5H-1, 55	32.6	6.0	Sandstone
5H-4, 40	36.9	1.0	Basalt?
5H-7, 52	41.5	1.0	nd
6H-1, 102	42.5	1.0	nd
6H-2, 135	44.4	2.0	nd
6H-3, 143	45.9	1.0	Basaltic?
6H-4, 51	46.5	4.0	Mylonite?

Table 3 (continued).

Core, section, interval top (cm)	Depth (mbsf)	Diameter (cm)	Lithology
6H-5, 72	48.2	1.5	Sandstone
7H-3, 104	55.0	1.0	Quartz
7H-3, 144	55.4	2.0	Amphibolite
7H-5, 109	58.1	1.5	Sandstone
7H-6, 56	59.1	2.0	Siltstone?
7H-6, 69	59.2	2.8	Sandstone
7H-6, 69	59.2	3.1	Sandstone
8H-1, 32	60.8	2.0	nd
8H-2, 30	62.3	1.5	nd
8H-2, 43	62.4	1.6	Shale
8H-4, 5	65.1	3.0	nd
8H-6, 73	68.7	1.5	nd
9H-1, 64	70.6	2.0	nd
9H-1, 80	70.8	1.0	nd
9H-2, 26	71.8	2.0	Siltstone?
9H-3, 22	74.7	1.5	nd
10H-1, 48	75.9	1.5	Siltstone?
10H-2, 10	77.0	3.6	Clay/siltstone
10H-2, 43	77.3	1.0	Quartz
10H-5, 57	82.0	1.0	Coal

Note: nd = not determined.

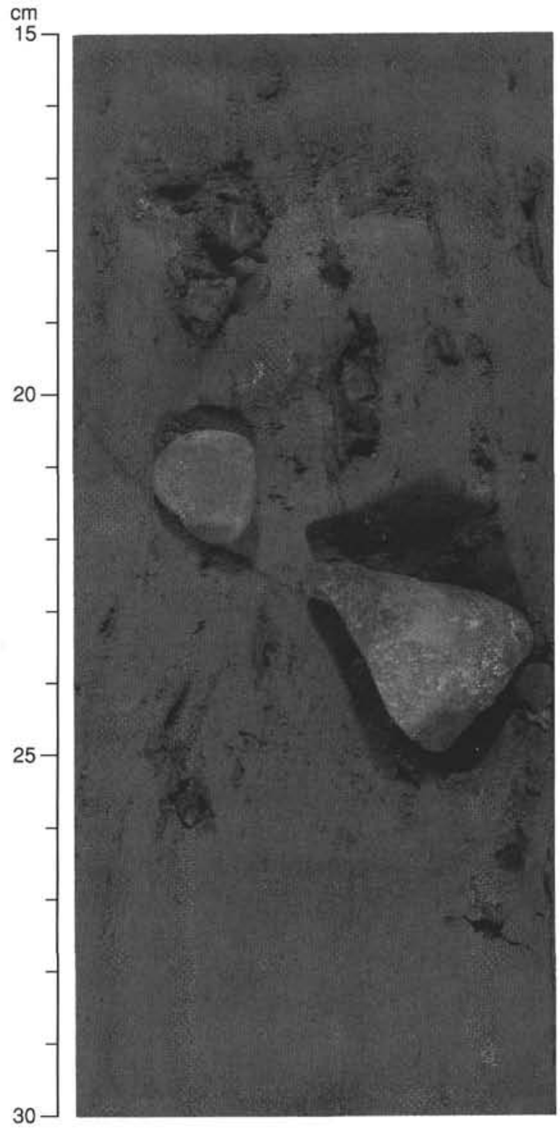

Figure 7. Interval 151-908A-7H-3, 15–30 cm; dropstones associated with granules and clay clasts within a layer of clayey mud.

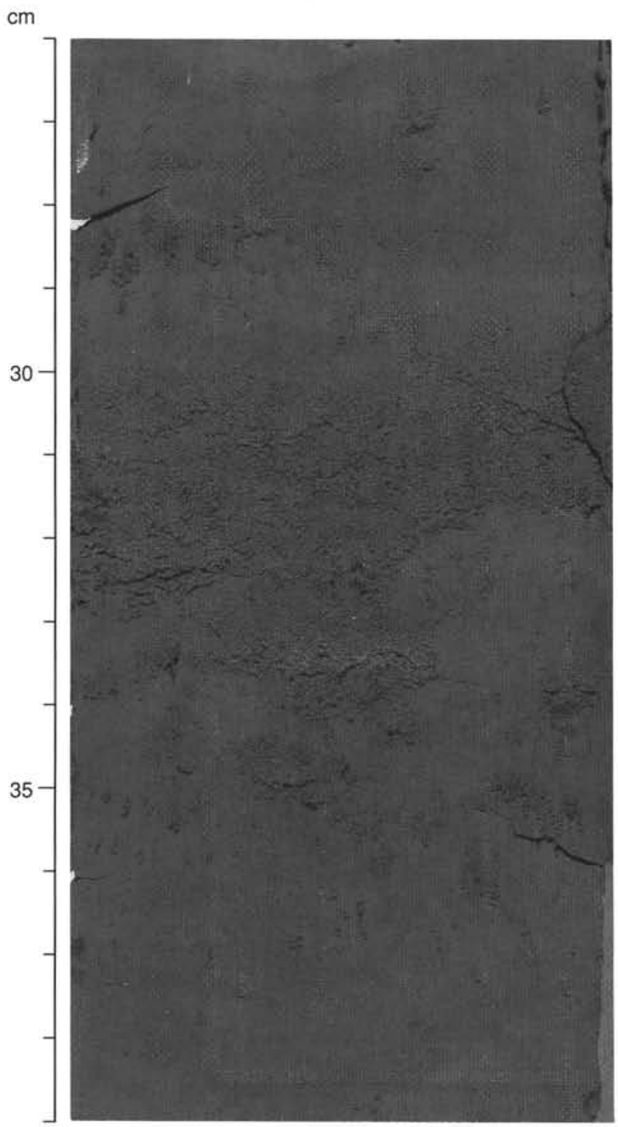

Figure 8. Interval 151-908A-18X-4, 26–39 cm; sandy mud layer with top and bottom contacts that are indistinct and bioturbated.

5%–10% of the sediment, and radiolarians are a lesser component. Molluscan fragments are also present. Variations in the biogenic content contrast with the homogeneous siliciclastic composition of the unit. Bioturbation is pervasive, resulting in a mottled appearance (Fig. 9). On a fine scale, bioturbation is apparent in discrete *Planolites* and *Chondrites* traces highlighted by color contrasts. Larger burrows are commonly filled with coarse-grained pyrite. Within some intervals, bioturbation does not obscure fine parallel laminations.

Interpretation

Lithologic Unit II

Based on the fine-grained character of the clastic fraction and the significant amount of siliceous biogenic component, lithologic Unit II is interpreted as a hemipelagic sedimentary deposit. Large fluctuations in the biogenic content demonstrate variable conditions. The common presence of pyrite indicates strongly reducing conditions in the sediments, which may partially explain the relatively high organic carbon contents preserved in this unit (see "Organic Geochemistry" section, this chapter). However, the high organic carbon and biosilica contents, along with the preservation of fine sedimentary laminations, suggest relatively low bottom-water oxygen levels at the time of deposition. Nevertheless, evidence for slight to moderate bioturbation indicates the presence of burrowers.

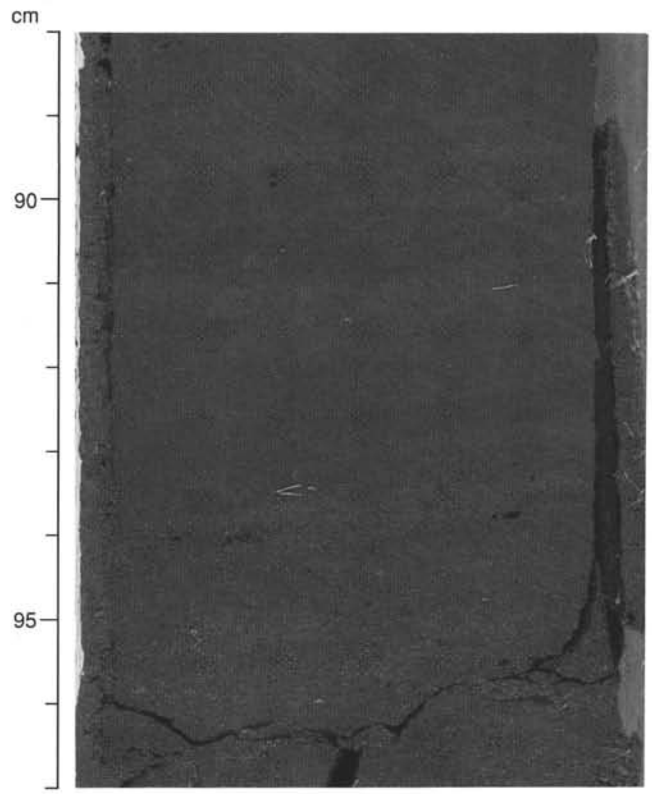

Figure 9. Interval 151-908A-25X-4, 88–97 cm; various surface textures of Unit II biosiliceous silty clay: (1) homogeneous (upper part), (2) faint color patches indicative of burrowing (middle part), (3) horizontal layering to indistinct lamination (lower part) showing coarse dark grains of pyrite and glauconite.

Alternatively, the laminations may represent fine color bandings resulting from diagenetic processes similar to those that outline burrows with diagenetic haloes. No change in texture is observed in these laminations. In certain sections, irregular, very thin color banding suggests soft sediment deformation and/or bottom current influence.

Lithologic Unit I

The base of lithologic Unit I is marked by two silty to sandy glauconitic layers, 41 and 66 cm thick. Based on the angular grain shape and the absence of very coarse clasts, these graded, sharp-based beds probably represent thick ash layers altered to glauconite. The observation of thick ash layers at this level supports the suggestion that intense volcanic activity in the Norwegian-Greenland Sea area accompanied the tectonic phase associated with the upper Oligocene to Miocene(?) unconformity (see "Biostratigraphy," "Seismic Stratigraphy" sections, this chapter).

A detailed record of the Neogene onset and subsequent history of ice-rafting is provided by sediments at this site. The presence of isolated dropstones, followed by an increase in the amount of coarse-grained siliciclastic material in the upper part of the section, clearly indicates an increase in ice-rafted material during the deposition of Unit I. Based on the absence of dropstones, Subunit IC may have been deposited before the onset of major Northern Hemisphere glaciation. The dominantly fine-grained nature of the sediment, its dark color and relative homogeneity, and evidence for the presence of benthic organisms suggest rapidly deposited terrigenous sediments.

The presence of dropstones and scattered mud clasts or granules in lithologic Subunit IB indicates that glaciers were well developed on surrounding land masses at this time. The irregular occurrence of discrete layers of silty muds is more difficult to interpret. These layers are commonly rather sharp-based but are not clearly graded, nor do they include well-defined laminations. Although these characteristics do not support their interpretation as turbidites, bioturbation may account for the lack of diagnostic turbidite features. These layers are too thin and too sparse to be related to brief increases in bottom current activity. Thus, as similar beds also are found well developed in Subunit IA, they are interpreted as related to ice-rafting processes.

The abundance of dropstones and the dominance of mud lithologies in lithologic Subunit IA indicate a marked increase in glacially derived sediment transport. Based on the composition of the dropstones and erratic clasts (sandstone, clay, coal fragments), the ice-rafted debris might have been dominantly delivered from the Fennoscandia including Svalbard and the Barents Sea shelf rather than from eastern Greenland.

Changes in colors and/or in texture that characterize this subunit must be documented in greater detail, because they are probably linked to climatic cycles. Although the sediments are largely barren of microfossils, the darker layers probably represent glacial periods, and the lighter intervals warmer periods; such dark/light cycles are well-known in Quaternary cores of the North Atlantic Ocean (Ruddiman et al., 1987). The observation that these variations tend to be more distinctive and repetitive in the upper part of the sequence needs explanation. This observation suggests that glacial-interglacial cycles became more pronounced in the late Quaternary in the Norwegian-Greenland Sea, and involved rapid transitions between states.

Inorganic Carbonate Layers

Inorganic calcite was found at several levels of the drilled sequence. It occurs rarely in low amounts (<20%) in the dominant lithologies, and in high amounts (~80%) in centimeter-scale intervals commonly marked by lighter-colored sediment. These layers range from very weakly defined intervals to beds with sharp top and basal contacts. They are commonly structureless. Within these beds, the calcite occurs as grains with a uniform size close to silt-clay boundary (~4 µm). Only one graded and laminated carbonate bed, interbedded within biosilica-bearing silty clay of Unit II (Interval 151-908A-29X-6, 25–48 cm), contains coarse carbonate bioclasts.

Previous studies in the North Atlantic Ocean have demonstrated that detricarbonate grains characterize sediments influenced by ice-rafting and/or sediment-gravity flows associated with erosion by the Laurentian ice sheet (Andrews and Tedesco, 1992). However, the lack of sedimentary structures and the uniform grain size make it difficult to invoke reworking from carbonate sequences on surrounding landmasses. On the contrary, these observations suggest a diagenetic origin, possibly the recrystallization of calcareous nannofossils. They are also found as small burrow infillings in the biosiliceous clay of lithologic Unit II, favoring the hypothesis that they resulted from recrystallization of nannofossil-rich layers.

BIOSTRATIGRAPHY

Introduction

Microfossils recovered from Site 908 on the Hovgaard Ridge reveal a discontinuous stratigraphic sequence of Pliocene to Quaternary and upper Oligocene sediments. An unconformity, identified in the base of Section 151-908A-20X-5 (185 mbsf), separates relatively unfossiliferous Pliocene and Quaternary hemipelagic muds from upper Oligocene diatom-rich muds. Miocene sediments are absent at Site 908, with the possible exception of lowermost Miocene diatom-rich muds in Cores 151-908A-21X and -22X (187.1 to 206.3 mbsf).

Biostratigraphic correlations at Site 908 are based largely on previous studies of siliceous and calcareous microfossils from ODP and DSDP sites in the Labrador and Norwegian-Greenland seas. Although general age determinations are possible, difficulties are encountered in making more precise correlations because of the use of rare marker species in biostratigraphic zonations for the region, increasing endemism at higher latitudes, generally low abundance and diversity of certain groups, and variable preservation of carbonate or silica within the sedimentary succession. Biostratigraphic zones recognized during shipboard analyses are shown in Figure 10.

Diatoms

Smear-slide analyses of all core-catcher samples and numerous shipboard samples revealed that Cores 151-908A-1H through -16X are barren of diatoms, as are all core-catcher samples from Hole 908B (Cores 908B-1H through -10H). The youngest diatom assemblage recovered at Site 908 is in Sample 151-908A-17X-4, 2–4 cm (153 mbsf). This sample, which contains few diatoms, is a few centimeters above a prominent white ash layer (Fig. 11). This glassy ash may have enriched the pore waters in silica, enhancing the preservation potential of biogenic opal in the sediments. The diatom assemblage consists of *Stephanogonia hanzawae, Thalassionema lineatum, Thalassiosira jacksonii, T. eccentrica*, and *T. oestrupii*, indicating the lower Pliocene part of the *T. kryophila* Zone. The co-occurrence of *T. jacksonii* and *T. oestrupii* implies an age range of 5.0–4.3 Ma (Bodén, 1992). This sample contains the only age-diagnostic siliceous fossils in the upper 153 m of sediment. This sample also contains reworked upper Oligocene diatoms and silicoflagellates. Diatoms are sporadic and generally poorly preserved in Cores 151-908A-18X through -20X. The assemblages in these samples consist of robust, non-age diagnostic forms, such as *Paralia sulcata* and *Stephanopyxis turris*.

Below Core 151-908A-20X a distinct change in the diatom assemblage is evident. Unlike the dominantly barren upper section, most samples from Cores 151-908A-21X (187 mbsf) through -34X (320 mbsf) contain a diverse assemblage of well-preserved diatoms, although several short barren intervals are present. This silica-rich interval is well represented in analyses of lithostratigraphy, geochemistry, physical properties, and logging (see separate sections on these topics within this chapter). Diatoms in Hole 908A show that the unconformity spans the upper Oligocene/lower lower Miocene to the lower Pliocene. No diatoms that are known to be restricted to Miocene sediments have been identified in Site 908 sediments.

The sediments below Core 151-908A-20X contain a diatom assemblage similar to those described from Site 338 of DSDP Leg 38 on the outer Vøring Plateau in the Norwegian Sea, particularly in the interval 180 mbsf through 230 mbsf at Site 338, as described by Schrader and Fenner (1976) and Dzinoridze et al. (1978). Schrader and Fenner (1976) defined four diatom zones in this interval, from the upper Oligocene *Sceptroneis pupa* Zone through the lower Miocene/upper upper Oligocene *Rocella praenitida (Coscinodiscus praenitidus)* Zone. These four zones correspond to the *Goniothecium decoratum* Zone of Dzinoridze et al. (1978).

Additional changes in the diatom assemblages of Cores 151-908A-21X through -34X are observed. The assemblage in Core 151-908A-21X is dominated by *G. decoratum* and *Stephanopyxis* species. The assemblages rich in *Sceptroneis* species are recorded in Cores 151-908A-22X through -31X, whereas the assemblages in Cores 151-908A-32X and -33X are rich in *Azpetia tuberculata* var. *atlantica* and *Cymatosira* species. Although assemblage changes between Cores 151-908A-21X and -34X are recognized, specific assignment to the zones described by Schrader and Fenner (1976) for this interval was not possible during shipboard analyses. This is because some of the zones were defined based on the occurrence of rare taxa, some of

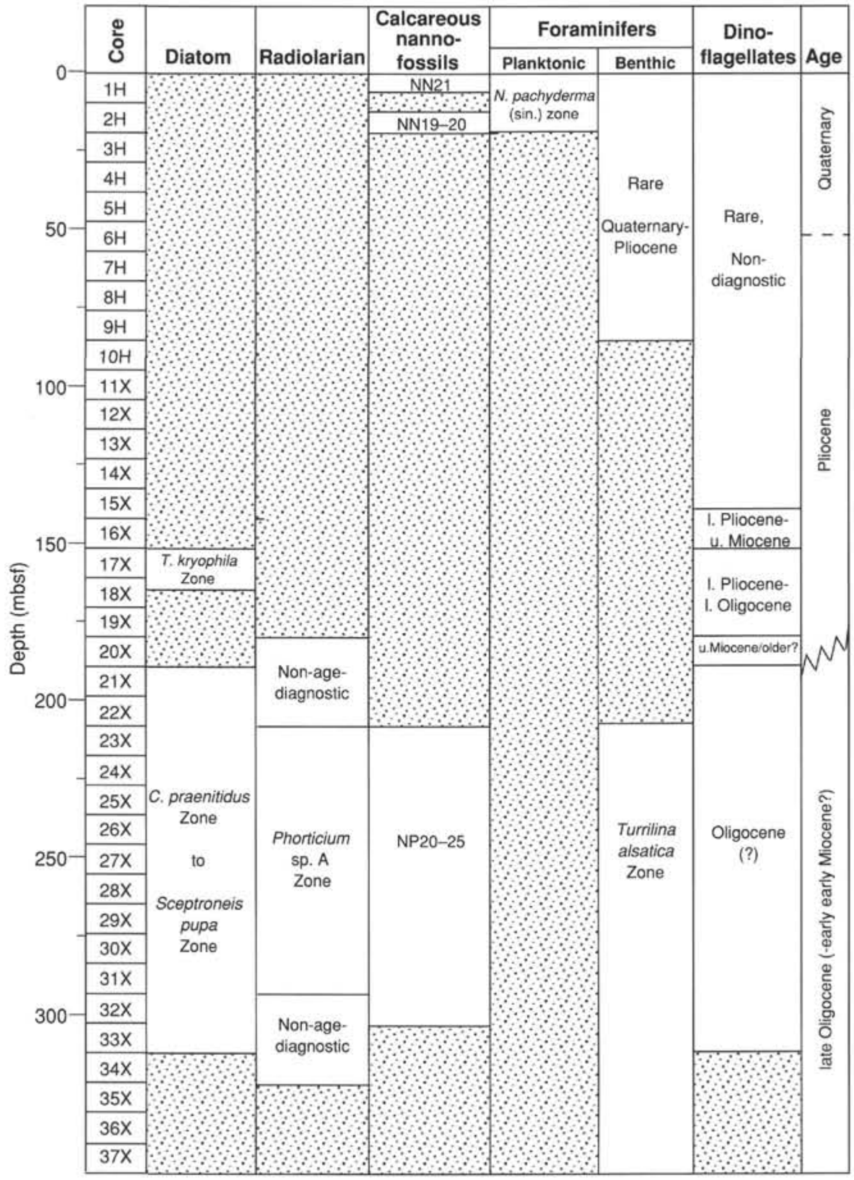

Figure 10. Biostratigraphic zonation and correlation of the different microfossil groups present at Site 908.

which have not been identified at Site 908. In fact, Fenner (1985) acknowledges that the zonal boundaries defined by Schrader and Fenner (1976) may be difficult or impossible to identify, even in their type locality.

In summary, the diatom assemblages in Cores 151-908A-20X through -34X are characterized by abundant and diverse taxa of the genera *Sceptroneis* and, to a lesser extent, *Rhabdonema*, and include many species first described by Schrader and Fenner (1976). Some cosmopolitan marker species for the upper Oligocene to lower lower Miocene are present, such as *R. praenitida, Thalassiosira* sp. aff. *T. irregulata*, and *Synedra jouseana*, although these taxa are rare. Other cosmopolitan marker taxa, such as *Rocella vigilans, R. gelida*, and *Asteromphalus symmetricus* have not been found; *R. vigilans* and *A. symmetricus* are reported as rare in Leg 38 reports (Schrader and Fenner, 1976; Dzinoridze et al., 1978). Chronostratigraphic calibration of these zones is unavailable, but an early early Miocene through late Oligocene age is consistent with all known biostratigraphic calibrations. Samples from Core 151-908A-35X contain rare and very poorly preserved diatoms of indeterminate age. Cores 151-908A-36X and -37X are barren of diatoms.

Silicoflagellates

Biostratigraphically significant silicoflagellates were noted during shipboard diatom study, though no systematic examination of silicoflagellates was performed. Ages based on silicoflagellates are not reported because only a low number of specimens were evaluated.

Radiolarians

Core-catcher samples from Cores 151-908A-1H through -37X and Cores 151-908B-1H through -10H have been examined for radiolarians at Site 908. Samples 151-908A-1H-CC through 151-908A-19X-CC and 151-908B-1H-CC through 151-908B-10H-CC are barren of radiolarians, and thus there is no Neogene record for radiolarian biostratigraphy at this site. Moderately preserved middle to upper Oligocene radiolarians are present intermittently from Sample 151-908A-20X-CC through Sample 151-908A-34X-CC. Diversity and abundances of radiolarians in these samples are very low, but at least one known and one other potentially age-diagnostic species are

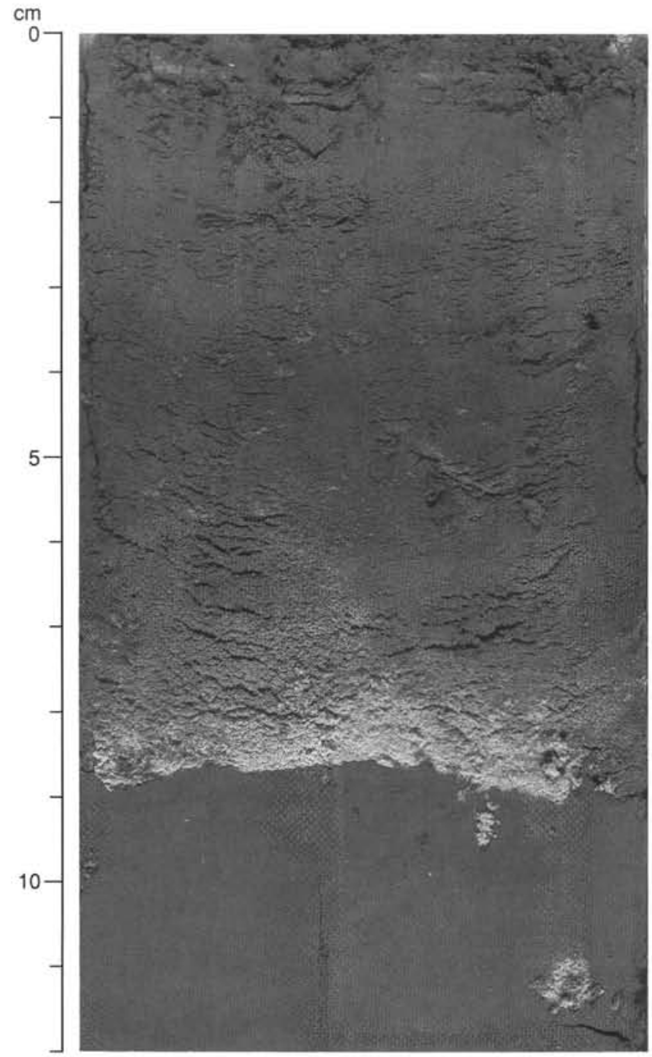

Figure 11. Silica-rich ash layer in Section 151-908A-17X-4. The dark layer overlying the ash (Sample 151-908A-17X-4, 2–4 cm) contains well-preserved lower Pliocene and reworked Oligocene diatoms, the only datable siliceous fossils in the upper 153 m of sediment.

present. Core-catcher samples taken from the lowermost cores of Hole 908A, 35X-CC through 37X-CC, are barren of radiolarians.

Relatively few species of Oligocene radiolarians from high-latitude sites have been formally described and named in the literature. Key references to Oligocene radiolarians in the Northern Hemisphere are Bjørklund (1976), Dzinoridze et al. (1978), Petrushevskaya (1979), and Lazarus and Pallant (1989). From these studies, species identifications at Site 908 include: *Phorticium* sp. A of Bjørklund (1976), *Lithelius nautiloides, Spongotrochus* sp. aff. *S. glacialis, Spongodiscus* spp., *Prunopyle* sp. C "group" and "Spumellarian gen. et sp. indet. #2" of Lazarus and Pallant (1989), *Stylodictya* spp., *Gondwanaria* sp. aff. *G. dogieli, Actinomma* spp., and *Lithomelissa* spp. The latter group of species under the genus *Lithomelissa* is a distinctive, though little described, group of radiolarians typical of high-latitude regions. *Lithomelissa* makes its first appearance in Antarctic waters in the early Oligocene (Sancetta, 1979).

Bjørklund (1976) described a low-diversity Oligocene assemblage at Site 338 (outer Vøring Plateau) in the Norwegian Sea, and recognized four biostratigraphic zones for the Oligocene. Only one age-diagnostic species, *Phorticium* sp. A, is present at Site 908, occurring in Samples 151-908A-23X-CC through -31X-CC. Although *P.* sp. A is most common in the lower to middle Oligocene *P.* sp. A Zone of Bjørklund (1976), its full range is from lower to upper Oligocene. The absence of markers for the remaining three zones may be because of the very low diversity and abundance of radiolarians at Site 908 or because of its higher latitude.

Calcareous Nannofossils

Only 15 of 42 samples examined contain calcareous nannofossils. The nannofossil assemblages have very low species diversity, and age diagnostic taxa are rare to absent.

Samples 151-908A-1H-2, 50 cm, and -1H-2, 75 cm, contain *Emiliania huxleyi* and are assigned to Quaternary Zone NN21. As in the Quaternary of Hole 907A, reworked specimens from the Cretaceous and Paleogene, such as *Watznaueria barnesae*, *Prediscosphaera cretacea*, *Micula decussata*, *Reticulofenestra reticulata*, are present in these two samples. Small *Gephyrocapsa* species (cf. *Gephyrocapsa ericsonii*) occur in Sample 151-908A-2H-CC. However, *Gephyrocapsa caribbeanica* and *G. oceanica*, which are present at Site 907, are not found in this hole. *Pseudoemiliania lacunosa*, which defines the top of the NN19/NN20 boundary, is also absent. On the basis of the occurrence of *Gephyrocapsa* spp. this sample is assigned to the Quaternary. However, species diversity is poor, and it is difficult to correlate with Martini's (1971) zonation.

Samples from 151-908A-3H-1, 15 cm, through -22X-CC are barren or have rare occurrences of nannofossils. Calcareous nannofossil assemblages below Sample 151-908A-23X-CC are characterized by an abrupt change to Paleogene specimens such as *Dictyococcites bisectus*, *Chiasmolithus altus*, *Reticulofenestra daviesii*, *R. samodurovii*, and *Zygrhablithus bijugatus*. Species diversity is low, and continuous occurrences of *Dictyococcites bisectus* in the sequence between 23X-CC and 32X-CC in addition to the presence of *Chiasmolithus altus* in Sample 151-908A-32X-CC, result in an age assignment of these samples to latest Eocene or Oligocene (NP20 to NP25). Warm-water species such as discoasters and sphenoliths, which define the upper Paleogene zones in Martini's zonation (1971), are not found in these samples. As a result, correlation with the Martini zonation is difficult at this site.

Planktonic Foraminifers

All core-catcher samples from Holes 908A and 908B were processed and examined for planktonic foraminifers. All samples are barren, with the exception of core-catcher samples from Cores 1H and 2H of Holes 908A and 908B. These sections contain *Neogloboquadrina pachyderma* sin., suggesting an age assignment of Quaternary. Ten additional samples were collected from carbonate-rich intervals within Cores 908A-1H and 908A-2H for shipboard analyses. High abundances of *N. pachyderma* sin. in Samples 151-908A-1H-1, 43–46 cm, 151-908A-1H-2, 67–69 cm, and 151-908A-2H-3, 135–139 cm, suggest interglacial conditions. Other samples between these contain only rare specimens of *N. pachyderma* sin., which are typical of more glacial conditions.

Benthic Foraminifers

In the upper 10 core catchers of Holes 908A and 908B, benthic foraminifers are rare and consist of scattered occurrences of Pliocene and Quaternary species. Beneath the upper interval, Samples 151-908A-11X-CC through -22X-CC were barren of benthic foraminifers but contained abundant sponge spicules and ice-rafted debris. Pyritized burrows were found in Samples 151-908A-18X-CC and -19X-CC.

Benthic foraminifers first appear commonly in Sample 151-908A-23X-CC. From -23X-CC through -37X-CC a mixed calcareous and agglutinated assemblage occurs, including *Cibicides grims-*

dalei, *Turrilina alsatica*, *Cyclammina* spp., *Haplophragmoides* spp., and *Spiriloccamina* sp. These species are common in Oligocene deposits of the North Sea (King, 1983), the Vøring Plateau (Osterman and Qvale, 1989), the Labrador Sea (Miller et al., 1982) and the Bay of Biscay (Miller, 1983). The common appearance of *T. alsatica* in the lower part of the hole suggests low to intermediate oxygen in the bottom waters at this time (Kaiho, 1991).

Agglutinated foraminifers become more abundant in the lowermost part of Hole 908A from Samples 151-908A-30X-CC through -37X-CC. In the Labrador Sea the last occurrence of *Cyclammina* spp. and *Rhizzamina* and the first increase in biosiliceous microfossils are used to mark the Eocene/Oligocene boundary (Kaminski et al., 1989). Similar conditions are found at the base of Hole 908A; however, the faunal change seen in the Labrador Sea is most likely time-transgressive, and agglutinated species were observed in Oligocene sediments of Leg 104 (Osterman and Qvale, 1989).

Palynology

Core-catcher samples from Cores 151-908A-1H through -21X, -23X through -27X, and -29X, -31X, -33X, and -35X were processed for palynomorphs. No samples from Hole 908B were processed. All processed samples contain abundant amorphous organic matter, plant debris, common spores and gymnosperm pollen, and some angiosperm pollen. Dinoflagellate cysts are rare in all samples, and are commonly broken or obscured by debris; therefore, many identifications of taxa are tentative.

Samples 151-908A-1H-CC through -15X-CC contain very rare, non-age-diagnostic dinoflagellate species. Sample 151-908A-16X-CC contains *Selenopemphix dioneaecysta*, which has a range of upper Miocene to lower Pliocene at Site 646 in the Labrador Sea (Head et al., 1989a). Cores 151-908A-17X-CC through -19X-CC contain specimens tentatively assigned to *Melitasphaeridium choanophorum*, which ranges from lower Oligocene to lower Pliocene (Powell, 1992). In addition, Sample 151-908A-19X-CC contains a possible specimen of *Cyclopsiella elliptica*, which ranges from lower to upper Miocene in the Norwegian Sea (Mudie, 1989), and Samples 151-908A-19X-CC and -20X-CC contain specimens of *Palaeocystodinium* sp., which indicates an age of no younger than early late Miocene (Head et al., 1989c). Sample 151-908A-18X-CC contains a reworked specimen of *Wetzeliella articulata* (range Eocene to lower Oligocene; Powell, 1992). This occurrence means that the specimens of *C. elliptica* and *Palaeocystodinium* sp. in Samples 151-908A-19X-CC and -20X-CC also could be reworked; therefore, a definite age assignment of these two samples is not possible without further study. Other taxa observed from Samples 151-908A-15X-CC through -20X-CC are: *Tectatodinium* sp., *Spiniferites* sp. cf. *S. elongatus*, *Operculodinium* sp., *Impagidinium* sp., *Selenopemphix nephroides*, *Spiniferites* sp., *Lejeunecysta* sp. cf. *L. tenella*, *Lejeunecysta* sp., and *Achomosphaera* sp.

Core-catcher Samples 151-908A-21X-CC and -24X-CC contain *Svalbardella* sp. cf. *S. cooksoniae*. *S. cooksoniae* has its last occurrence in lower Oligocene (Powell, 1992); however, the genus *Svalbardella* apparently ranges into the upper Oligocene (Head and Norris, 1989) except for a possible middle Miocene occurrence of this genus in the Norwegian Sea (Manum, 1976). *Deflandrea* sp. cf. *D. phosphoritica* occurs in Sample 151-908A-24X-CC, and questionable *Chiropteridium* sp. occurs in Samples 151-908A-27X-CC and -29X-CC. These taxa range no higher than upper Oligocene (Powell, 1992). Finally, Sample 151-908A-33X-CC contains *Cordosphaeridium* sp. cf. *C. cantharellum* and *Distatodinium paradoxum*. The former ranges from middle Eocene to lower Miocene, whereas the latter ranges from middle Eocene to middle Miocene (Powell, 1992). Although all species are rare and many species identifications are tentative, the overall assemblage from Samples 151-908A-21X-CC through -35X-CC suggests an Oligocene age. Other taxa observed in the lower part of Hole 908A are *Palaeocystodinium* sp., *Selenopemphix* sp., *Deflandrea* sp., *Lejeunecysta* sp., and *Achomosphaera* sp.

Biostratigraphic Synthesis

Biostratigraphic data from Site 908 reveal a 185-m-thick succession of sparsely fossiliferous Quaternary and Pliocene hemipelagic muds overlying an unconformity, which is underlain by upper Oligocene muds rich in biogenic silica.

Calcareous microfossils (calcareous nannofossils and foraminifers) are relatively common constituents only in Cores 151-908A-1H, 151-908A-2H, 151-908B-1H, and 151-908B-2H, representing the youngest Quaternary sediments at Site 908. Overall, carbonate material is scarce in the upper cores of both Holes 908A and 908B, and siliceous microfossils are not present. Rare occurrences of Pliocene to Quaternary benthic foraminifers continue to the base of Core 151-908B-9H (81.4 mbsf). Below this level, age-diagnostic microfossils are absent to a depth of 139.2 mbsf (top of Core 151-908A-16X).

A single dinoflagellate marker taxon, *S. dioneaecysta*, is present in Sample 151-908A-16X-CC (148.7 mbsf), which provides an age of late Miocene to early Pliocene. In Section 151-908A-17X-4, a diatom assemblage consisting of *S. hanzawae*, *T. jacksonii*, *T. eccentrica*, and *T. oestrupii*, indicates the lower Pliocene *T. kryophila* Zone. Cores 151-908A-18X through -20X contain only poorly preserved, fragmented or non-age-diagnostic diatoms and radiolarians, in addition to a dinoflagellate assemblage that includes possibly reworked specimens and the long-ranging species (lower Oligocene to lower Pliocene) *M. choanophorum*.

An unconformity within the base of Core 151-908A-20X or the uppermost part of Core 151-908A-21X is indicated by an abrupt change in floral composition and age, and by the high abundance of reworked specimens in Core 151-908A-21X. Section 908A-21X-1 contains an upper Oligocene (to lower lower Miocene) diatom assemblage characterized by the species *G. decoratum*. Oligocene dinoflagellates also appear in this core, represented by the genus *Svalbardella*. Upper Oligocene radiolarians (*Phorticium* sp. A of Bjørklund, 1976), calcareous nannofossils, and benthic foraminifers appear in Core 151-908A-23X. Thus, at the level of the unconformity, the biostratigraphic data indicate that all or nearly all of the Miocene is absent at Site 908.

In general, Oligocene siliceous microfossils and dinoflagellates continue downhole to the base of Core 151-908A-33X (312.5 mbsf); calcareous and agglutinated benthic foraminifers of the Oligocene *T. alsatica* Zone continue to the bottom of Hole 908A (344.6 mbsf). No sediments older than late Oligocene can be confirmed at this site on the basis of shipboard analyses.

PALEOMAGNETICS

Shipboard paleomagnetic studies performed at Site 908 followed the methods described in the "Explanatory Notes" chapter (this volume). The prime objective of these studies was to recover from the core a magnetostratigraphic record that could provide a chronostratigraphic framework for the sediments of Site 908. This objective was met in the upper part of the cores; however, the temporal control for the sediments deeper than 187 mbsf remains a bit uncertain.

General Magnetic Character of the Site 908 Sediments

The variation in intensity of the natural remanent magnetization (NRM) of the sediments recovered at Site 908 reflected the major lithostratigraphic divisions encountered in the cores. The NRM of sediments from the top half of Hole 908A (0–185 mbsf) and all of Hole 908B (0–83.4 mbsf) was consistently high (~10^{-2} Am^{-1}) and re-

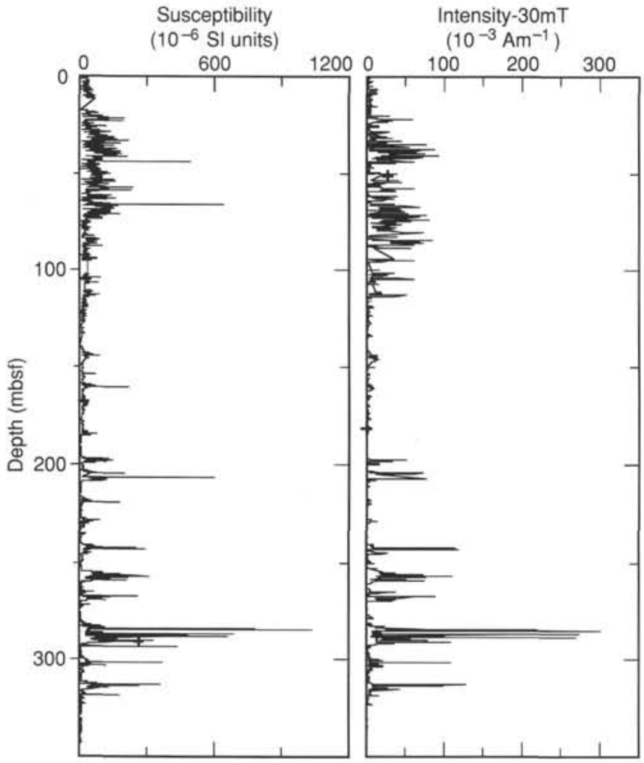

Figure 12. Depth profiles of whole-core magnetic susceptibility and NRM intensity after 30-mT AF demagnetization at Hole 908A. The unconformity between upper Oligocene and Pliocene strata occurs at about 185 mbsf.

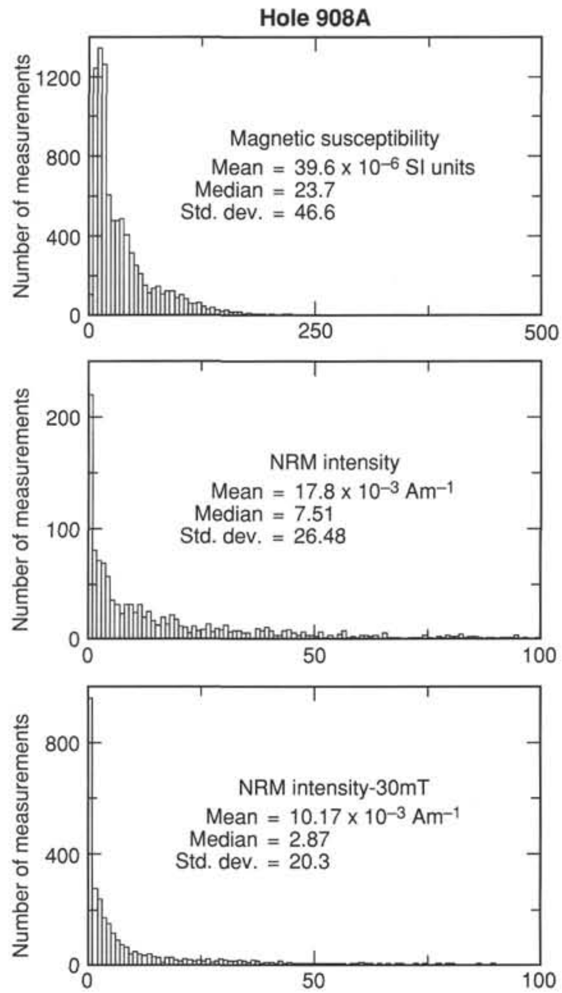

Figure 13. The distributions of magnetic susceptibility values from the whole-core multi-sensor track, NRM intensity, and NRM intensity after 30-mT demagnetization.

mained easily measurable after AF (alternating field) demagnetization to 30 mT (NRM_{30}) (Fig. 12). Below the unconformity defined on the basis of seismic, lithologic, and biostratigraphic criteria at 185 mbsf in Hole 908A, the character of the NRM changes significantly. The NRM of sediments above the unconformity of Hole 908A is generally quite low except for thin, isolated spikes of quite high NRM intensity (~3×10^{-1} Am^{-1}). These spikes in NRM intensity coincide with similarly thin spikes of susceptibility (up to ~10^{-3} SI as measured on whole cores in the multi-sensor track system) and are generally associated with the occurrence of coarse-grained ice-rafted debris (IRD) or tephra layers enriched in opaque minerals (see lithologic descriptions). The distribution of NRM intensity before and after a 30-mT demagnetization treatment (Fig. 13) suggests that many of the carriers of the high NRM intensities have relatively low coercivities, and the distribution of susceptibility values (Fig. 13) is consistent with the notion that these low-coercivity and high-NRM-intensity carriers also are responsible for the magnetic susceptibility peaks.

AF Demagnetization Behavior

Detailed progressive AF demagnetization experiments were conducted on a group of seven discrete pilot samples with peak demagnetizing fields ranging up to 80 mT (Fig. 14). These preliminary experiments indicate the NRM is carried by a fairly high coercivity material with a median destructive field generally at least 20 mT, and in many cases as large as 30 mT. AF demagnetization on discrete samples also indicates that the NRM of the cores sometimes contains spurious components, which were largely removed by AF demagnetization to 30 mT; however, in many of the discrete samples AF demagnetization yielded a simple univectoral decay to the origin. The magnetic polarity stratigraphy of the Hole 908A and 908B cores was interpreted from the inclination of the NRM after a 30-mT treatment.

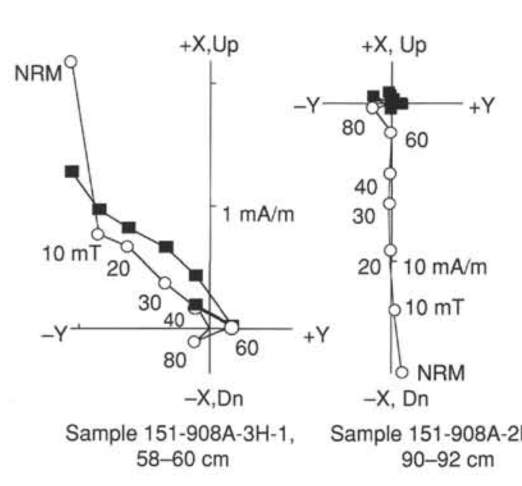

Figure 14. AF demagnetization diagrams for two discrete samples from Cores 151-908A-3H (reversed polarity characteristic magnetization) and 151-908A-2H (normal polarity characteristic magnetization). Solid squares = projection onto the horizontal plane; open circles = projection onto the vertical plane parallel to the split face of the core.

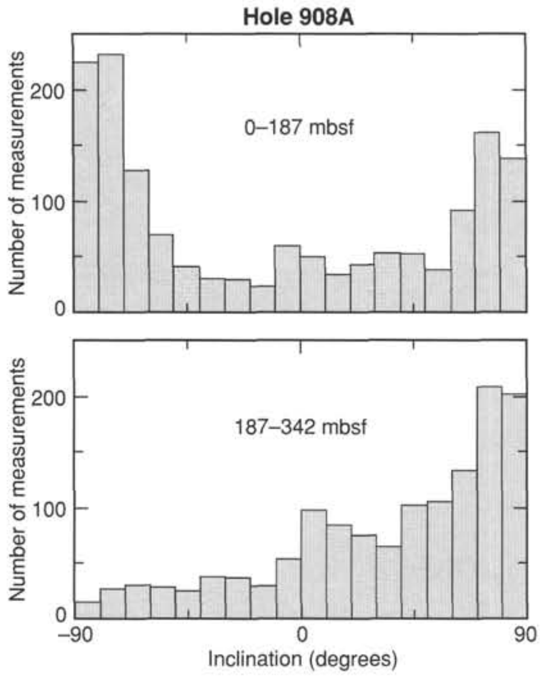

Figure 15. Distribution of inclination values after 30-mT demagnetization treatment.

Inclination Record

The NRM_{30} inclination measured in cores from Hole 908A above the unconformity at 185 mbsf is highly bimodal in distribution, having two peaks centered between plus and minus 75° (Fig. 15). We interpret these two populations of NRM_{30} inclinations as normal and reversed polarity characteristic remanent magnetizations. Numerous shallow and intermediate inclinations were observed in the record from Hole 908A, and to a lesser extent Hole 908B; thus, the inclination record from Site 908 is not as decidedly bipolar as the Site 907 result. The common occurrence of shallow inclinations could indicate a partial record of geomagnetic secular variation in some rapidly deposited lithozones from the upper 150 mbsf of Site 908 (see the "Sedimentation Rates" discussion below). However, these shallow inclinations are more likely acquired during coring and shipboard processing of the core due to spurious components of viscous remanent magnetization or the result of mechanical disturbance of the soft sediments. The preponderance of intermediate inclinations comes from below the unconformity encountered at 185 mbsf in Hole 908A and contributes to the problematic interpretation of the magnetostratigraphy of the bottom portion of Hole 908A.

The high degree of penetrative deformation that the sediments have suffered during the APC process most likely has disturbed the orientation of the magnetic grains that carry the magnetostratigraphic record. In almost all of the APC cores, originally planar bedding surfaces have been deformed into near conical forms due to large shearing forces along the cylindrical inside surface of the core liner. This style of deformation has been particularly intense in Holes 908A and 908B, probably because of the high clay content of the sediments. In some instances, these conical bedding forms were stretched over an interval of more than 20 cm. To mitigate the effect of this coring disturbance on the magnetostratigraphic record, we collected discrete paleomagnetic samples (one per 1.5-m core section) from the center of the working half of these cores, which presumably include some of the least deformed sediments. Shore-based measurements of these sediments might resolve some of the ambiguities in magnetostratigraphic interpretation of the APC cores at Holes 908A and 908B.

Similarly, the study of discrete samples from XCB cores in Hole 908A might improve the magnetostratigraphic record from those cores (Cores 151-908A-11X through -37X), which is probably degraded because of the formation of core "biscuits" during the XCB process. For much of the interval cored using the XCB tool, the recovered core consisted of 25%–50% (visually, by volume) churned up sediment debris and only 75%–50% intact cylinders of sediment, which in an additional complication, have rotated with respect to one another along the axis of the core. Discrete samples should offer some improvement over the pass-through record of the lower portion of Hole 908A by eliminating the contribution from the matrix that surrounds the "biscuits," as well as isolating the signal from one intact and contiguous volume of sediment.

Magnetic Polarity Stratigraphy

Identification of magnetozones in Holes 908A and 908B was based entirely on inclination data observed after a 30-mT AF demagnetization. The core orientation tool was not deployed at this site because of the high latitude and the expectation that the magnetic declination record would contain little information. Magnetozones were identified on the basis of a coherent sequence of steep (>+60°) positive (normal polarity) or steep (<–60°) negative (reversed polarity) inclinations, which spanned more than 20 cm (two independent pass-through measurements) of the core. Several intervals have complicated inclination signals, which are identified in Figure 16 by gray zones in the polarity column. These thin zones of anomalous inclinations might have some regional or geomagnetic significance because, in the upper 83 m of the Site 908 cores, where Holes 908A and 908B overlap stratigraphically, several of these zones are observed in both cores. We have identified these as inclination perturbations in Figure 16, but they are not used as chronostratigraphic calibration points in any subsequent analysis.

Correlation with Geomagnetic Polarity Time Scale

In Figures 16 and 17, and Table 4, we propose a correlation of the magnetozones identified at Site 908 with the recent geomagnetic polarity time scale (GPTS) of Cande and Kent (1992). The major magnetozones that we have identified in both holes include the top of the Matuyama (C1r.t) identified at 34.4 mbsf in Hole 908A and at 32.4 mbsf in Hole 908B, the top of the Jaramillo (C1r.1n.t) identified at 48.2 mbsf in Hole 908A, and at 47.0 mbsf in Hole 908B. The records from the two holes are complementary and give us some confidence in the placement of the Brunhes/Matuyama boundary in the positions indicated, despite the noise of portions of each record (e.g., Core 151-908A-4H is noisy and of indeterminate polarity, whereas Core 151-908B-4H is more easily interpreted as normal polarity). As noted at Site 907 and in the work of Bleil (1989), the inclination records of the Brunhes and upper Matuyama magnetozones are variable and have several intervals of anomalous inclination that apparently correlate between cores. In addition to the major chronozones identified in both Holes 908A and 908B, we have identified the Olduvai subchronozone (C2n.t at 95.3 mbsf) and the Gauss (C2An.1.t at 163.4 mbsf) in the bottom portion above the unconformity of Hole 908A. This identification of magnetozones infers a late Pliocene age for the sediments just above the unconformity at 185 mbsf.

On the other hand, diatom biostratigraphy suggests an early Pliocene age for Core 151-908A-17X at about 155 mbsf (see "Biostratigraphy" section, this chapter). This age is inconsistent with interpretation of the magnetostratigraphy presented above. At face value this age would suggest that the normal polarity zone between 160 and 180 mbsf is correlative to the top of C3n and that one normal polarity magnetozone was missing in the overlying stratigraphic section; however, no obvious hiatuses are described in that section, and pinpointing the missing section is difficult.

The deep half of Hole 908A, (below 185 mbsf) which is largely of late Oligocene age according to biostratigraphic evidence, yields a noisy inclination record with a general bias toward steep downward directions, except for two intervals having generally upward inclinations (200–210 mbsf and 320–360 mbsf). Two hypothetical magne-

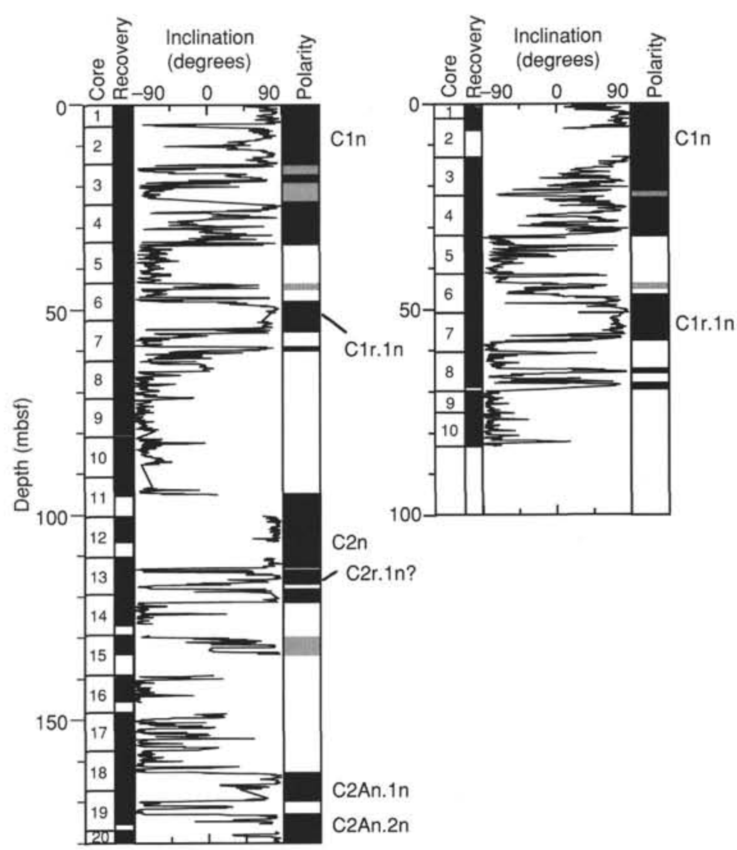

Figure 16. The magnetic polarity stratigraphy (Table 4) of the upper portion of Hole 908A (left) and all of Hole 908B (right). For each hole, the core boundaries and recovery (black indicates the thickness of the recovered core) are indicated on the left, the depth profile of inclination from pass-through measurements after 30-mT AF demagnetization is plotted in the center, and the interpreted magnetozone boundaries are indicated on the right. (Black = normal polarity; white = reversed polarity; gray = indeterminate polarity).

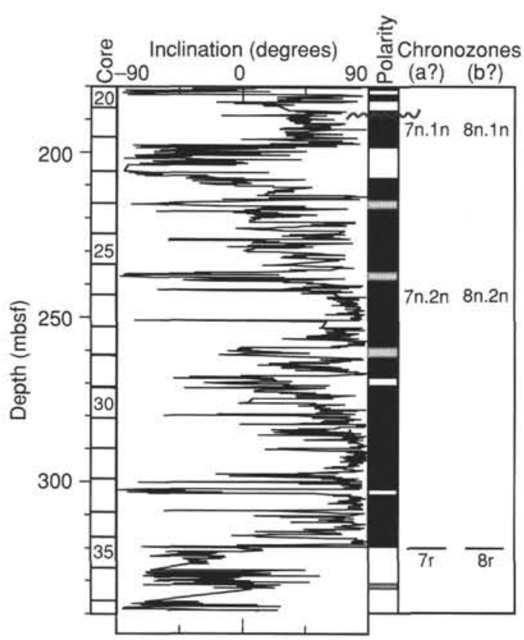

Figure 17. The depth profile of inclination from pass-through measurements after 30-mT AF demagnetization from the lower portion of Hole 908A. Core boundaries are indicated to the left of the inclination graph, and the interpreted magnetic polarity stratigraphy is indicated to the right of the inclinations (Black = normal polarity; white = reversed polarity; stippling = indeterminate polarity). The wavy horizontal line indicates the position of the unconformity defined on the basis of seismic, lithologic, and biostratigraphic criteria.

Table 4. Depth in Holes 908A and 908B and preliminary ages deduced from the magnetostratigraphy.

Depth (mbsf)	Age (Ma)	Chron
Hole 908A		
0	0	
		C1n
34.45	0.78	
48.15	0.984	
		C1r.1n
55.85	1.049	
95.3	1.757	
		C2n
121.75	1.9833	
163.35	2.6	
		C2An.1n
Hole 908B		
0	0	
		C1n
32.35	0.78	
46.95	0.984	
		C1r.1n
57.85	1.049	

tozone solutions are offered in Figure 17. These solutions, which both suggest fairly high deposition rates during the late Oligocene, are by no means unique. However, the presence of normal and reversed polarity with a bias toward normal polarity is entirely consistent with the GPTS for the late Oligocene (Cande and Kent, 1992).

In summary, the paleomagnetic analysis of cores from Site 908 yields a credible correlation to the GPTS for the stratigraphic section above the unconformity at 185 mbsf. For the interval between 0 and 100 mbsf, the comparison between Holes 908A and 908B provides a valuable opportunity to test the robustness and persistence of some of the indeterminate inclination zones so as to establish a satisfactory correlation to the GPTS. Below the unconformity at 185 mbsf, the correlation to the GPTS is entirely speculative at present, but not inconsistent with independent biostratigraphic constraints. The very low NRM intensities in the bottom of Hole 908A and the common occurrence of iron sulfides and other opaque minerals in this section complicate, perhaps fatally, the isolation of a magnetostratigraphically useful characteristic remanent magnetization. Paleomagnetic study of the discrete samples from this interval, as well as the upper core, could clean up some of the spurious inclinations related to deformation during the APC and XCB processes, and this is likely a worthwhile avenue for further work.

Sedimentation Rates

The preferred depth-age model implied by the correlations expressed in Figure 18 suggests fairly constant net sedimentation rates of about 60 m/m.y. for the upper Pliocene and Quaternary. If we interpret the normal polarity zone between 160 and 180 mbsf as C3n, as the diatom data suggest, and presume that the Jaramillo (C1r.1n) is not preserved in this section, the implied sedimentation accumulation rates are lower and much more variable (Fig. 18). For the Oligocene part of Hole 908A, a sedimentation rate of approximately 270 m/m.y. is implied in the hypothetical age models as defined by Figure 18. However, this model remains speculative at present.

Conclusions

Shipboard paleomagnetic studies of cores from Holes 908A and 908B have yielded an interpretable polarity stratigraphy in the upper 180 mbsf of these holes; however, drilling deformation of the clay-rich sediments complicates the interpretation. Preliminary identification of the Brunhes/Matuyama boundary and Jaramillo subchronozone in Holes 908A and 908B indicates sedimentation rates on the order of 60 m/m.y. (Fig. 18). Magnetostratigraphic temporal control for the sediments below the unconformity at 185 mbsf remains very uncertain, although the observation of reversed and normal polarity signatures in the sediments between 180 and 344.6 mbsf is not inconsistent with the upper Oligocene biostratigraphic constraint.

INORGANIC GEOCHEMISTRY

Interstitial Water

Table 5 shows the results of interstitial-water analyses in Hole 908A. Sodium is relatively constant in Hole 908A, and potassium decreases by about 40% from near seawater values (seawater K = 10.96 mmol/L) at the surface to less than 8 mmol/L below 100 m. Magnesium and calcium (Fig. 19) show different trends. Magnesium decreases downward from seawater values (seawater Mg = 56.74 mmol/L) at the surface to less than 30 mmol/L at the bottom of Hole 908A. Calcium shows a slight decrease with depth from seawater values (seawater Ca = 11.05 mmol/L) to less than 8 mmol/L at about 100 mbsf and then back up to near seawater values at the bottom. Although magnesium is diffusing downward in these sediments, it does not appear that calcium is diffusing upward. Ammonia is near zero at the surface and increases to levels above 1000 μmol in the deeper parts of the hole (Fig. 19). The diagenesis of organic matter is supplying abundant ammonia, and there is no indication of an important sink for ammonia at depth. The most important sink is oxidation at the sediment-water interface.

Chloride is virtually invariant with depth in Hole 908A, but silica (Fig. 19) shows a steady increase with depth to about 1000 μmol/L at depth. This is probably supplied by the dissolution of siliceous skeletons in these sediments.

Sulfate (Fig. 19) decreases rapidly in the core, reaching essentially zero at about 100 mbsf. The reduction of sulfate by organisms converts sulfur from the S^{+6} to the S^{-2} oxidation state using organic matter as the electron donor. The drop in sulfate levels to zero also sets the upper boundary for the presence of methane in the hole (see Fig. 21). There is no indication of a supply of sulfate from below. Alkalinity (Fig. 19) shows a large increase from seawater values at the sediment-water interface to values in excess of 17 meq/L below 200

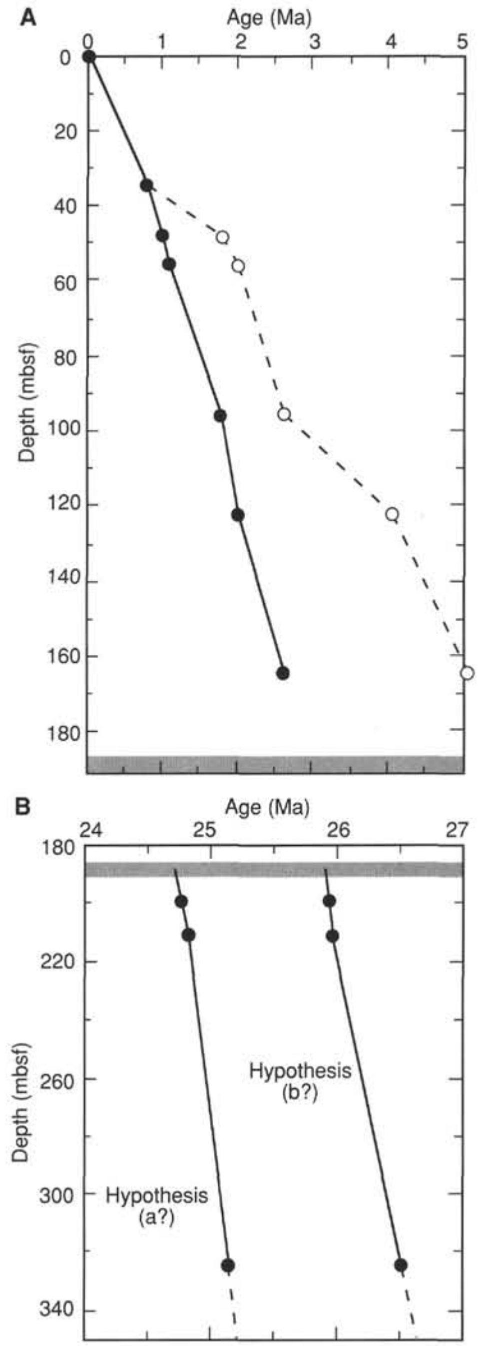

Figure 18. Age-depth model based on the magnetostratigraphy of sediments at Site 908. **A.** The solid circles and lines indicate our preliminary preferred age model for sedimentation in the Pliocene–Quaternary portion of Hole 908A (Table 4). An alternative model consistent with the lower Pliocene diatom biostratigraphic datum in Core 151-908A-17X is indicated by the open circles and dashed line and assumes the nonpreservation of the Jaramillo subchronozone. **B.** Two speculative models of sediment accumulation in the Oligocene portion of Hole 908A. The hiatus at 185 mbsf (gray bar) is thought to represent at least the entire Miocene, based on biostratigraphic grounds.

Table 5. Composition of interstitial waters in Hole 908A.

Core, section	Depth (mbsf)	Na (mmol/L)	K (mmol/L)	Mg (mmol/L)	Ca (mmol/L)	Chloride (mmol/L)	Sulfate (mmol/L)	Silica (µmol/L)	Ammonia (µmol/L)	pH	Alkalinity (meq/L)
151-908A-											
1H-3	4.45	491	12.38	52.1	11.0	550	29.0	141	66	7.61	3.26
4H-5	31.85	456	10.02	42.4	8.4	553	17.4	280	763	7.81	7.47
7H-5	60.35	430	6.91	41.2	7.6	548	7.7	399	924	7.73	10.72
10H-5	88.8	464	8.59	39.0	7.2	551	1.5	518	1397	7.76	11.72
13X-4	116.3	428	7.78	34.7	7.3	549	0.6	514	1461	7.79	10.14
16X-3	143.6	418	7.04	36.6	8.5	532	0.2	698	1347	7.38	10.71
19X-4	173.7	453	7.82	35.1	9.3	537	0.3	565	1325	7.51	13.71
22X-4	202.6	432	7.46	33.0	9.4	536	0.1	900	1229	7.54	15.19
25X-4	231.5	473	8.38	32.8	10.8	549	0.3	1019	1656	6.98	17.12
28X-5	262.0	468	7.88	31.6	11.4	544	0.3	958	1876	7.42	17.42
31X-5	290.9	464	6.84	30.3	11.8	541	0.9	1030	1708	7.33	16.71
34X-3	316.9	461	6.94	27.7	11.8	547	1.0	996	nd	7.32	16.21

Note: nd = not determined.

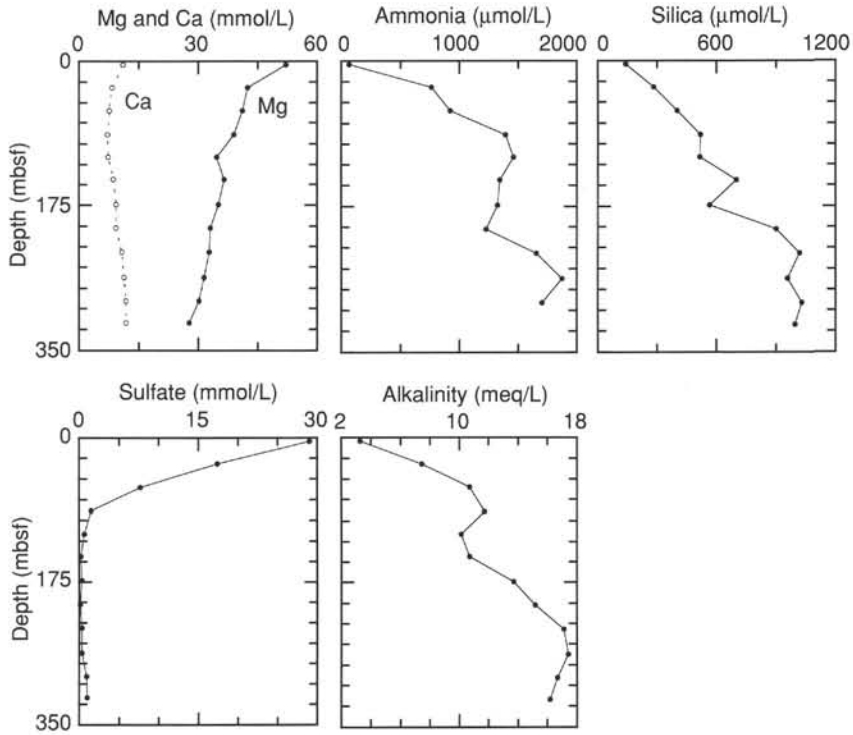

Figure 19. Interstitial water compositions at Site 908.

mbsf. This alkalinity is supported by the dissolution of carbonate in the sediments in Hole 908A (see Fig. 22), which is promoted by the sulfate reduction process ($2CH_2O_{org} + 2\ CaCO_3 + SO_4^{2-} \leftrightarrow 2Ca^{2+} + 4HCO_3^- + S^{2-}$). Carbonate mineral precipitation from pore waters is not evident.

Sediment Geochemistry

Major element abundances in sediments from Hole 908A are shown in Table 6. Both CaO and MgO (Fig. 20) decrease with depth in Hole 908A. The change in MgO and CaO may be stepwise at about 185 m, representing the lithologic boundary between Units I and II (see "Lithostratigraphy" section, this chapter). CaO contents are low but are lower below 185 m, whereas carbonate content is higher in the lower parts of the core (1.5%–2.0%) relative to the upper parts (see Fig. 23). Calcium carbonate levels around 1.6% correspond to CaO abundances of about 0.64%, and more than enough CaO is detected in the lower parts of Hole 908A to make the carbonate values shown in Figure 23. Note that the amount of $CaCO_3$ dissolution necessary to raise pore water alkalinity from 2 to 10 meq/L is about 0.04 wt% of the solid sediment (at about 50% porosity), and the dissolution in support of the elevated alkalinity profile in Figure 19 has no detectable effect on either the CaO or carbonate abundances.

Potassium (Fig. 20) shows a similar decrease with depth in the hole, but no trend is detectable in the composition of the potassium and aluminum-bearing parts of the sediments (Fig. 20), indicating little change in the composition of the feldspar-mica-illite component of these sediments. The decreases in MgO, CaO, and K_2O abundances are compensated by a subtle increase in the abundance of silica (Fig. 20), which rises from about 62 wt% in the top 100 m of the hole to about 64 wt% at the bottom. This corresponds to the lithologic changes described in the "Lithostratigraphy" section (this chapter).

Discussion

Interstitial-water compositions in Hole 908A show no unusual features. Carbonate and siliceous fossils are dissolving and affecting interstitial-water compositions as is the diagenesis of organic matter.

Table 6. Major element composition of sediments in Hole 908A.

Core, section	Depth (mbsf)	SiO_2 (wt%)	TiO_2 (wt%)	Al_2O_3 (wt%)	Fe_2O_3 (wt%)	MnO (wt%)	MgO (wt%)	CaO (wt%)	Na_2O (wt%)	K_2O (wt%)	P_2O_5 (wt%)	Total (wt%)
151-908A-												
1H-4	4.92	61.05	0.88	15.92	5.85	0.04	3.15	1.98	2.21	3.16	0.24	94.48
2H-3	9.68	64.41	0.85	15.02	5.30	0.09	2.61	1.91	2.57	2.88	0.15	95.79
3H-3	19.29	67.38	0.72	13.10	4.96	0.04	2.66	2.00	2.31	2.94	0.35	96.47
4H-4	29.54	61.05	0.95	16.72	6.68	0.04	2.88	1.85	2.15	3.09	0.16	95.57
5H-3	37.54	61.42	0.93	16.61	6.50	0.04	2.89	1.82	2.04	3.19	0.17	95.61
6H-3	47.03	63.97	0.70	13.51	4.34	0.03	2.60	1.76	2.71	2.81	0.19	92.61
7H-3	56.46	62.82	0.87	16.15	5.79	0.03	2.68	1.79	2.32	3.16	0.17	95.78
8H-4	67.15	61.32	0.90	16.60	6.51	0.04	3.03	1.88	2.16	3.31	0.16	95.92
9H-4	76.56	61.83	0.97	16.82	7.45	0.04	2.81	1.70	1.90	3.07	0.16	96.75
10H-4	86.14	60.83	0.93	15.64	6.39	0.08	2.64	1.85	2.02	2.71	0.18	93.28
11X-3	94.59	63.04	0.92	15.95	6.22	0.04	2.88	1.80	2.09	3.22	0.15	96.30
12X-4	105.36	61.73	0.89	16.13	6.62	0.03	2.79	1.77	2.18	3.06	0.20	95.42
13X-4	115.56	59.59	1.06	18.04	7.77	0.04	2.78	1.84	2.10	2.83	0.10	96.16
14X-4	125.18	57.87	1.02	18.92	7.88	0.04	2.90	1.72	2.01	2.98	0.12	95.47
15X-3	133.40	61.89	1.06	17.64	6.58	0.03	2.60	1.67	2.01	2.76	0.06	96.30
16X-3	142.89	59.22	0.93	17.34	8.46	0.04	2.79	1.65	2.14	2.76	0.12	95.45
17X-4	153.93	62.20	0.90	15.73	7.41	0.03	2.68	1.67	2.04	2.90	0.16	95.70
18X-3	161.91	63.83	0.91	15.33	6.17	0.02	2.45	1.61	2.04	2.89	0.09	95.33
19X-3	171.46	61.96	0.83	14.94	6.71	0.02	2.31	1.54	1.83	2.54	0.10	92.78
20X-3	181.10	61.47	1.07	18.56	5.96	0.02	2.44	1.63	1.95	2.82	0.05	95.97
21X-3	190.74	64.67	0.88	15.23	6.37	0.02	2.37	1.56	2.22	2.43	0.09	95.84
22X-4	202.35	63.20	0.94	16.14	6.36	0.02	2.48	1.72	1.79	2.58	0.21	95.43
23X-3	210.40	65.56	0.84	14.34	5.84	0.02	2.24	1.55	2.21	2.23	0.08	94.91
24X-3	219.64	63.12	0.90	15.77	5.89	0.02	2.39	1.83	2.33	2.36	0.09	94.61
25X-3	229.26	62.28	0.93	15.35	6.23	0.03	2.45	1.73	1.80	2.43	0.11	93.37
26X-3	238.84	63.66	0.88	15.13	5.56	0.02	2.32	1.66	1.79	2.51	0.12	95.67
27X-3	248.57	63.26	1.00	16.84	6.06	0.03	2.32	1.65	1.78	2.59	0.07	95.61
28X-3	258.08	63.46	1.04	17.14	5.83	0.02	2.30	1.64	1.80	2.69	0.06	95.99
29X-3	267.84	63.47	1.04	17.14	5.83	0.02	2.30	1.64	1.80	2.69	0.06	95.99
30X-3	277.55	64.19	0.91	15.82	6.15	0.03	2.33	1.65	1.93	2.40	0.09	95.55
31X-3	287.14	62.23	1.04	17.89	6.34	0.02	2.27	1.71	1.75	2.68	0.06	95.98
32X-3	296.87	66.37	0.85	14.34	6.15	0.03	2.24	1.63	2.09	2.24	0.12	96.06
33X-3	306.44	68.27	0.80	13.27	6.19	0.03	2.18	1.64	2.15	2.25	0.12	96.89
34X-3	316.14	68.22	0.76	12.21	6.89	0.03	2.14	1.66	1.71	2.06	0.15	95.82
35X-3	323.86	63.86	0.92	15.82	5.78	0.02	2.46	1.64	1.93	2.43	0.09	94.95
36X-3	333.74	63.81	0.92	16.17	6.47	0.02	2.46	1.62	1.96	2.56	0.08	96.07
37X-2	342.40	63.96	0.93	16.33	6.19	0.02	2.39	1.61	1.94	2.76	0.07	96.21

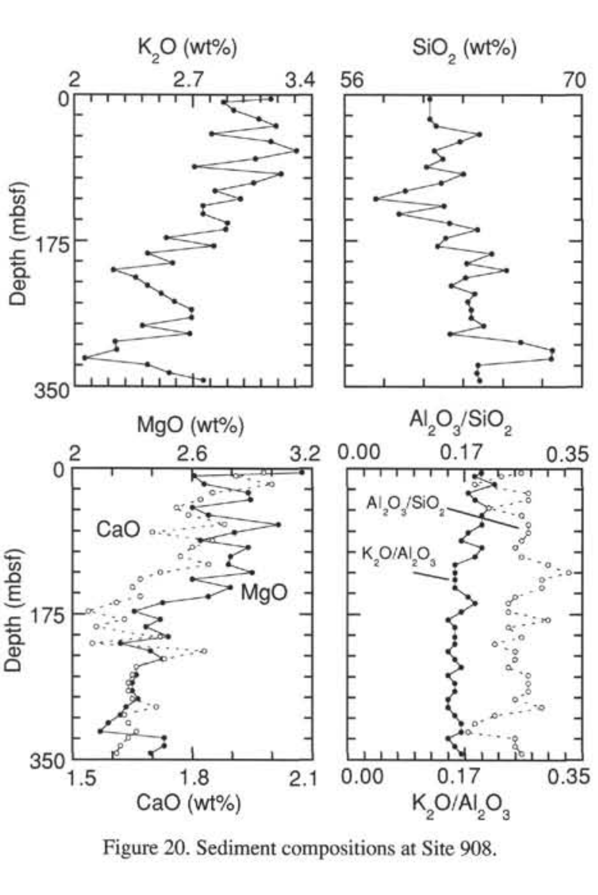

Figure 20. Sediment compositions at Site 908.

Sediment compositions reflect the lithologic boundary between Units I and II. This change is reflected generally in a modest increase in silica content with equivalent decreases in CaO, MgO, and K_2O below the boundary. The sediments in Hole 908A are much more siliceous than at Site 907 (silica percentages in the low 60s in Hole 908A vs. the low 50s at Site 907), reflecting the increased distance of Site 908 from the volcanic centers near and on Iceland. The lithologic change between Units I and II is not reflected in the mineralogical estimates in the "Lithostratigraphy" section, where quartz becomes substantially less abundant in Unit II. Siliceous microfossils must increase substantially in the lower unit to cause the increase in silica measured by X-ray fluorescence analysis.

ORGANIC GEOCHEMISTRY

The shipboard organic geochemistry program at Site 908 consisted of analyses of volatile hydrocarbons and determinations of inorganic carbon, total nitrogen, total carbon, and total sulfur (for methods see "Explanatory Notes" chapter, this volume).

Volatile Hydrocarbons

As part of the shipboard safety and pollution monitoring program, concentrations of methane (C_1) and ethane (C_2) gases were monitored every core using standard ODP headspace-sampling technique. Concentrations of methane were low in the upper 90 m (3 to 10 ppm); ethane was not detected in this interval (Fig. 21). Below 90 mbsf, methane concentrations sharply increased by about three orders of magnitude, reaching 10,000 ppm at 150 mbsf. At that depth, also first amounts of ethane (2–3 ppm) were detected; the methane/ethane (C_1/C_2) ratio is about 3500 (Fig. 21). Both methane and ethane continuously increased farther downhole. Maximum values occurred be-

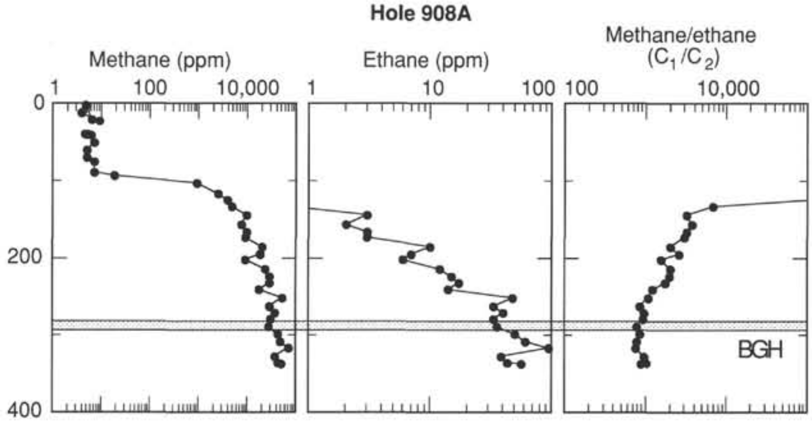

Figure 21. Records of headspace methane (C_1) and ethane (C_2) concentrations and C_1/C_2 ratios in sediments from Hole 908A. "BGH" marks the calculated depth of the base of gas hydrates possibly present at Hole 908A (see text for further explanations).

tween 250 and 340 mbsf (methane: 30,000–70,000 ppm, ethane: 30–60 ppm; Fig. 21). In this lower part of the sedimentary sequence of Hole 908A, relatively constant C_1/C_2 ratios of 800 to 1000 were determined; traces of propane also occurred (0.5 to 3 ppm; Table 7).

For safety considerations, the C_1/C_2 ratio is generally used to get quick information about the origin of the hydrocarbons (i.e., to distinguish between biogenic gas and gas migrated from a deeper source of thermogenic hydrocarbons). Very high C_1/C_2 ratios indicate a gas (C_1) formation by microbial processes. On the other hand, major amounts of C_2 (to C_5) are associated with thermogenic hydrocarbon generation. When interpreting the C_1/C_2 ratios, it has to be considered, however, that minor amounts of C_2 (and C_3, C_4, C_5) also can be generated in situ during early (low-temperature) diagenesis of organic matter. The importance of this process increases with increasing burial, resulting in a consistent ("normal") decrease in C_1/C_2 with increasing depth as recorded at numerous DSDP and ODP sites (JOIDES PPSP, 1992).

The C_1/C_2 ratios at Site 908 are generally high, suggesting a biogenic origin of the methane. Furthermore, the record shows the normal consistent decrease in C_1/C_2 ratios from >6000 to about 800–1000 near the bottom of the hole (Fig. 21). The methane probably is formed by in-situ microbial fermentation of the marine organic carbon, which is present in major amounts in the lower part of the sedimentary sequence. Similar in-situ microbial methane production from marine organic carbon resulting in high biogenic gas concentrations also has been described at other DSDP/ODP sites (e.g., at the Walvis Ridge; Meyers and Brassell, 1985). At Hole 908A, the methanogenesis has begun at depths between 90 and 105 mbsf, as clearly indicated by the sharp increase in methane concentration and the contemporaneous sharp cessation of sulfate reduction (see "Inorganic Geochemistry" section, this chapter; Fig. 19).

Although no obvious gas hydrates were observed at Hole 908A, the maximum concentration of methane below 250 mbsf may possibly be related to the presence of hydrates. According to the pressure-temperature stability field of gas hydrates (cf., Kvenvolden and Barnard, 1983), a geothermal temperature gradient of about 60°C (see "Downhole Measurements" section, this chapter), a water depth of 1284 m, and a bottom water temperature of about 0°C, gas hydrates are stable down to about 280 mbsf. This would imply that Hole 908A, which reached a final depth of 340 m, was drilled through the base of the gas hydrates into the zone of free gas.

Table 7. Results of headspace gas analysis from Hole 908A.

Core, section, interval top (cm)	C_1	C_2	C_1/C_2	C_3
1H-4, 0	8	0	—	0
2H-6, 0	4	0	—	0
3H-6, 0	5	0	—	0
4H-6, 0	5	0	—	0
5H-6, 0	6	0	—	0
6H-6, 0	7	0	—	0
7H-6, 0	5	0	—	0
8H-6, 0	5	0	—	0
9H-3, 135	7	0	—	0
10H-6, 0	7	0	—	0
11X-3, 0	18	0	—	0
12X-3, 0	902	0	—	0
13X-5, 0	2422	0	—	0
14X-4, 0	3846	0	—	0
15X-3, 0	4630	1	6614	0
16X-4, 0	9354	3	3118	0
17X-6, 0	7356	2	3678	0
18X-6, 0	9359	3	3120	0
19X-5, 0	8892	3	2964	0
20X-6, 0	20432	10	2043	0
21X-6, 0	17856	7	2551	0
22X-5, 0	9127	6	1521	0
23X-6, 0	23955	12	1996	0
24X-6, 0	29031	15	1935	0
25X-5, 0	29120	17	1713	0
26X-5, 0	17155	14	1225	0
27X-5, 0	51059	48	1064	0
28X-6, 0	28096	33	851	0.4
29X-5, 0	37528	40	938	0
30X-5, 0	30634	33	928	0.7
31X-5, 0	27382	35	782	0.9
32X-6, 0	42186	50	844	1.6
33X-6, 0	46690	61	765	3.0
34X-4, 0	70993	94	755	3.0
35X-5, 0	36222	38	953	1.0
36X-4, 0	43756	43	1018	1.0
37X-2, 0	49336	56	881	1.0

Note: Methane (C_1), ethane (C_2), and propane (C_3) concentrations are given in parts per million (ppm).

Carbon, Nitrogen, and Sulfur Concentrations

The results of determinations of inorganic carbon, carbonate, total carbon, total nitrogen, and total sulfur are summarized in Tables 8 and 9 and presented in Figures 22 and 23.

In general, the carbonate contents of the sedimentary sequence of Hole 908A are very low; most of the values are <2%, with some higher values of 2%–5% in the lower part of the sequence (Fig. 23). According to the carbonate record, this sequence can be divided into three intervals. The upper interval (0–82 mbsf; Quaternary to upper Pliocene), which corresponds to lithologic Subunit IA, is characterized by very low carbonate percentages between 0% and 2%. Only in the uppermost sample (0.33 mbsf), a relatively high carbonate content of almost 9% was determined. In the middle interval (82 to 185 mbsf; Pliocene) corresponding to Subunits IB and IC, carbonate is nearly absent (<1%), with two exceptions. In Sections 151-908A-14X-1 through -5 and Section 151-908A-16X-3 carbonate contents reach distinctly higher values of 2% to 5.6% and 3.7%, respectively (Fig. 23). These high carbonate values are probably caused by increased contents of detrital carbonate (see "Lithostratigraphy" sec-

Table 8. Summary of geochemical analyses of sediments in Hole 908A.

Core, section, interval top (cm)	Depth (mbsf)	IC (%)	$CaCO_3$ (%)	TC (%)	TOC (%)	TN (%)	TS (%)	C/N	C/S
151-908A-									
1H-1, 33	0.33	1.06	8.8	1.24	0.18	0.00	0.07		2.6
1H-2, 36	1.86	0.24	2.0	1.59	1.35	0.05	0.17	27.0	7.9
1H-3, 108	4.08	0.02	0.2	0.31	0.29	0.00	0.08		3.6
1H-4, 35	4.85	0.27	2.2	0.56	0.29	0.05	0.05	5.8	5.8
2H-1, 18	5.58	0.03	0.2	0.35	0.32	0.00	0.09		3.6
2H-1, 96	6.36	0.26	2.2	1.84	1.58	0.07	0.14	22.6	11.3
2H-2, 40	7.30	0.15	1.2	0.88	0.73	0.00	0.13		5.6
2H-3, 24	8.64	0.08	0.7	0.47	0.39	0.06	0.00	6.5	
2H-4, 44	10.34	0.13	1.1	0.51	0.38	0.00	0.00		
2H-5, 38	11.78	0.09	0.7	0.77	0.68	0.05	0.07	13.6	9.7
2H-6, 35	13.25	0.17	1.4	1.04	0.87	0.07	0.20	12.4	4.3
2H-7, 40	14.80	0.11	0.9	0.44	0.33	0.00	0.00		
3H-1, 82	15.72	0.10	0.8	0.56	0.46	0.06	0.00	7.7	
3H-2, 75	17.15	0.07	0.6	0.69	0.62	0.07	0.10	8.9	6.2
3H-3, 29	18.19	0.04	0.3	0.36	0.32	0.00	0.00		
3H-4, 38	19.78	0.04	0.3	0.68	0.64	0.08	0.04	8.0	16.0
3H-5, 33	21.23	0.17	1.4	0.82	0.65	0.07	0.07	9.3	9.3
3H-6, 46	22.86	0.10	0.8	0.60	0.50	0.08	0.09	6.2	5.6
4H-1, 41	24.81	0.08	0.7	0.50	0.42	0.06	0.05	7.0	8.4
4H-2, 42	26.32	0.08	0.7	0.66	0.58	0.07	0.00	8.3	
4H-3, 28	27.68	0.02	0.2	0.38	0.36	0.07	0.12	5.1	3.0
4H-4, 44	29.34	0.07	0.6	0.87	0.80	0.09	0.13	8.9	6.2
4H-5, 32	30.72	0.15	1.2	1.17	1.02	0.09	0.00	11.3	
4H-6, 30	32.20	0.03	0.2	0.51	0.48	0.07	0.43	6.9	1.1
4H-7, 30	33.70	0.19	1.6	1.04	0.85	0.07	0.15	12.1	5.7
5H-1, 27	34.17	0.10	0.8	0.68	0.58	0.07	0.06	8.3	9.7
5H-2, 27	35.67	0.06	0.5	0.68	0.62	0.09	0.12	6.9	5.2
5H-3, 27	37.17	0.04	0.3	0.52	0.48	0.08	0.09	6.0	5.3
5H-4, 27	38.67	0.12	1.0	0.91	0.79	0.06	0.30	13.2	2.6
5H-5, 27	40.17	0.05	0.4	0.60	0.55	0.06	0.09	9.2	6.1
5H-5, 99	40.89	0.09	0.7	0.78	0.69	0.05	0.07	13.8	9.9
5H-6, 48	41.88	0.28	2.3	0.65	0.37	0.05	0.00	7.4	
5H-7, 27	43.17	0.08	0.7	0.59	0.51	0.00	0.00		
6H-1, 26	43.66	0.13	1.1	0.81	0.68	0.06	0.07	11.3	9.7
6H-2, 27	45.17	0.06	0.5	0.48	0.42	0.00	0.05		8.4
6H-3, 101	47.41	0.03	0.2	0.80	0.77	0.07	0.00	11.0	
6H-4, 27	48.17	0.08	0.7	0.43	0.35	0.00	0.04		8.8
6H-5, 28	49.68	0.10	0.8	0.89	0.79	0.08	0.11	9.9	7.2
6H-6, 29	51.19	0.06	0.5	0.72	0.66	0.06	0.00	11.0	
6H-7, 29	52.69	0.07	0.6	0.74	0.67	0.06	0.00	11.2	
7H-1, 27	53.17	0.16	1.3	0.89	0.73	0.06	0.15	12.2	4.9
7H-2, 27	54.67	0.04	0.3	0.68	0.64	0.06	0.04	10.7	16.0
7H-3, 27	56.17	0.05	0.4	0.67	0.62	0.08	0.00	7.8	
7H-4, 25	57.65	0.04	0.3						
7H-5, 24	59.14	0.19	1.6	1.17	0.98	0.08	0.16	12.2	6.1
7H-6, 24	60.64	0.05	0.4	0.50	0.45	0.00	0.00		
7H-7, 26	62.16	0.07	0.6	0.71	0.64	0.00	0.00		
8H-1, 21	62.61	0.02	0.2	0.81	0.79	0.09	0.05	8.8	15.8
8H-2, 20	64.10	0.06	0.5	0.84	0.78	0.07	0.00	11.1	
8H-3, 20	65.60	0.02	0.2	0.75	0.73	0.10	0.11	7.3	6.6
8H-5, 20	68.60	0.17	1.4	1.19	1.02	0.10	0.00	10.2	
9H-1, 22	72.12	0.09	0.7	0.92	0.83	0.09	0.00	9.2	
9H-3, 22	75.12	0.04	0.3	0.72	0.68	0.06	0.00	11.3	
9H-5, 23	78.02	0.15	1.2	1.01	0.86	0.10	0.00	8.6	
10H-1, 42	81.82	0.28	2.3	0.93	0.65	0.06	0.13	10.8	5.0
10H-3, 25	84.65	0.05	0.4	0.80	0.75	0.08	0.04	9.4	18.8
10H-5, 27	87.67	0.02	0.2	0.73	0.71	0.09	0.00	7.9	
11X-2, 109	93.49	0.05	0.4	0.81	0.76	0.09	0.00	8.4	
11X-3, 12	94.02	0.04	0.3	0.79	0.75	0.07	0.04	10.7	18.8
12X-1, 31	100.91	0.02	0.2	0.71	0.69	0.09	0.15	7.7	4.6
12X-3, 71	104.31	0.03	0.2	0.76	0.73	0.09	0.06	8.1	12.2
13X-1, 29	110.69	0.05	0.4	0.72	0.67	0.08	0.14	8.4	4.8
13X-3, 93	114.33	0.02	0.2	0.52	0.50	0.07	0.00	7.1	
13X-5, 30	116.70	0.09	0.7	0.32	0.23	0.00	0.00		
14X-1, 50	120.50	0.42	3.5	1.07	0.65	0.08	0.11	8.1	5.9
14X-3, 50	123.50	0.67	5.6	2.24	1.57	0.11	0.96	14.3	1.6
14X-5, 17	126.17	0.25	2.1	0.97	0.72	0.08	0.18	9.0	4.0
15X-1, 66	130.36	0.08	0.7	0.89	0.81	0.09	0.19	9.0	4.3
15X-3, 66	133.36	0.07	0.6	0.87	0.80	0.09	0.20	8.9	4.0
16X-1, 66	139.86	0.05	0.4	0.96	0.91	0.09	0.40	10.1	2.3
16X-3, 66	142.86	0.05	0.4	1.26	1.21	0.10	0.00	12.1	
16X-3, 140	143.60	0.45	3.7	1.72	1.27	0.09	0.22	14.1	5.8
16X-4, 66	144.36	0.04	0.3	0.67	0.63	0.06	0.00	10.5	
17X-1, 68	149.38	0.05	0.4	1.22	1.17	0.12	0.61	9.8	1.9
17X-3, 68	152.38	0.02	0.2	0.72	0.70	0.09	0.10	7.8	7.0
17X-5, 68	155.38	0.09	0.7	1.18	1.09	0.10	0.11	10.9	9.9
18X-1, 65	158.85	0.06	0.5	1.25	1.19	0.11	0.06	10.8	19.8
18X-3, 65	161.85	0.08	0.7	0.91	0.83	0.09	0.18	9.2	4.6
18X-5, 65	164.85	0.03	0.2	0.70	0.67	0.07	0.14	9.6	4.8
19X-1, 99	168.79	0.21	1.7	1.24	1.03	0.10	1.43	10.3	0.7
19X-2, 100	170.30	0.16	1.3	1.24	1.08	0.08	0.08	13.5	13.5
19X-3, 100	171.80	0.14	1.2	1.33	1.19	0.10	0.43	11.9	2.8
19X-4, 140	173.70	0.05	0.4	0.95	0.90	0.18	0.82	5.0	1.1
19X-5, 101	174.81	0.10	0.8	0.97	0.87	0.10	0.26	8.7	3.3
20X-1, 52	177.92	0.08	0.7	0.80	0.72	0.08	0.96	9.0	0.8
20X-2, 77	179.67	0.31	2.6	1.33	1.02	0.07	0.00	14.6	

Table 8 (continued).

Core, section, interval top (cm)	Depth (mbsf)	IC (%)	$CaCO_3$ (%)	TC (%)	TOC (%)	TN (%)	TS (%)	C/N	C/S
20X-3, 73	181.13	0.09	0.7	0.84	0.75	0.09	0.21	8.3	3.6
20X-5, 76	184.16	1.54	12.8	2.56	1.02	0.09	0.23	11.3	4.4
21X-1, 117	188.27	0.07	0.6	1.36	1.29	0.11	1.46	11.7	0.9
21X-3, 118	191.28	0.15	1.2	1.46	1.31	0.12	1.27	10.9	1.0
22X-1, 120	197.90	0.14	1.2	0.80	0.66	0.09	0.00	7.3	
22X-3, 132	201.02	0.25	2.1	1.58	1.33	0.10	0.24	13.3	5.5
22X-4, 140	202.60	0.19	1.6	0.93	0.74	0.09	0.12	8.2	6.2
23X-1, 25	206.55	0.15	1.2	0.77	0.62	0.06	0.07	10.3	8.9
23X-3, 25	209.55	0.11	0.9	1.78	1.67	0.11	0.88	15.2	1.9
24X-1, 43	216.43	0.09	0.7	0.83	0.74	0.09	0.08	8.2	9.2
24X-3, 71	219.71	0.13	1.1	1.92	1.79	0.11	0.58	16.3	3.1
25X-1, 100	226.60	0.22	1.8	1.55	1.33	0.10	0.56	13.3	2.4
25X-3, 100	229.60	0.27	2.2	4.56	4.29	0.10	1.19	42.9	3.6
25X-4, 140	231.50	0.14	1.2	1.56	1.42	0.08	0.17	17.8	8.4
25X-5, 100	232.60	0.21	1.7	1.49	1.28	0.10	0.48	12.8	2.7
26X-1, 100	236.20	0.37	3.1	1.08	0.71	0.09	1.10	7.9	0.6
26X-5, 100	242.20	0.21	1.7	0.87	0.66	0.09	0.05	7.3	13.2
27X-1, 100	245.90	0.22	1.8	1.86	1.64	0.12	0.80	13.7	2.0
27X-4, 101	250.41	0.21	1.7	1.57	1.36	0.10	0.71	13.6	1.9
28X-1, 101	255.61	0.17	1.4	0.97	0.80	0.09	0.06	8.9	13.3
28X-4, 100	260.10	0.21	1.7	1.84	1.63	0.11	0.46	14.8	3.5
29X-1, 100	265.20	0.35	2.9	1.18	0.83	0.10	0.09	8.3	9.2
29X-4, 100	269.70	0.23	1.9	1.99	1.76	0.11	0.40	16.0	4.4
30X-1, 101	274.91	0.16	1.3	1.66	1.50	0.13	2.37	11.5	0.6
30X-4, 101	279.41	0.50	4.2	2.59	2.09	0.11	1.40	19.0	1.5
31X-1, 100	284.50	0.21	1.7	1.01	0.80	0.09	0.00	8.9	
31X-3, 100	287.50	0.49	4.1	1.38	0.89	0.08	0.00	11.1	
31X-5, 100	290.50	0.17	1.4	1.21	1.04	0.09	0.09	11.6	11.6
32X-1, 103	294.23	0.18	1.5	2.42	2.24	0.13	1.18	17.2	1.9
32X-5, 100	300.20	0.25	2.1	1.95	1.70	0.12	0.61	14.2	2.8
33X-1, 100	303.80	0.65	5.4	2.41	1.76	0.12	0.75	14.7	2.3
33X-4, 70	308.00	0.62	5.2	2.30	1.68	0.12	0.23	14.0	7.3
34X-1, 100	313.50	0.47	3.9	1.94	1.47	0.12	0.43	12.2	3.4
34X-4, 49	317.49	0.35	2.9	1.65	1.30	0.11	0.10	11.8	13.0
35X-1, 120	321.40	0.17	1.4	2.09	1.92	0.13	2.65	14.8	0.7
35X-4, 131	326.01	0.16	1.3	1.48	1.32	0.11	0.61	12.0	2.2
36X-1, 58	330.68	0.15	1.2	0.99	0.84	0.09	0.93	9.3	0.9
36X-4, 99	335.59	0.11	0.9	1.32	1.21	0.10	0.21	12.1	5.8
37X-1, 67	340.67	0.06	0.5	1.58	1.52	0.11	1.05	13.8	1.4
37X-2, 0	341.50	0.07	0.6	1.03	0.96	0.10	0.96	9.6	1.0
37X-2, 67	342.17	0.07	0.6	1.19	1.12	0.10	0.93	11.2	1.2

Notes: IC = inorganic carbon; $CaCO_3$ = carbonate; TC = total carbon; TOC = total organic carbon; TN = total nitrogen, TS = total sulfur; C/N = total organic carbon/total nitrogen ratios; C/S = total organic carbon/total sulfur ratios.

Table 9. Organic carbon, nitrogen, and sulfur contents of selected dropstones (coals, dark mudstones, siltstones) and black sulfide-rich lenses and pockets.

Core, section, interval (cm)	First suggestion (visual core description)	Results of CNS analyses TOC (%)	TN (%)	TS (%)	C/N	Classification (based on visual core description and chemical data)
151-908A-						
1H-2, 62	Black lense, mudstone, coal ?	9.93	0	0		Black, TOC-rich mudstone; black shale
1H-3, 73	Coal, dark mudstone ?	2.25	0.13	0	17	Dark, TOC-rich mudstone
1H-3, 89	Coal, wood fragments ?	4.22	0.27	0	17	TOC-rich mudstone with wood fragments
1H-4, 81–86	Dark claystone ?	7.29	0.32	0.09	23	Dark, TOC-rich mudstone
2H-3, 111	Black mudstone (coal?)	15.91	0.31	0	51	Dark coaly mudstone
5H-2, 106	Coal ?	3.24	0	0.86		Dark, TOC-rich mudstone
5H-6, 0	Dark gray siltstone ?	0.13	0.04	0.06	3	Dark gray siltstone
8H-5, 122	Coal ?	22.55	0.31	3.13	73	Coal, coaly mudstone
10H-4, 119	Coal ?	58.97	0.77	0.74	77	Coal
12H-1, 43	Dark silt, claystone ?	0.77	0.13	0.07	6	Dark gray mud, siltstone
151-908B-						
5H-1, 16	Dark olive mudstone, coal ?	1.92	0	0		Dark, TOC-rich mudstone
5H-5, 28	Black spots, burrows ?	1.16	0.08	4.29	15	(Mono-) sulfide-rich spots, lenses, burrows
5H-6, 43	Coal ?	0.90	0.13	2.37	7	(Mono-) sulfide-rich lense
6H-4, 50	Pyritic coal ?	0.31	0	4.38		Pyrite (pyritized coal)

tion, this chapter). In the lower interval (185–344.6 mbsf; upper Oligocene), carbonate contents are generally slightly higher, ranging between 1% and 5%. A single maximum value of 12.8% occurs at the top of this interval. The carbonate in the upper Oligocene sediments is mainly of biogenic origin (e.g., benthic foraminifers; see "Biostratigraphy" section, this chapter).

The total organic carbon (TOC) contents are generally high and vary between 0.3% and 4.3% (Fig. 23). In the upper 120 mbsf (i.e., Quaternary to upper Pliocene), TOC values range from 0.3% to 1%. In two samples of the uppermost part of the interval, even higher values of about 1.5% were measured. The lower interval between 120 and 344.6 mbsf is characterized by high TOC values between 0.5% and 2.3%, with the higher values dominating in the upper Oligocene interval. A maximum TOC value of 4.3% occurs at about 230 mbsf.

The total nitrogen contents are generally very low (0% to 0.13%; Table 8). The total sulfur values vary between 0% and 1.5%; two higher values of 2.4% and 2.7% occur at about 275 mbsf and 320 mbsf, respectively (Fig. 23). According to the sulfur record, the sed-

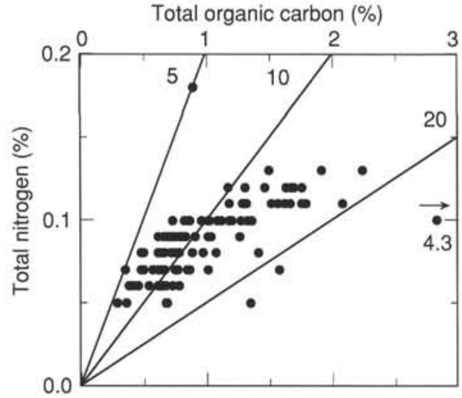

Figure 22. Total organic carbon vs. total nitrogen. Lines of C/N ratios of 5, 10, and 20 are indicated. Data points with nitrogen values of zero (determined on organic-carbon-lean samples) were not included.

imentary sequence of Hole 908A can be divided into two intervals. In the upper 120 m, the sulfur contents are very low (<0.2%), whereas the lower interval (120 to 345 mbsf) is characterized by high-amplitude variations between 0% and 1.5%.

In lithologic Subunits IA and IB, dropstones occur in common to trace amounts (see "Lithostratigraphy" section, this chapter). Parts of these dropstones are described as dark mudstones, siltstones, and coals. On a selected (however, not representative) set of dropstones, total (organic) carbon, nitrogen, and sulfur were determined as well (Table 9). Based on these data, several of the dropstones suggested to be "coals" have organic carbon contents of only 1% to 4%. Thus, they were classified as "dark (TOC-rich) mudstones or siltstones." The organic carbon contents of coal fragments and coaly mudstones reach maximum values of 16% to 59% (Table 9). Black spots, lenses, and pockets, which commonly occur in the more homogenous sedimentary intervals of Unit I (see "Lithostratigraphy" section, this chapter), have high sulfur contents of 2.4%–4.3% and TOC values of about 1% (Table 9), indicating the presence of major amounts of (mono-) sulfides.

Composition of Organic Matter

The type of organic matter in the sediments of Hole 908A has been characterized using organic carbon/nitrogen (C/N) ratios (e.g., Stein, 1991a). The average C/N ratios of marine zoo- and phytoplankton are between 5 and 8, whereas higher land plants have ratios between 20 and 200 (Bordowskiy, 1965; Emerson and Hedges, 1988; for further comments see also "Organic Geochemistry" section, "Site 907" chapter, this volume).

In Hole 908A sediments, most of the C/N ratios vary between 5 and 15 and thus indicate a mixture between marine and terrigenous organic carbon, with a dominance of the marine material (Figs. 22 and 23, Table 8). The sediments from the uppermost Quaternary interval, characterized by very high TOC values of about 1.5%, also have very high C/N ratios of about 25, reflecting a terrigenous source of the organic material. These samples are from dark gray sedimentary intervals probably representing glacial periods with an increased supply of terrigenous matter by glaciomarine processes (cf., Henrich et al., 1989a). The presence of significant amounts of terrigenous organic carbon in the Quaternary to Pliocene section also is supported by coal particles and mudstones with plant and coal fragments, which occasionally occur in this interval (Table 9; see "Lithostratigraphy" section, this chapter).

Increased amounts of marine organic matter, indicated by very high TOC values and C/N ratios of about 10, have been preserved in the intervals between 185 and 310 mbsf (Fig. 23). The bacterial decomposition of this marine organic matter probably has caused the very high concentrations of methane present at Hole 908A (see above). The enrichment of marine organic matter in these upper Oligocene sediments coincides with increased abundances of biogenic opal (see "Lithostratigraphy" section, this chapter), suggesting increased surface-water productivity at that time. Furthermore, high-amplitude variations in (marine) organic carbon deposition may reflect short-term changes in paleoproductivity. A distinct short-term cyclicity is observed in the GRAPE density record (see "Physical Properties" section, this chapter), probably reflecting changes in biogenic opal concentrations that also may support paleoproductivity variations.

Further qualitative and quantitative organic geochemical data (such as detailed records of flux rates of terrigenous and marine or-

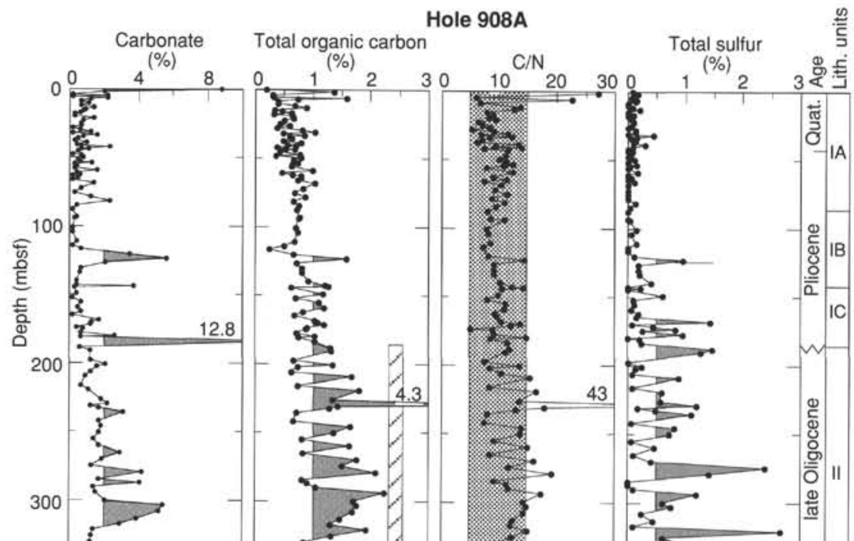

Figure 23. Carbonate contents, total organic carbon contents, organic carbon/total nitrogen (C/N) ratios, and total sulfur contents in sediments in Hole 908A. Stippled field in the C/N record indicates major to dominant occurrence of marine organic matter. The hatched bar marks interval of major occurrence of biogenic silica (see "Lithostratigraphy" section, this chapter).

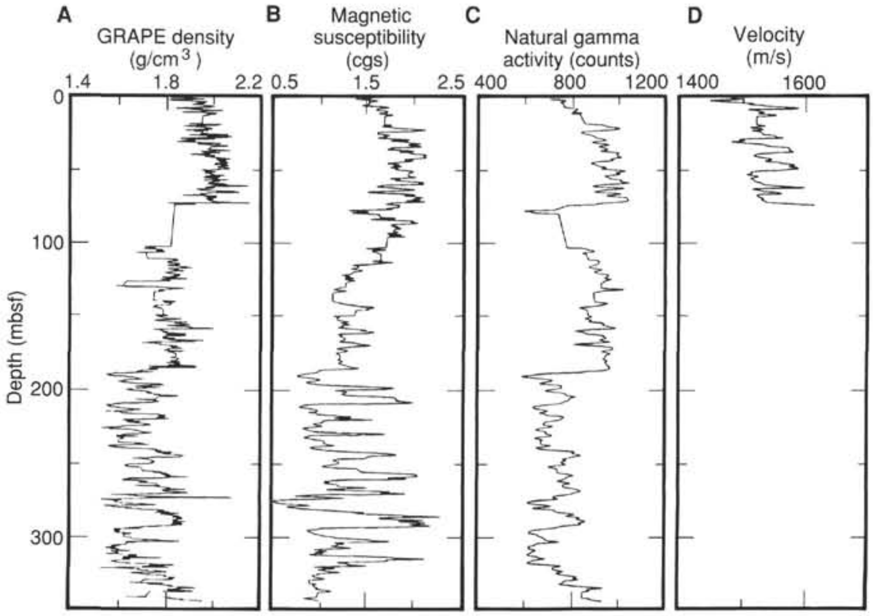

Figure 24. Hole 908A. **A.** GRAPE density, low-pass filtered. **B.** Magnetic susceptibility, low-pass filtered. Units are logarithmic uncorrected cgs Bartington meter units. **C.** Natural gamma activity, low-pass filtered. **D.** Compressional-wave velocities, low-pass filtered.

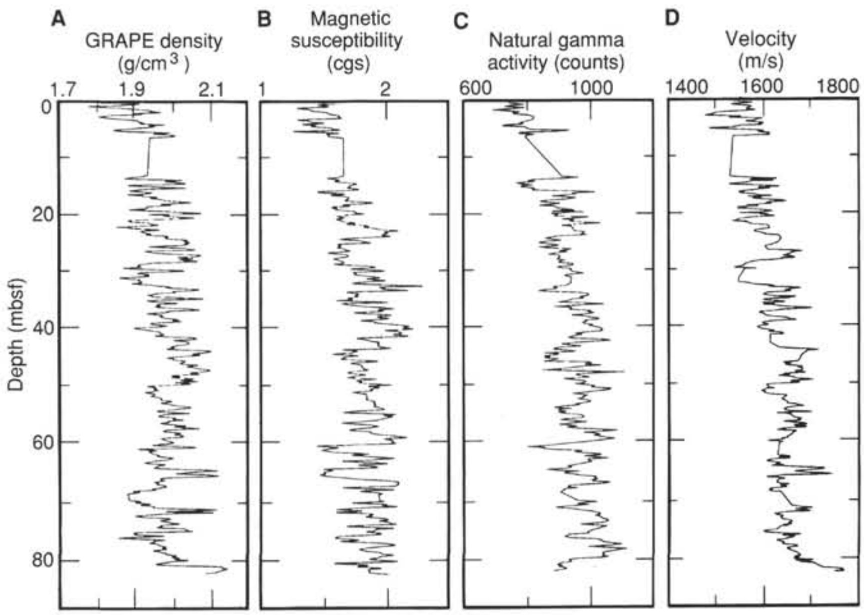

Figure 25. Hole 908B. **A.** GRAPE density, low-pass filtered. **B.** Magnetic susceptibility, low-pass filtered. Units are logarithmic uncorrected cgs Bartington meter units. **C.** Natural gamma activity, low-pass filtered. **D.** Compressional-wave velocities, low-pass filtered.

ganic carbon as well as biomarker data) are required before a more detailed paleoceanographic interpretation of the organic carbon data can be done.

PHYSICAL PROPERTIES

Introduction

The shipboard physical properties program at Site 908 included nondestructive measurements of bulk density, bulk magnetic susceptibility, compressional-wave velocity, and total natural gamma activity on whole sections of core using the multi-sensor track (MST), as well as discrete measurements of thermal conductivity, compressional-wave velocity, shear strength, and index properties. The downhole temperature measurements also are reported here. Methodology is discussed in the "Explanatory Notes" chapter (this volume).

Two holes (908A and 908B) were drilled at the site using advanced piston corer (APC) and extended core barrel (XCB). The degree of core disturbance, as observed both visually and in the physical properties, increased slightly from APC to XCB cores. Samples for discrete measurements were selected from the most undisturbed parts of the split half-core sections.

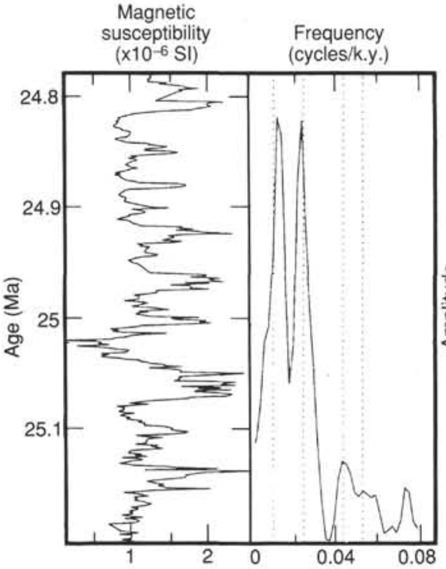

Figure 26. Results of spectral analysis of magnetic susceptibility record of the time interval 24.78–25.2 Ma for Hole 908A. Vertical dotted lines correspond to 100 k.y., 41 k.y., 23 k.y., and 19 k.y. orbital periodices.

Whole-core Measurements

Whole-round measurements of GRAPE density at 1-cm intervals, magnetic susceptibility at 3- to 5-cm intervals, and natural gamma activity at 18-cm intervals were performed on the 0–345 mbsf interval recovered in Hole 908A and the 0–83.4 mbsf interval sampled in Hole 908B. Whole-round compressional-wave velocity at 3-cm intervals was measured on the first nine APC cores (0–81.4 mbsf) from Hole 908A and on all 10 cores (0–83.4 mbsf) from Hole 908B. XCB cores consistently failed to give reliable velocity data. Figures 24 and 25 show plots of the four parameters for Holes 908A and 908B, respectively. Extended gaps in the data correspond either to intervals of poor recovery (for example, Hole 908B, 6–15 mbsf) or to vagaries of the MST data storage system. The gap in the GRAPE density and in the gamma records from about 75–100 mbsf in Hole 908A is the result of the failure of the system to send data to either the VAX or diskette. Measurements of magnetic susceptibility were performed later on half-round cores from this interval and are included in Figure 24D.

Time series of magnetic susceptibility and GRAPE density were generated using a tentative chronology based on polarity reversal stratigraphy (see "Paleomagnetics" section, this chapter). The time series were analyzed using a fast Fourier transform routine. The results for the time interval 0–1.2 Ma suggest that fluctuations are within the Milankovitch band (104–105 k.y.), although variance peaks did not consistently align with orbital periods. The results for the time interval 24.78–25.2 Ma (Fig. 26) suggest the presence of significant variance at the 100-k.y. and 41-k.y. periods.

Thermal Conductivity

Thermal conductivities measured at Hole 908A are given in Table 10 and in Figure 27 together with downhole trends in laboratory values of bulk density, water content, and grain density. Measurements were typically performed at 75 cm in four whole-round sections from each core. A black rubber standard (cond. = 0.54 ± 0.02 W/m·K) was used each time to evaluate the degree of error in the measurements.

The thermal conductivities measured in the upper portion of Hole 908A from the seafloor to 185 mbsf range from 0.8–1.8 W/m·K. The measured conductivities decreased and became less variable (0.8–1.35 W/m·K) in the lower portion of the hole (185–344.6 mbsf), which corresponds to lithologic Unit II below the unconformity (See

Table 10. Thermal conductivity measurements from Hole 908A.

Core, section, interval top (cm)	Depth (mbsf)	M	P #	TC_{corr} (W/m·K)	Std. dev. (W/m·K)	Drift (°C/min)
151-908A-						
1H-1, 75	0.75	F	325	1.168	0.00239	–0.020
1H-2, 75	2.25	F	338	1.139	0.00593	–0.009
1H-3, 75	3.75	F	339	1.668	0.00299	0.018
1H-4, 35	4.85	F	332	1.334	0.00247	0.010
3H-2, 75	17.15	F	332	1.437	0.00277	0.013
3H-3, 75	18.65	F	325	1.523	0.00240	0.007
3H-5, 75	21.65	F	338	1.484	0.00296	–0.009
3H-6, 75	23.15	F	339	1.454	0.00312	–0.015
4H-2, 75	26.65	F	325	1.731	0.00466	0.020
4H-3, 75	28.15	F	338	1.134	0.00252	0.015
4H-5, 75	31.15	F	339	1.812	0.00228	0.015
4H-6, 75	32.65	F	17	1.521	0.00338	–0.013
5H-2, 75	36.15	F	325	1.776	0.00222	0.012
5H-3, 75	37.65	F	338	1.277	0.00276	0.007
5H-5, 75	40.65	F	339	1.703	0.00383	0.011
5H-6, 75	42.15	F	17	1.643	0.00546	–0.015
6H-2, 75	45.65	F	332	1.604	0.00289	0.015
6H-3, 75	47.15	F	325	1.700	0.00367	0.010
6H-5, 75	50.15	F	339	1.661	0.00218	–0.026
7H-2, 75	55.15	F	332	1.375	0.00502	–0.009
7H-3, 75	56.65	F	325	1.625	0.00330	–0.007
7H-3, 75	56.65	F	325	1.708	0.00279	0.002
7H-5, 75	59.65	F	339	1.845	0.00272	–0.019
7H-6, 75	61.15	F	17	1.431	0.00291	–0.031
8H-2, 75	64.65	F	332	1.699	0.00200	0.024
8H-3, 75	66.15	F	325	1.369	0.00344	0.007
8H-6, 2	69.92	F	17	1.407	0.00308	–0.024
9H-2, 75	74.15	F	332	1.391	0.00175	–0.003
9H-2, 75	74.15	F	332	1.363	0.06675	0.014
9H-3, 75	75.65	F	325	1.396	0.00407	0.019
9H-4, 75	77.04	F	339	1.388	0.00229	–0.017
9H-5, 75	78.54	F	17	1.465	0.00315	0.021
10H-2, 75	83.65	F	332	1.603	0.00424	0.014
10H-3, 75	85.15	F	325	1.444	0.00339	–0.002
10H-5, 75	88.15	F	339	1.571	0.00244	0.012
10H-6, 75	89.65	F	17	1.754	0.00293	0.009
11X-1, 75	91.65	F	332	1.194	0.00183	0.022
12X-1, 75	101.35	F	332	1.411	0.00214	0.033
12X-3, 75	104.35	F	339	1.426	0.00322	0.025
12X-4, 75	105.85	F	17	1.338	0.00177	0.016
13X-2, 75	112.65	F	332	1.386	0.00229	0.039
13X-3, 75	114.15	F	325	1.339	0.00111	0.012
13X-5, 75	117.15	F	339	1.564	0.00289	0.038
13X-6, 75	118.65	F	17	1.400	0.00304	0.035
14X-2, 75	122.25	F	332	1.301	0.00282	0.012
14X-3, 75	123.75	F	325	1.104	0.00251	0.007
14X-4, 75	125.25	F	339	0.928	0.00274	–0.007
15X-3, 75	133.45	F	339	1.202	0.00412	0.010
16X-2, 75	141.45	F	325	1.223	0.00872	–0.002
16X-3, 75	142.95	F	339	1.027	0.00187	0.023
16X-4, 75	144.45	F	17	1.170	0.00636	0.009
17X-2, 75	150.95	F	332	1.257	0.00314	0.027
17X-5, 75	155.45	F	339	1.154	0.00267	0.019
17X-6, 75	156.95	F	17	1.485	0.00434	0.016
18X-2, 75	160.45	F	332	1.256	0.00162	0.022
18X-5, 75	164.95	F	339	1.218	0.00248	0.014
18X-6, 75	166.45	F	17	1.339	0.00380	0.017
19X-2, 75	170.05	F	332	1.350	0.00218	0.027
19X-3, 75	171.55	F	325	1.520	0.00333	0.022
19X-4, 75	173.05	F	339	1.224	0.00268	0.035
19X-4, 75	173.05	F	339	1.169	0.00393	0.020
19X-5, 75	174.55	F	17	1.433	0.00344	0.027
20X-2, 75	179.65	F	332	1.348	0.00322	0.028
20X-2, 75	179.65	F	332	1.350	0.00262	0.017
20X-3, 75	181.15	F	325	1.363	0.00227	0.029
20X-5, 75	184.15	F	339	1.196	0.00344	0.034
20X-6, 75	185.65	F	17	1.193	0.00411	0.018
21X-2, 75	189.35	F	332	1.033	0.00253	0.016
21X-3, 75	190.85	F	325	1.058	0.00265	0.028
21X-5, 75	193.85	F	339	1.112	0.00369	0.031
21X-6, 75	195.35	F	17	1.012	0.00510	0.012
22X-2, 75	198.95	F	332	1.213	0.00384	0.030
22X-3, 75	200.45	F	325	1.213	0.00221	0.005
22X-4, 75	201.95	F	339	1.222	0.00288	0.028
22X-5, 75	203.45	F	17	1.169	0.00374	0.008
23X-2, 75	208.55	F	332	1.185	0.00261	0.038
23X-3, 75	210.05	F	325	1.075	0.00119	0.011
23X-5, 75	213.05	F	339	0.993	0.00228	0.002
23X-6, 75	214.55	F	17	1.053	0.00274	0.017
24X-2, 75	218.25	F	332	1.171	0.00351	0.003
24X-3, 75	219.75	F	325	0.975	0.00277	–0.036
24X-5, 75	222.75	F	339	1.254	0.00760	–0.009
24X-6, 75	224.25	F	17	1.120	0.00280	0.016
25X-2, 75	227.85	F	332	1.179	0.00145	0.012
25X-3, 75	229.35	F	325	1.058	0.00182	–0.019
25X-5, 75	232.35	F	17	1.092	0.00360	0.003
26X-2, 75	237.45	F	332	1.036	0.00285	0.014
26X-3, 75	238.95	F	325	0.944	0.00406	–0.009

Table 10 (continued).

Core, section, interval top (cm)	Depth (mbsf)	M	P #	TC_{corr} (W/m·K)	Std. dev. (W/m·K)	Drift (°C/min)
26X-5, 75	241.95	F	339	1.181	0.00695	–0.039
26X-6, 75	243.45	F	17	1.235	0.00291	–0.032
27X-2, 75	247.15	F	332	1.217	0.00365	0.018
27X-3, 75	248.65	F	325	1.291	0.00289	0.022
27X-4, 75	250.15	F	339	1.141	0.00296	0.008
27X-5, 75	251.65	F	17	1.090	0.00282	0.006
28X-2, 75	256.85	F	332	1.198	0.00251	–0.000
28X-3, 75	258.35	F	325	1.161	0.00298	–0.021
28X-4, 75	259.85	F	339	1.229	0.00242	0.031
28X-5, 75	261.35	F	17	1.197	0.00182	0.008
29X-2, 75	266.45	F	332	1.271	0.00322	0.021
29X-5, 75	270.95	F	339	1.126	0.00807	0.011
29X-6, 75	272.45	F	17	1.256	0.00219	0.005
30X-2, 75	276.15	F	332	1.088	0.00359	0.018
30X-3, 75	277.65	F	325	1.117	0.00224	–0.006
30X-5, 75	280.65	F	339	1.325	0.00144	0.022
31X-2, 75	285.75	F	332	1.290	0.00126	0.026
31X-3, 75	287.25	F	325	1.120	0.00198	–0.021
31X-5, 75	290.25	F	339	1.310	0.00173	0.009
31X-6, 75	291.75	F	17	1.486	0.00142	0.028
32X-2, 75	295.45	F	332	1.052	0.02164	0.021
32X-3, 75	296.95	F	325	0.979	0.00271	–0.016
32X-5, 75	299.95	F	339	1.104	0.00441	–0.003
32X-5, 75	299.95	F	339	1.119	0.00448	0.002
32X-6, 75	301.45	F	17	1.189	0.00426	–0.004
32X-6, 75	301.45	F	17	1.189	0.00418	–0.004
33X-2, 75	305.05	F	332	1.023	0.00285	0.014
33X-5, 75	309.55	F	339	1.036	0.00301	0.016
33X-6, 75	311.05	F	17	1.028	0.00367	0.008
34X-2, 75	314.75	F	332	1.085	0.00383	0.017
34X-3, 75	316.25	F	325	1.006	0.00248	0.012
34X-5, 75	319.25	F	339	1.167	0.00255	0.011
35X-2, 75	322.45	F	332	1.200	0.00510	–0.007
35X-3, 75	323.95	F	325	1.099	0.00344	0.032
35X-5, 75	326.95	F	339	1.269	0.00481	0.011
37X-1, 75	340.75	F	332	1.364	0.00196	0.013
37X-2, 75	342.25	F	325	1.361	0.00217	0.025
37X-2, 75	342.25	F	325	1.289	0.00320	0.006

Notes: M = method used, F = full-space; P # = probe number used for test; TC_{corr} = thermal conductivity corrected for drift; Std. dev. = standard deviation of the measurement.

"Lithostratigraphy" section, this chapter). The decrease in thermal conductivity in the deeper portion of the hole is associated with high measured values of porosity and water content (Fig. 27). The greater variation in the measured thermal conductivities above 180 mbsf is in the upper part associated with the higher variability in clay, and thus water content, in this interval. The cause for the increase in the variability in the otherwise rather homogeneous interval between 100 and 185 mbsf is unclear.

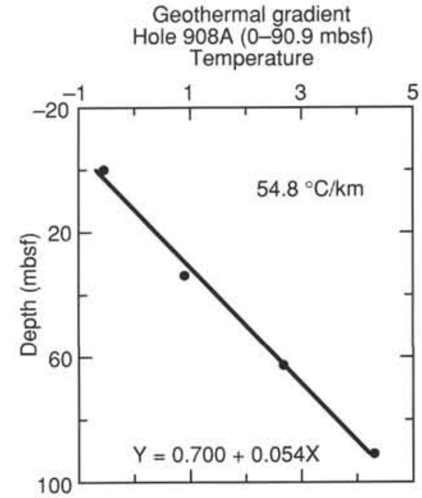

Figure 28. Temperature downhole in Hole 908A as calculated by the Adara tool measurements.

Bottom-hole Temperature Measurements and Geothermal Gradient

The bottom-hole temperature was determined at the mud line and three depths in Hole 908A by the Adara Temperature Tool. The equilibrium temperature was calculated as described in the "Explanatory Notes" chapter (this volume), with the following results: mud line: –0.543°C; 33.9 mbsf: 0.902°C; 62.4 mbsf: 2.676°C; and 90.9 mbsf: 4.309°C. The geothermal gradient determined by linear fit was estimated at 54.8°C/km (Fig. 28).

Split-core Measurements

Compressional Velocity

The digital sound velocimeter (DSV) and the Hamilton Frame apparatus were used to measure compressional velocity in the sediment from Hole 908A at the rate of one measurement per core section. The DSV was used to measure longitudinal velocity (along the core axis) in Cores 151-908A-1H through -9H-1 (0–72.1 mbsf). When it became impossible to insert the sonic transducers without cracking the sediment, measurements were continued using the Hamilton Frame

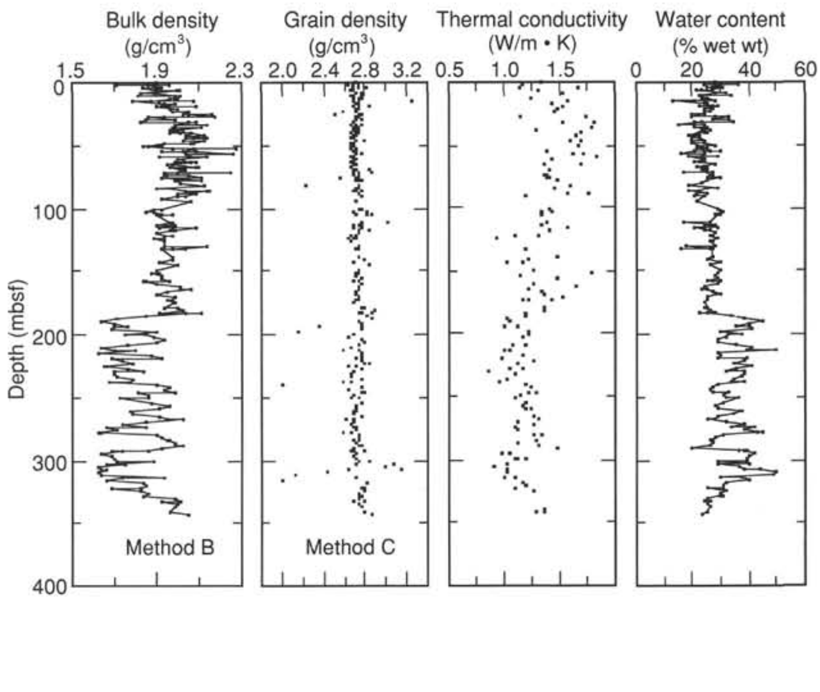

Figure 27. Comparison of index properties, measured on discrete samples, and thermal conductivity vs. depth in Hole 908A.

while the split core was still in the liner. Corrections for the core liner thickness and traveltime were made in Cores 151-908A-9H through -12X-4 (70–105.1 mbsf). The signal path was then perpendicular to the core axis. From 111.4 mbsf to Core 151-908A-34X at 319 mbsf, the sediments were sufficiently consolidated. Therefore, Hamilton Frame measurements were performed along the axis of the core on cut pieces of the sediment. The fact that the velocities parallel and perpendicular to the core axis do not have appreciable variation indicates that the sediments are relatively isotropic in the decimeter scale. The results of the velocity measurements are given in Table 11 and in Figure 29. MST velocities are given in Figure 24D and 25D.

Laboratory velocity data are compared with downhole sonic logging results in Figure 30 (see "Seismic Stratigraphy" section, this chapter). There is a strong co-variation between the downhole logging velocity measurements, the sonic log, and the discrete measurements. However, the discrete measurements are consistently 120 m/s lower than the logging values. The co-variation suggests that the considerable fluctuations of the velocities are mostly attributed to subtle variations in the homogeneous-appearing sedimentary sequence (see "Lithostratigraphy" section, this chapter) and not only to experimental fluctuations. The discrete measurements of compressional-wave velocities range, except for a few extreme values, between 1450 and 1750 m/s. Some of the high values are associated with sand-rich layers.

An examination of Figure 29 indicates that four distinct layers are characterized by the velocity and its variations downhole: (V1) 0–28 mbsf, range approximately 1550–1675 m/s; (V2): 28–70 mbsf, range 1610–1770 m/s; (V3): 70–240 mbsf, range 1470–1600 m/s, decreasing slightly downward; and (V4): 240–bottom of hole in 344.6 mbsf, range 1470–1650 m/s. It is remarkable that the low velocity layer (V3) extends across the marked stratigraphic unconformity at 185 mbsf, which seems indistinguishable in these data.

Shear Strength

Shear strength measurements were performed at a rate of one per section in split half-cores using the mechanical vane in sediment from the seafloor to approximately 80 mbsf. A hand-held penetrometer was used below this level as the sediment became too firm to test with the vane apparatus. Strength values increase with depth in the upper 200 m of sediments, from a few kPa near the surface to ~211 kPa at 200 mbsf, which is the maximum measurable value of the pocket penetrometer. In spite of the limitations in the comparison of vane shear and penetrometer values, a rough linear trend with depth is indicated. This trend is well defined in the vane shear data, as approximately 1.2 kPa/m from 0 to 28 mbsf and from 50 to 70 mbsf. In this depth interval, interlayering of weaker and stronger layers was observed, presumably corresponding to more or less sand-rich mud. The strength appears constant between 28 and 50 mbsf; this is not explained, but some of the failure patterns were anomalous in this interval, suggesting drilling disturbance or measuring problems. The data are presented in Table 12 and shown in Figure 31.

Index Properties

Gravimetric determinations of index properties were made for 284 samples in Hole 908A and 69 in Hole 908B at the rate of about two (908A) or about one (908B) samples per core section. The data are presented in Table 13. Method C produced the most consistent dry density and porosity determinations and more realistic grain densities, whereas the Method B bulk density appears the better of the two methods used. These data sets are plotted in Figures 27, 31, and 32.

The mean grain density is almost constant through the section, so the variations in bulk density, porosity, and dry density all reflect the variation in water content. The bulk densities determined on discrete samples compare well with bulk densities derived from resistivity downhole logs (Figs. 33 and 34; see "Downhole Measurements" section, this chapter), showing that most of the observed variation mirrors changes in the sedimentary column, and not experimental (drilling and laboratory) scatter.

Geotechnical Units

The downhole records of GRAPE density, magnetic susceptibility, natural gamma activity, velocity, and the discrete determinations of thermal conductivity, bulk density, porosity, and water content delineate geotechnical Units G-I and G-II, with the boundary located at about 185 mbsf. In the upper unit, the GRAPE density and discrete bulk-density values averages ~1.9 g/cm^3, and the natural gamma-ray values average around 900 total counts. These fluctuations, which are best seen in Figures 25A and 25D, are of relatively low amplitude and high frequency, with the average wavelength of ~1 m. The porosity averages about 50%, and the water content is ~30%–40% (Fig. 27). No marked decrease with depth is noted, even if the strength of the sediment increases downwards in the unit. This apparent lack of consolidation with depth may suggest that gradual changes in the lithology take place and/or that over-pressure in the pore water occurs in this interval. The geotechnical Unit G-I correlates well with lithologic Unit I, composed of siliciclastic sediments of Pliocene–Quaternary age (see "Lithostratigraphy" section, this chapter).

In geotechnical Unit G-II the GRAPE and discrete bulk densities average ~1.7 g/cm^3 and natural gamma activity values ~800 counts. The fluctuations are of higher amplitude and longer wavelength (~5–15 m) than in geotechnical Unit G-I. This pattern also is recognized in the variations in water content and porosity, whereas the variation in thermal conductivity is less in Unit II than in Unit I. In general, the water content, and thus the porosity, is higher and more variable in Unit II than in Unit I. Geotechnical Unit G-II correlates well with lithologic Unit II, composed of silty clay with intermittent biosiliceous components of late Oligocene age (see "Lithostratigraphy" section, this chapter). The marked decrease in porosity and, consequently, decrease in bulk density and water content observed from ~310 mbsf to the bottom of the hole at 344.6 mbsf may be used to subdivide geotechnical Unit G-II into Subunit G-IIA, from 185 to 310 mbsf, and Subunit G-IIB, from 310 to 344.6 mbsf.

DOWNHOLE MEASUREMENTS

Logging Operations and Log Quality

Three Schlumberger tool strings were run at Hole 908A: the seismic stratigraphic, lithoporosity, and Formation MicroScanner (FMS) combinations. The wireline heave compensator (WHC) was used to counter mild ship heave (0.2–0.5 m of motion). The base of the drill pipe was set at 79 mbsf. The logging tool strings used during Leg 151 are discussed in the "Explanatory Notes" chapter (this volume). A summary of the logging operations at Hole 908A is given in Table 14.

The seismic stratigraphic tool string comprising sonic (DSI), induction (DIT), and natural gamma-ray (NGT) tools, along with the Lamont-Doherty temperature tool (TLT), was run first. Total penetration in Hole 908A was 344.6 mbsf; hole fill or possibly a bridge, however, prevented the tool string from passing below 277.5 mbsf. Data were recorded at a logging speed of 600 ft/hr from this depth to the mud line, with a repeat section over the interval 220.5–151.5 mbsf, less than 79.3 mbsf within the pipe. The sonic and induction data are invalid within the pipe, and the natural gamma-ray data are highly attenuated. The open hole natural gamma-ray data are displayed in Figure 35, and the resistivity data in Figure 33. Data from the DSI tool seem to have been adversely affected by the rugose nature of the borehole (see Fig. 33), and the compressional velocity log was difficult to obtain. Data reported here and used for creating a synthetic seismogram (see "Seismic Stratigraphy" section, this chapter) could be improved by processing the sonic waveform data.

Table 11. Compressional-wave velocity measurements from Hole 908A.

Core, section, interval (cm)	Depth (mbsf)	Tool	Velocity (m/s)	
			Perp	Par
151-908A-				
1H-1, 28–35	0.28	dsv	1697	
1H-1, 111–118	1.11	dsv	1623	
1H-2, 21–28	1.71	dsv	1682	
1H-2, 64–71	2.14	dsv	1558	
1H-3, 25–32	3.25	dsv	1598	
1H-4, 25–32	4.75	dsv	1613	
2H-1, 89–96	6.29	dsv	1648	
2H-2, 80–87	7.70	dsv	1553	
2H-3, 19–26	8.59	dsv	1589	
2H-5, 32–39	11.72	dsv	1662	
2H-6, 30–37	13.20	dsv	1636	
2H-7, 28–35	14.68	dsv	nd	
3H-1, 80–87	15.70	dsv	1632	
3H-2, 70–77	17.10	dsv	1638	
3H-3, 25–32	18.15	dsv	1617	
3H-4, 25–32	19.65	dsv	1574	
3H-5, 29–36	21.19	dsv	1626	
3H-6, 42–49	22.82	dsv	1617	
4H-1, 34–41	24.74	dsv	1672	
4H-2, 35–42	26.25	dsv	1666	
4H-3, 22–29	27.62	dsv	1603	
4H-4, 38–45	29.28	dsv	1605	
4H-5, 25–32	30.65	dsv	1565	
4H-6, 42–49	32.32	dsv	1747	
4H-7, 21–28	33.61	dsv	1716	
5H-1, 34–41	34.24	dsv	1691	
5H-2, 20–27	35.60	dsv	1640	
5H-3, 20–27	37.10	dsv	1624	
5H-4, 20–27	38.60	dsv	1644	
5H-5, 20–27	40.10	dsv	1654	
5H-6, 20–27	41.60	dsv	1712	
5H-6, 85–92	42.25	dsv	1682	
5H-6, 43–50	41.83	dsv	nd	
6H-1, 20–27	43.60	dsv	1763	
6H-1, 52–59	43.92	dsv	1754	
6H-1, 75–82	44.15	dsv	1583	
6H-1, 98–105	44.38	dsv	1727	
6H-2, 20–27	45.10	dsv	1716	
6H-3, 22–29	46.62	dsv	1718	
6H-3, 102–109	47.42	dsv	1740	
6H-4, 30–37	48.20	dsv	1699	
6H-4, 83–90	48.73	dsv	1734	
6H-5, 20–27	49.60	dsv	1632	
6H-5, 102–109	50.42	dsv	1626	
6H-6, 18–25	51.08	dsv	1676	
7H-1, 20–27	53.10	dsv	1742	
7H-1, 88–95	53.78	dsv	1689	
7H-2, 20–27	54.60	dsv	1609	
7H-2, 77–84	55.17	dsv	1658	
7H-3, 50–57	56.40	dsv	1644	
7H-4, 20–27	57.60	dsv	1670	
7H-5, 15–22	59.05	dsv	1611	
7H-5, 25–32	59.15	dsv	1658	
7H-6, 20–27	60.60	dsv	1716	
8H-1, 20–27	62.60	dsv	1676	
8H-2, 20–27	64.10	dsv	1749	
8H-3, 20–27	65.60	dsv	1660	
8H-4, 20–27	67.10	dsv	1695	
8H-5, 28–35	68.68	dsv	1680	
8H-6, 20–27	70.10	dsv	1666	
8H-7, 20–27	71.60	dsv	1809	
9H-1, 20–27	72.10	dsv	1592	
9H-1, 20–22	72.10	ham		1726
9H-2, 120–122	74.60	ham		1587
9H-3, 120–122	76.10	ham		1558
9H-4, 120–122	77.49	ham		1573
9H-5, 125–127	79.04	ham		1599
9H-5, 125–127	79.04	ham		1591
9H-5, 125–127	79.04	ham		1598
9H-5, 125–127	79.04	ham		1595
9H-5, 125–127	79.04	ham		1598
10H-1, 112–114	82.52	ham		1605
10H-2, 117–119	84.07	ham		1580
10H-3, 114–116	85.54	ham		1535
10H-4, 106–108	86.96	ham		1653
10H-5, 126–128	88.66	ham		1535
10H-6, 91–93	89.81	ham		1567
11X-2, 109–111	93.49	ham		1586
11X-3, 76–78	94.66	ham		1628
12X-1, 119–121	101.79	ham		1560
12X-2, 125–127	103.20	ham		1560
12X-3, 110–112	103.80	ham		1426
12X-4, 20–22	105.10	ham		1421
13X-1, 96–98	111.36	ham	1527	
13X-2, 93–95	112.83	ham	1556	
13X-3, 93–95	114.33	ham	1542	
13X-4, 93–95	115.83	ham	1556	
13X-5, 93–95	117.33	ham	nd	
13X-5, 93–95	117.33	ham	1523	
13X-6, 93–95	118.83	ham	1536	
14X-1, 120–122	121.20	ham	1552	
14X-2, 120–122	122.70	ham	1541	
14X-3, 108–110	124.08	ham	1511	
14X-4, 120–122	125.70	ham	1550	
14X-5, 17–19	126.17	ham	1549	
15X-1, 64–66	130.34	ham	1500	
15X-2, 64–66	131.84	ham	1555	
15X-3, 64–66	133.34	ham	1522	
16X-1, 64–66	139.84	ham	1569	
16X-2, 64–66	141.34	ham	1581	
16X-3, 64–66	142.84	ham	1539	
16X-4, 64–66	144.34	ham	1542	
17X-1, 65–67	149.35	ham	1509	
17X-2, 65–67	150.85	ham	1560	
17X-3, 65–67	152.35	ham	1550	
17X-4, 65–67	153.85	ham	1538	
17X-5, 65–67	155.35	ham	1496	
17X-6, 65–67	156.85	ham	1537	
17X-7, 17–19	157.87	ham	1563	
18X-1, 64–66	158.84	ham	1543	
18X-2, 64–66	160.34	ham	1524	
18X-3, 64–66	161.84	ham	1607	
18X-4, 15–17	162.85	ham	1467	
18X-5, 64–66	164.84	ham	1546	
18X-6, 64–66	166.34	ham	1488	
18X-6, 64–66	166.34	ham	1537	
18X-7, 17–19	167.37	ham	1565	
19X-1, 99–101	168.79	ham	1511	
19X-1, 99–101	168.79	ham	1522	
19X-2, 99–101	170.29	ham	1558	
19X-3, 99–101	171.79	ham	1555	
19X-4, 99–101	173.29	ham	1575	
19X-5, 99–101	174.79	ham	1599	
20X-1, 55–57	177.95	ham	1553	
20X-2, 77–79	179.67	ham	1584	
20X-3, 73–75	181.13	ham	1561	
20X-4, 78–80	182.68	ham	1542	
20X-5, 76–78	184.16	ham	1562	
21X-2, 126–128	189.86	ham	1464	
21X-2, 126–128	189.86	ham	1495	
21X-3, 119–121	191.29	ham	1481	
21X-3, 119–121	191.29	ham	1486	
21X-3, 119–121	191.29	ham	1524	
21X-5, 33–35	193.43	ham	1500	
22X-1, 120–122	197.90	ham	1567	
22X-2, 133–135	199.53	ham	1483	
22X-3, 134–136	201.04	ham	1512	
22X-4, 121–123	202.41	ham	1553	
22X-5, 123–125	203.93	ham	1584	
23X-1, 88–90	207.18	ham	1554	
23X-2, 95–97	208.75	ham	1532	
23X-3, 93–95	210.23	ham	1506	
23X-4, 92–94	211.72	ham	1509	
23X-5, 91–93	213.21	ham	1527	
23X-5, 91–93	213.21	ham	1495	
24X-1, 41–43	216.41	ham	1536	
24X-2, 41–43	217.91	ham	1575	
24X-3, 70–72	219.70	ham	1510	
24X-4, 114–116	221.64	ham	1467	
24X-5, 112–114	223.12	ham	1501	
24X-6, 24–26	223.74	ham	1507	
25X-1, 41–43	226.01	ham	1512	
25X-2, 39–41	227.49	ham	1507	
25X-3, 10–12	228.70	ham	1551	
25X-4, 9–11	230.19	ham	1505	
25X-6, 18–20	233.28	ham	1505	
25X-5, 12–14	231.72	ham	1491	
26X-1, 53–55	235.73	ham	1516	
26X-2, 17–19	236.87	ham	1516	
26X-3, 62–64	238.82	ham	1479	
26X-4, 38–40	240.08	ham	1570	
26X-5, 82–84	242.02	ham	1577	
26X-6, 54–56	243.24	ham	1595	
27X-5, 23–25	251.13	ham	1470	
27X-1, 37–39	245.27	ham	1611	
27X-2, 27–29	246.67	ham	1420	
27X-3, 23–25	248.13	ham	1496	
27X-4, 21–23	249.61	ham	1443	
28X-1, 51–53	255.11	ham	1509	
28X-2, 40–42	256.50	ham	1634	
28X-3, 42–44	258.02	ham	1636	
28X-4, 113–115	260.23	ham	1507	
28X-5, 58–60	261.18	ham	1491	
28X-1, 24–26	254.84	ham	1536	
28X-6, 51–53	262.61	ham	1492	

Table 11 (continued).

Core, section, interval (cm)	Depth (mbsf)	Tool	Velocity (m/s)	
			Perp	Par
29X-1, 73–75	264.93	ham	1561	
29X-2, 84–86	266.54	ham	1585	
29X-3, 40–42	267.60	ham	1630	
29X-4, 91–93	269.61	ham	1534	
29X-5, 94–96	271.14	ham	1493	
29X-5, 99–101	271.19	ham	1527	
30X-1, 82–84	274.72	ham	1512	
30X-2, 92–94	276.32	ham	1507	
30X-3, 104–106	277.94	ham	1501	
30X-4, 27–29	278.67	ham	1475	
30X-5, 86–88	280.76	ham	1644	
30X-7, 38–40	283.28	ham	1585	
30X-6, 50–52	281.90	ham	1581	
31X-1, 42–44	283.92	ham	1568	
31X-2, 134–136	286.34	ham	1587	
31X-3, 96–98	287.46	ham	1629	
31X-5, 114–116	290.64	ham	1748	
31X-6, 97–99	291.97	ham	1527	
31X-7, 23–25	292.73	ham	1491	
32X-1, 37–39	293.57	ham	1500	
32X-2, 51–53	295.21	ham	1503	
32X-3, 62–64	296.82	ham	1500	
32X-4, 80–82	298.50	ham	1517	
32X-5, 86–88	300.06	ham	1539	
32X-6, 116–118	301.86	ham	1607	
32X-7, 20–22	302.40	ham	1532	
33X-1, 92–94	303.72	ham	1498	
33X-2, 118–120	305.48	ham	1516	
33X-3, 135–137	307.15	ham	1489	
33X-4, 71–73	308.01	ham	1523	
33X-5, 95–97	309.75	ham	1501	
33X-6, 97–99	311.27	ham	1477	
34X-1, 77–79	313.27	ham	1671	
34X-2, 52–54	314.52	ham	1527	
34X-3, 56–58	316.06	ham	1509	
34X-4, 53–55	317.53	ham	1543	
34X-5, 51–53	319.03	ham	1527	

Note: Tool = device used for measurement, either dsv = digital sound velocimeter or ham = Hamilton Frame. Perp = perpendicular, Par = parallel. nd = not determined.

The lithodensity tool string, consisting of NGT, density (HLDT), and neutron porosity (CNT) tools, together with the TLT, was run next. The tool string reached a depth of 229 mbsf where a bridge stopped downward progress. One pass was recorded from this depth at a logging speed of 900 ft/hr to the base of pipe at 79.3 mbsf. The HLDT was run in high-resolution mode, recording data at 1.2-in. increments. The bulk density and neutron porosity data are displayed in Figure 33. The recorded data are generally of good quality, although

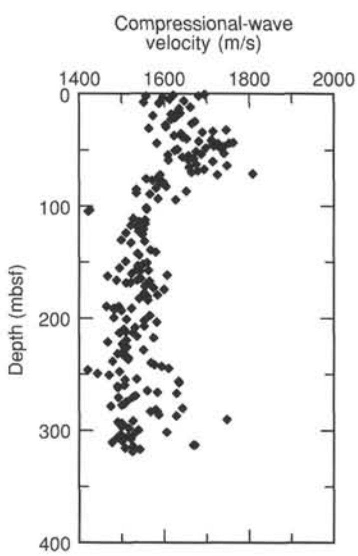

Figure 29. Laboratory measurements of velocity in Hole 908A.

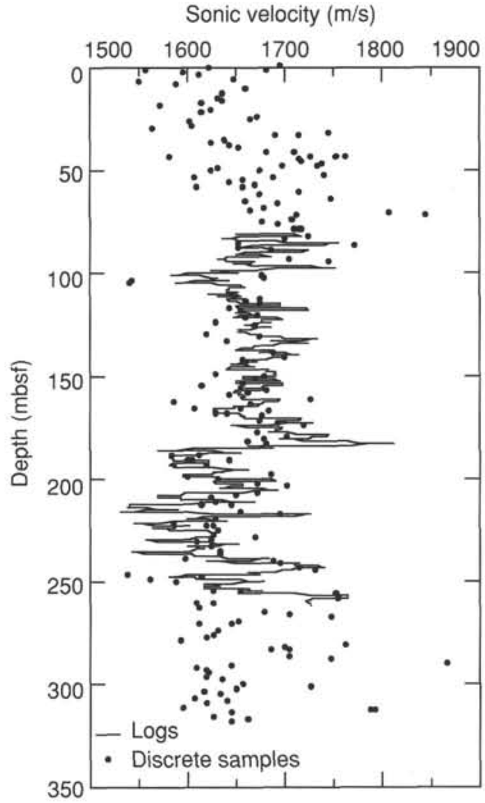

Figure 30. Comparison between sonic velocity measured in situ by logging and the adjusted discrete velocities measured on core (see text). Within the interval common to both sets of data, the two measurements agree well in terms of location and amplitude of velocity changes within the profile.

the density and neutron porosity data are not reliable in the interval where the eccentralizing caliper arm was retracted, between 93 and 79 mbsf (Fig. 33). The density profile also is adversely affected in intervals of borehole diameter that are larger than the maximum caliper extension (16 in.). Where such washouts occur, good contact of the HLDT arm with the borehole wall is less certain, resulting in anomalously low bulk-density readings (e.g., 100 mbsf; 214 mbsf). The neutron porosity data appear similarly affected but to a less severe degree.

After the lithodensity run, the hole was reamed out to clear bridges that were forming, apparent from the caliper data of the HLDT (Fig. 33). The FMS with an NGT tool was then run into the hole but was unable to pass an obstruction at 177 mbsf. Two full passes were recorded at 1400 ft/hr from this depth to the end of pipe (pulled up to 59 mbsf). The FMS microresistivity images generally appear of good quality, but are degraded in places by the rugose borehole, which occasionally exceeded the maximum extension of the FMS caliper arms. Where this occurs, the contact of the FMS pads with the borehole wall is poor, degrading the image quality. No time was available to run the geochemical logging tool in Hole 908A.

Results

Borehole Temperature

The TLT was deployed on two of the three tool strings run in Hole 908A. Data were recorded successfully only on the seismic stratigraphic tool string, giving a mud line temperature of –1.43°C and a bottom-hole (270 mbsf) temperature of 5.31°C. An accurate thermal gradient cannot be obtained from this single measurement because cold seawater is circulated in the hole during drilling, thus cooling the adjacent formation; a minimum of three bottom-hole-temperature

Table 12. Shear strength measurements from Hole 908A

Core, section, interval (cm)	Depth (mbsf)	SN	Vane (kPa)	Res (kPa)	Pen (kPa)
151-908A-					
1H-1, 100–101	0.96	3	6	4	
1H-2, 68–69	2.18	3	3	1	
1H-3, 85–86	3.85	3	5	5	
1H-4, 36–37	4.86	3	5	4	
2H-1, 92–93	6.31	3	7	5	
2H-2, 130–94	8.20	3	9	6	
2H-3, 128–129	9.68	3	13	12	
2H-4, 120–121	11.10	3	17	4	
2H-5, 8–9	11.48	3	18	11	
2H-6, 101–102	14.01	3	15	11	
2H-7, 59–60	14.99	3	14	7	
3H-1, 83–84	15.73	3	18	9	13
3H-2, 130–131	17.60	3	19	11	30
3H-3, 119–120	19.09	3	21	10	18
3H-4, 120–121	20.60	3	14	5	13
3H-5, 114–115	22.04	3	23	13	18
3H-6, 66–67	23.06	3	29	15	22
4H-1, 98–99	25.38	3	32	14	
4H-2, 95–96	26.85	3	32	8	27
4H-3, 83–84	28.23	3	22	14	16
4H-4, 101–102	29.91	3	24	17	20
4H-5, 93–94	31.33	3	22	14	16
4H-6, 107–108	32.97	3	26	10	30
4H-7, 25–26	33.65	3	35	12	39
5H-1, 35–36	34.35	3	27	7	30
5H-1, 125–126	36.65	3	24		
5H-2, 25–26	37.15	3	29	6	25
5H-3, 25–26	38.65	3	28	5	34
5H-4, 25–26	40.15	3	24	10	32
5H-5, 23–24	41.63	3	28	9	30
5H-5, 99–100	42.39	3	27	0	28
5H-6, 88–89	44.28	3	27	11	27
6H-1, 25–26	43.65	3	53	3	49
6H-2, 25–26	45.15	3	89	40	49
6H-2, 50–51	47.00	4	87	47	61
6H-3, 102–103	47.42	4	67	27	56
6H-3, 25–26	48.15	4	32	11	34
6H-4, 87–88	48.78	4	83	38	59
6H-5, 105–106	50.45	4	70	32	37
6H-5, 25–26	49.65	4	66	30	47
6H-6, 22–23	51.12	4	60	28	52
7H-1, 18–19	53.08	4	68	26	60
7H-2, 25–26	54.65	4	89	32	74
7H-3, 55–56	56.45	4	66	28	57
7H-4, 20–21	57.60	4	73	23	49
7H-5, 18–19	59.08	4	99	23	79
7H-6, 78–79	61.18	4	110	38	64
8H-1, 46–47	62.68	4	77	34	52
8H-2, 25–26	64.15	4	115	45	76
8H-3, 80–81	66.20	4	100	42	87
8H-4, 80–81	67.70	4	87	38	66
8H-4, 25–26	67.15	4	80	32	
8H-5, 80–81	69.20	4	104	44	74
8H-6, 80–81	70.70	4	80	36	61
8H-7, 25–26	71.65	4	144	74	201
9H-3, 50–51	75.40	4	132	30	93
9H-3, 62–63	75.52	4	112	46	91
9H-4, 62–63	76.91	4	148	61	110
9H-5, 50–51	78.29	4	137	60	101
10H-1, 117–118	82.57				116
10H-2, 116–117	84.08				79
10H-3, 118–119	85.58				67
10H-4, 115–116	86.85				109
10H-5, 110–111	88.50				92
10H-6, 87–88	89.77				55
11X-2, 129–130	93.59				64
11X-3, 75–76	94.65				62
12X-1, 20–21	100.80				81
12X-2, 20–21	102.15				121
12X-3, 20–21	102.90				82
12X-4, 15–16	105.05				92
13X-1, 100–101	111.40				77
13X-2, 100–101	112.90				137
13X-3, 100–101	114.40				103
13X-4, 100–101	115.90				103
13X-5, 100–101	117.40				113
13X-6, 100–101	118.90				109
14X-1, 23–24	120.23				113
14X-2, 12–13	121.62				99
14X-3, 12–13	123.12				132
14X-4, 12–13	124.72				111
14X-5, 12–13	126.12				128
15X-1, 67–68	130.37				132
15X-2, 67–68	131.87				113
15X-3, 67–68	133.37				145
16X-1, 71–72	139.91				160
16X-2, 71–72	141.41				143
16X-3, 71–72	142.91				196
16X-4, 71–72	144.44				159
17X-1, 70–71	149.40				164
17X-2, 70–71	150.90				182
17X-3, 70–71	152.40				118
17X-4, 70–71	153.90				137
17X-5, 70–71	155.40				141
17X-6, 70–71	156.90				152
17X-7, 14–15	157.84				170
18X-1, 15–16	158.35				127
18X-2, 15–16	159.85				181
18X-3, 15–16	161.35				164
18X-4, 12–13	162.82				135
18X-5, 15–16	164.35				169
18X-6, 15–16	165.85				198
18X-7, 15–16	167.35				181
19X-1, 30–31	168.10				172
19X-2, 30–31	169.60				181
19X-3, 30–31	171.10				168
19X-4, 30–31	172.60				179
19X-5, 30–31	174.10				196
19X-6, 30–31	175.60				201
20X-1, 22–23	177.62				196
20X-2, 35–36	179.25				186
20X-3, 22–23	180.62				204
20X-4, 22–23	182.12				211
20X-5, 22–23	183.62				191
20X-6, 31–32	185.21				132

Notes: SN = numbered spring used to make the measurement. Vane = undrained shear strength; Res = residual shear strength; Pen = unconfined shear strength as measured by the penetrometer.

measurements over a period of time are required to extrapolate the true bottom-hole temperature and, hence, calculate the true thermal gradient.

Lithology

The interval logged in Hole 908A (79–277.5 mbsf) covers lithostratigraphic Units IB to II (see "Lithostratigraphy" section, this chapter). The most prominent feature of the section is the angular unconformity identified in seismic reflection profiles. This unconformity, marking the boundary between lithologic Units I and II, occurs at about 185 mbsf in the cored section and is a prominent feature in all of the log data at about 185 mbsf.

Sedimentary Units IB (81.4–139.2 mbsf) and IC (139.2–185 mbsf) of Pliocene age are characterized by high clay contents (~60%) along with quartz and feldspar, with virtually no biogenic component. Unit IB contains the oldest dropstones observed in this hole. The high-count rate of total gamma-ray log (Fig. 35), bulk densities of 1.8–1.9 g/cm^3, and porosities of ~50% reflect the high clay content in the unit. Units IB and IC can be differentiated in the logs by a subtle downward decrease in bulk density and increase in neutron porosity and hole diameter.

Notable in this upper interval is the cyclic nature of logs. Figure 34 shows the shallow-focused resistivity, high-resolution bulk density, and total gamma-ray logs for the interval 100–150 mbsf. The shallow-focused resistivity log shows a very well-defined, high-frequency cyclic component having a wavelength of 0.5–1.5 m. This is reflected well in the gamma-ray log where it is superimposed on cycles with a wavelength 9–10 m. The resistivity log cyclicity is a result of subtle porosity changes in the formation caused by mineralogical and/or textural variations. The origin of the cyclicity may well be

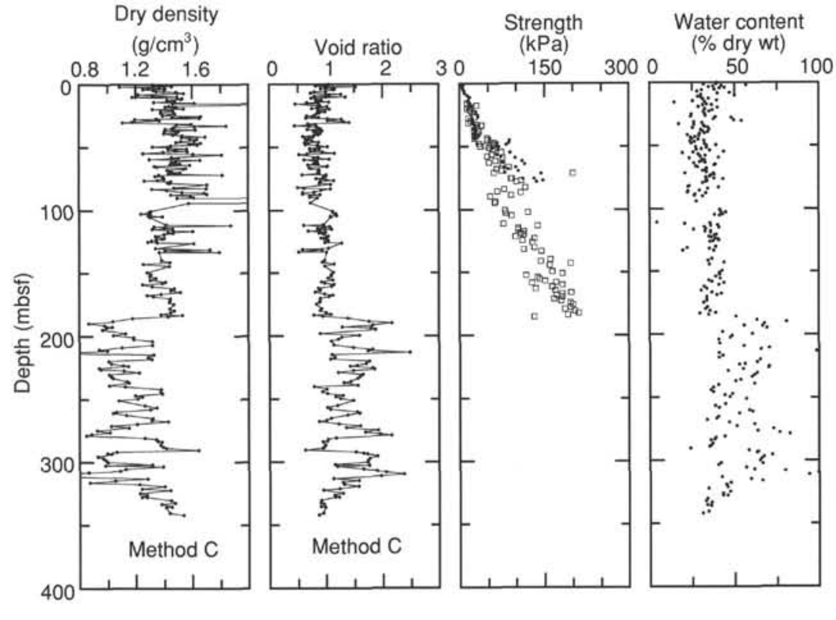

Figure 31. Comparison of combined vane shear (closed circles) and penetrometer (open squares) strength measurements, on discrete samples, of dry density, void ratio, and water content (% dry) vs. depth in Hole 908A.

Table 13. Index properties measured for Holes 908A and 908B.

Core, section, interval (cm)	Depth (mbsf)	WC-d (%)	WC-w (%)	WBD[a] (g/cm³)	WBD[b] (g/cm³)	GD[a] (g/cm³)	GD[b] (g/cm³)	DBD[a] (g/cm³)	DBD[b] (g/cm³)	Por[a] (%)	Por[b] (%)	VR[a]	VR[b]
151-908A-													
1H-1, 33–35	0.33	39.92	28.53	1.90	1.85	2.87	2.71	1.36	1.32	52.80	51.38	1.12	1.06
1H-1, 116–118	1.16	39.18	28.15	1.89	1.85	2.82	2.70	1.36	1.33	51.84	50.75	1.08	1.03
1H-2, 35–37	1.85	31.67	24.05	1.97	1.91	2.77	2.64	1.49	1.45	46.12	44.91	0.86	0.82
1H-2, 78–80	2.28	56.97	36.29	1.71	1.70	2.76	2.74	1.09	1.09	60.50	60.34	1.53	1.52
1H-2, 138–140	2.88	42.17	29.66	1.87	1.83	2.86	2.73	1.31	1.29	54.06	52.94	1.18	1.12
1H-3, 29–31	3.29	37.17	27.10	1.93	1.88	2.86	2.73	1.40	1.37	50.94	49.73	1.04	0.99
1H-3, 63–65	3.63	34.61	25.71	1.92	1.90	2.74	2.70	1.42	1.41	48.08	47.66	0.93	0.91
1H-3, 108–110	4.08	43.89	30.50	1.83	1.80	2.80	2.69	1.27	1.25	54.56	53.53	1.20	1.15
1H-4, 34–36	4.84	41.01	29.09	1.84	1.87	2.72	2.82	1.30	1.33	52.13	53.02	1.09	1.13
2H-1, 18–20	5.58	37.96	27.51	1.90	1.86	2.81	2.69	1.38	1.35	51.00	49.95	1.04	1.00
2H-1, 94–96	6.34	30.64	23.45	2.00	1.94	2.83	2.67	1.53	1.49	45.82	44.42	0.85	0.80
2H-2, 39–41	7.29	28.06	21.91	2.01	1.98	2.76	2.67	1.57	1.54	43.03	42.24	0.76	0.73
2H-2, 129–131	8.19	47.04	31.99	1.83	1.79	2.90	2.75	1.24	1.22	57.11	55.83	1.33	1.26
2H-3, 22–24	8.62	40.00	28.57	1.89	1.85	2.86	2.72	1.35	1.32	52.72	51.52	1.11	1.06
2H-3, 128–130	9.68	30.45	23.34	1.99	1.95	2.79	2.69	1.53	1.50	45.34	44.43	0.83	0.80
2H-4, 52–54	10.42	50.03	33.35	1.81	1.77	2.94	2.76	1.21	1.18	58.94	57.42	1.44	1.35
2H-4, 120–122	11.10	28.43	22.14	2.02	1.97	2.78	2.66	1.57	1.53	43.56	42.46	0.77	0.74
2H-5, 36–38	11.76	30.30	23.25	2.00	1.98	2.81	2.76	1.54	1.52	45.39	44.97	0.83	0.82
2H-5, 133–135	12.73	34.61	25.71	1.97	1.91	2.89	2.73	1.46	1.42	49.37	48.00	0.98	0.92
2H-6, 33–35	13.23	31.43	23.91	1.99	1.94	2.82	2.70	1.51	1.48	46.39	45.26	0.87	0.83
2H-6, 129–131	14.19	39.56	28.34	1.91	1.86	2.91	2.73	1.37	1.33	52.93	51.32	1.12	1.05
2H-7, 30–32	14.70	25.29	20.19	2.07	2.02	2.79	2.69	1.65	1.62	40.76	39.86	0.69	0.66
3H-1, 49–51	15.39	32.68	24.63	1.88	1.94	2.59	2.74	1.42	1.46	45.19	46.65	0.82	0.87
3H-1, 83–85	15.73	14.52	12.68	1.79	2.55	2.00	3.25	1.56	2.23	22.12	31.56	0.28	0.46
3H-2, 75–77	17.15	33.70	25.20	1.94	1.92	2.78	2.72	1.45	1.44	47.77	47.20	0.91	0.89
3H-2, 129–131	17.69	31.56	23.99	1.99	1.96	2.83	2.75	1.51	1.49	46.59	45.81	0.87	0.85
3H-3, 28–30	18.18	36.66	26.82	1.92	1.93	2.83	2.85	1.41	1.41	50.30	50.50	1.01	1.02
3H-3, 139–141	19.29	28.62	22.25	2.09	1.98	2.98	2.70	1.63	1.54	45.38	42.97	0.83	0.75
3H-4, 37–39	19.77	40.06	28.60	1.90	1.85	2.87	2.73	1.35	1.32	52.88	51.66	1.12	1.07
3H-4, 121–123	20.61	32.33	24.43	2.00	1.94	2.90	2.73	1.51	1.47	47.77	46.24	0.91	0.86
3H-5, 33–35	21.23	32.42	24.48	2.01	1.94	2.91	2.72	1.51	1.46	47.89	46.28	0.92	0.86
3H-5, 115–117	22.05	36.95	26.98	1.96	1.89	2.96	2.73	1.43	1.38	51.58	49.62	1.07	0.99
3H-6, 46–48	22.86	34.95	25.90	1.97	1.86	2.92	2.60	1.46	1.38	49.89	46.98	1.00	0.89
3H-6, 113–115	23.53	31.71	24.08	2.05	1.94	3.00	2.72	1.56	1.48	48.13	45.68	0.93	0.84
4H-1, 39–41	24.79	32.52	24.54	2.03	1.85	2.97	2.50	1.53	1.39	48.50	44.23	0.94	0.79
4H-1, 98–100	25.38	24.45	19.64	2.16	2.07	2.96	2.76	1.73	1.66	41.37	39.66	0.71	0.66
4H-2, 39–41	26.29	32.70	24.64	2.05	1.94	3.05	2.73	1.55	1.46	49.35	46.57	0.97	0.87
4H-2, 95–97	26.85	24.25	19.52	2.18	2.06	2.99	2.72	1.75	1.66	41.44	39.16	0.71	0.64
4H-3, 26–28	27.66	38.70	27.90	1.94	1.87	2.96	2.74	1.40	1.35	52.76	50.89	1.12	1.04
4H-3, 83–85	28.23	48.01	32.44	1.86	1.77	3.05	2.72	1.26	1.20	58.81	55.99	1.43	1.27
4H-4, 41–43	29.31	37.90	27.49	1.99	1.89	3.09	2.77	1.44	1.37	53.36	50.63	1.14	1.03
4H-4, 99–101	29.89	49.63	33.17	1.85	1.76	3.07	2.72	1.23	1.17	59.77	56.87	1.49	1.32
4H-5, 27–29	30.67	54.04	35.08	1.82	1.71	3.15	2.68	1.18	1.11	62.43	58.54	1.66	1.41
4H-5, 114–116	31.54	26.00	20.64	2.09	2.01	2.87	2.68	1.66	1.59	42.12	40.46	0.73	0.68
4H-6, 32–34	32.22	30.84	23.57	2.05	1.95	2.96	2.70	1.57	1.49	47.11	44.81	0.89	0.81
4H-6, 106–108	32.96	17.16	14.65	1.99	2.16	2.38	2.67	1.70	1.84	28.49	30.87	0.40	0.45
4H-7, 25–27	33.65	26.18	20.75	2.14	2.04	2.99	2.76	1.70	1.62	43.33	41.37	0.76	0.71
5H-1, 25–27	34.15	31.76	24.10	1.99	1.94	2.84	2.71	1.51	1.47	46.77	45.62	0.88	0.84
5H-1, 99–101	34.89	32.67	24.63	1.98	1.94	2.85	2.73	1.49	1.46	47.63	46.57	0.91	0.87
5H-2, 25–27	35.65	34.53	25.66	1.97	1.90	2.90	2.69	1.47	1.41	49.44	47.52	0.98	0.91
5H-2, 99–101	36.39	25.27	20.17	2.11	2.04	2.89	2.71	1.69	1.62	41.59	40.05	0.71	0.67

Table 13 (continued).

Core, section, interval (cm)	Depth (mbsf)	WC-d (%)	WC-w (%)	WBD[a] (g/cm^3)	WBD[b] (g/cm^3)	GD[a] (g/cm^3)	GD[b] (g/cm^3)	DBD[a] (g/cm^3)	DBD[b] (g/cm^3)	Por[a] (%)	Por[b] (%)	VR[a]	VR[b]
5H-3, 25–27	37.15	35.09	25.97	1.96	1.90	2.88	2.72	1.45	1.41	49.62	48.19	0.98	0.93
5H-3, 99–101	37.89	30.11	23.14	2.03	1.95	2.87	2.69	1.56	1.50	45.78	44.13	0.84	0.79
5H-4, 25–27	38.65	31.36	23.87	2.00	1.95	2.84	2.73	1.52	1.49	46.53	45.49	0.87	0.83
5H-4, 99–101	39.39	34.50	25.65	1.97	1.89	2.88	2.66	1.46	1.40	49.25	47.23	0.97	0.89
5H-5, 25–27	40.15	32.47	24.51	2.01	1.94	2.92	2.73	1.52	1.46	48.01	46.34	0.92	0.86
5H-5, 97–99	40.87	29.60	22.84	2.06	1.98	2.94	2.75	1.59	1.53	45.96	44.22	0.85	0.79
5H-6, 45–47	41.85	22.43	18.32	2.13	2.08	2.80	2.70	1.74	1.70	38.02	37.11	0.61	0.59
5H-6, 99–101	42.39	29.16	22.58	2.04	1.97	2.86	2.70	1.58	1.53	44.86	43.46	0.81	0.77
5H-7, 25–27	43.15	26.84	21.16	2.05	2.01	2.79	2.71	1.61	1.58	42.24	41.51	0.73	0.71
6H-1, 24–26	43.64	24.31	19.56	2.13	2.03	2.90	2.67	1.72	1.64	40.73	38.80	0.69	0.63
6H-1, 99–101	44.39	25.18	20.11	2.08	2.03	2.81	2.69	1.66	1.62	40.82	39.77	0.69	0.66
6H-2, 26–28	45.16	28.73	22.32	2.03	1.96	2.83	2.66	1.58	1.52	44.24	42.73	0.79	0.75
6H-2, 99–101	45.89	32.24	24.38	2.02	1.97	2.95	2.79	1.53	1.49	48.09	46.77	0.93	0.88
6H-3, 24–26	46.64	23.82	19.24	2.13	2.06	2.86	2.70	1.72	1.66	39.93	38.59	0.66	0.63
6H-3, 99–101	47.39	26.51	20.95	2.06	2.00	2.81	2.67	1.63	1.58	42.11	40.89	0.73	0.69
6H-4, 26–28	48.16	24.45	19.65	2.08	2.04	2.77	2.69	1.67	1.64	39.80	39.10	0.66	0.64
6H-4, 99–101	48.89	32.48	24.52	1.94	1.92	2.74	2.68	1.47	1.45	46.44	45.94	0.87	0.85
6H-5, 26–28	49.66	39.33	28.23	1.86	1.84	2.74	2.67	1.34	1.32	51.27	50.64	1.05	1.03
6H-5, 99–101	50.39	33.65	25.18	1.92	1.91	2.73	2.69	1.44	1.43	47.23	46.86	0.89	0.88
6H-6, 26–28	51.16	27.31	21.45	1.83	1.99	2.34	2.68	1.44	1.56	38.37	41.64	0.62	0.71
6H-6, 99–101	51.89	33.66	25.18	1.97	1.92	2.86	2.71	1.47	1.43	48.41	47.06	0.94	0.89
6H-7, 26–28	52.66	30.74	23.51	2.27	1.94	3.64	2.67	1.74	1.48	52.16	44.49	1.09	0.80
7H-1, 26–28	53.16	27.48	21.55	2.08	2.00	2.89	2.71	1.63	1.57	43.69	42.08	0.78	0.73
7H-1, 100–102	53.90	35.55	26.23	2.02	1.89	3.09	2.71	1.49	1.40	51.77	48.45	1.07	0.94
7H-2, 24–26	54.64	43.71	30.41	1.92	1.80	3.12	2.70	1.34	1.25	57.09	53.50	1.33	1.15
7H-2, 99–101	55.39	25.62	20.40	2.09	2.02	2.85	2.69	1.66	1.61	41.59	40.23	0.71	0.67
7H-3, 19–21	56.09	19.53	16.34	2.27	2.16	2.97	2.76	1.90	1.81	36.11	34.46	0.57	0.53
7H-4, 24–26	57.64	32.72	24.65	2.04	1.93	3.02	2.71	1.54	1.45	49.07	46.42	0.96	0.87
7H-4, 99–101	58.39	29.89	23.01	2.06	1.96	2.95	2.68	1.58	1.51	46.20	43.89	0.86	0.78
7H-5, 24–26	59.14	40.89	29.02	1.91	1.83	2.97	2.69	1.36	1.30	54.20	51.72	1.18	1.07
7H-5, 99–101	59.89	23.43	18.98	2.13	2.05	2.86	2.67	1.73	1.66	39.50	37.91	0.65	0.61
7H-6, 24–26	60.64	31.12	23.73	2.00	1.95	2.83	2.71	1.52	1.49	46.20	45.09	0.86	0.82
7H-6, 99–101	61.39	32.35	24.44	2.02	1.93	2.95	2.70	1.53	1.46	48.17	45.99	0.93	0.85
7H-7, 24–26	62.14	30.98	23.65	2.04	1.93	2.94	2.67	1.56	1.48	47.05	44.64	0.89	0.81
8H-1, 24–26	62.64	29.61	22.85	2.07	1.96	2.95	2.69	1.59	1.51	46.05	43.74	0.85	0.78
8H-1, 99–101	63.39	32.92	24.77	1.99	1.92	2.88	2.70	1.50	1.45	48.02	46.41	0.92	0.87
8H-2, 24–26	64.14	26.19	20.76	2.09	2.00	2.87	2.67	1.66	1.59	42.34	40.52	0.73	0.68
8H-2, 102–104	64.92	38.95	28.03	1.95	1.85	3.01	2.70	1.40	1.33	53.33	50.62	1.14	1.02
8H-3, 24–26	65.64	38.24	27.66	1.97	1.87	3.06	2.73	1.43	1.35	53.27	50.42	1.14	1.02
8H-3, 101–103	66.41	27.13	21.34	2.09	1.98	2.92	2.66	1.65	1.56	43.57	41.30	0.77	0.70
8H-4, 24–26	67.14	28.19	21.99	2.10	1.97	2.98	2.67	1.64	1.54	45.05	42.35	0.82	0.73
8H-4, 99–101	67.89	33.62	25.16	1.97	1.90	2.85	2.67	1.47	1.42	48.31	46.69	0.93	0.88
8H-5, 24–26	68.64	33.46	25.07	2.04	1.91	3.05	2.70	1.53	1.43	49.90	46.84	1.00	0.88
8H-5, 99–101	69.39	32.78	24.69	2.03	1.93	2.99	2.71	1.53	1.45	48.92	46.45	0.96	0.87
8H-6, 24–26	70.14	31.35	23.87	2.02	1.99	2.90	2.83	1.54	1.52	46.97	46.40	0.89	0.87
8H-6, 99–101	70.89	33.60	25.15	2.00	1.91	2.94	2.70	1.50	1.43	49.08	46.91	0.96	0.88
8H-7, 37–39	71.77	20.75	17.18	2.25	2.19	2.99	2.87	1.86	1.81	37.70	36.71	0.61	0.58
9H-1, 24–26	72.14	37.65	27.35	1.94	1.88	2.93	2.73	1.41	1.36	51.85	50.07	1.08	1.00
9H-1, 99–101	72.89	38.22	27.65	1.96	1.85	2.99	2.68	1.41	1.34	52.75	50.00	1.12	1.00
9H-2, 24–26	73.64	36.23	26.60	1.94	1.89	2.86	2.73	1.42	1.39	50.30	49.12	1.01	0.97
9H-2, 99–101	74.39	35.60	26.26	2.05	1.90	3.17	2.74	1.51	1.40	52.39	48.75	1.10	0.95
9H-3, 26–28	75.16	33.27	24.96	2.11	1.87	3.27	2.57	1.59	1.40	51.48	45.44	1.06	0.83
9H-3, 99–101	75.89	37.99	27.53	1.93	1.87	2.90	2.73	1.40	1.36	51.79	50.32	1.07	1.01
9H-4, 24–26	76.53	43.30	30.22	1.92	1.81	3.10	2.71	1.34	1.26	56.73	53.36	1.31	1.14
9H-4, 99–101	77.28	33.62	25.16	2.11	1.94	3.27	2.77	1.58	1.45	51.74	47.62	1.07	0.91
9H-5, 24–26	78.03	34.14	25.45	1.99	1.92	2.93	2.73	1.48	1.43	49.40	47.64	0.98	0.91
9H-5, 99–101	78.78	33.36	25.02	1.99	1.93	2.91	2.72	1.50	1.44	48.66	46.99	0.95	0.89
9H-6, 20–22	79.49	31.34	23.86	2.02	2.24	2.89	3.57	1.53	1.71	46.93	52.17	0.88	1.09
10H-1, 44–46	81.84	23.43	18.98	2.13	1.82	2.85	2.22	1.73	1.47	39.44	33.66	0.65	0.51
10H-1, 114–116	82.54	22.86	18.60	2.12	2.09	2.81	2.75	1.73	1.70	38.54	37.97	0.63	0.61
10H-2, 37–39	83.27	40.56	28.86	1.91	1.85	2.93	2.74	1.36	1.31	53.66	52.01	1.16	1.08
10H-2, 117–119	84.07	34.45	25.62	1.97	1.91	2.89	2.72	1.47	1.42	49.28	47.80	0.97	0.92
10H-3, 114–116	85.54	29.63	22.86	2.04	1.99	2.88	2.75	1.57	1.53	45.44	44.32	0.83	0.80
10H-4, 32–34	86.22	22.64	18.46	2.15	2.07	2.86	2.69	1.75	1.69	38.70	37.30	0.63	0.59
10H-4, 106–108	86.96	22.39	18.29	2.14	2.09	2.82	2.72	1.75	1.71	38.13	37.30	0.62	0.59
10H-5, 29–31	87.69	33.37	25.02	2.00	1.93	2.92	2.74	1.50	1.45	48.71	47.17	0.95	0.89
10H-5, 115–117	88.55	26.94	21.22	2.08	2.02	2.89	2.73	1.64	1.59	43.16	41.78	0.76	0.72
10H-6, 90–92	89.80	26.48	20.94	2.04	2.04	2.77	2.76	1.61	1.61	41.72	41.60	0.72	0.71
10H-0, 23–25	90.30	31.51	23.96	2.00	1.97	2.86	2.76	1.52	1.49	46.76	45.94	0.88	0.85
11X-3, 10–12	94.00	27.48	21.55	2.06	2.01	2.86	2.73	1.62	1.58	43.42	42.23	0.77	0.73
12X-1, 31–33	100.91	41.32	29.24	1.92	1.85	3.01	2.77	1.36	1.31	54.80	52.73	1.21	1.12
12X-1, 118–120	101.78	41.87	29.51	1.89	1.83	2.93	2.74	1.33	1.29	54.48	52.78	1.20	1.12
12X-2, 53–55	102.63	44.88	30.98	1.85	1.79	2.91	2.69	1.28	1.24	56.04	54.09	1.27	1.18
12X-2, 124–126	103.34	42.41	29.78	1.89	1.86	2.95	2.83	1.33	1.30	54.99	53.89	1.22	1.17
12X-3, 69–71	104.29	43.06	30.10	1.92	1.85	3.09	2.82	1.35	1.29	56.52	54.21	1.30	1.18
12X-3, 110–112	104.70	38.23	27.66	1.98	1.92	3.07	2.88	1.43	1.39	53.38	51.78	1.15	1.07
12X-4, 21–23	105.31	41.17	29.16	1.89	1.83	2.91	2.71	1.34	1.30	53.88	52.12	1.17	1.09
13X-1, 95–97	111.35	35.27	26.07	1.96	1.91	2.90	2.76	1.45	1.42	49.94	48.70	1.00	0.95
13X-2, 28–30	112.18	20.64	17.11	1.97	2.26	2.44	3.01	1.64	1.87	32.95	37.75	0.49	0.61
13X-2, 94–96	112.84	39.91	28.52	1.90	1.86	2.89	2.75	1.36	1.33	52.95	51.67	1.13	1.07
13X-3, 28–30	113.68	36.04	26.49	1.97	1.90	2.95	2.76	1.45	1.40	50.91	49.23	1.04	0.97
13X-3, 94–96	114.34	32.18	24.35	1.99	1.93	2.85	2.70	1.51	1.46	47.27	45.88	0.90	0.85
13X-4, 28–30	115.18	40.63	28.89	1.91	1.85	2.95	2.76	1.36	1.32	53.89	52.21	1.17	1.09
13X-4, 94–96	115.84	32.75	24.67	1.98	1.95	2.84	2.76	1.49	1.47	47.58	46.84	0.91	0.88
13X-5, 28–30	116.68	25.88	20.56	2.08	2.02	2.84	2.70	1.66	1.61	41.80	40.53	0.72	0.68
13X-5, 94–96	117.34	35.72	26.32	1.98	1.94	2.96	2.84	1.46	1.43	50.80	49.71	1.03	0.99
13X-6, 28–30	118.18	32.57	24.57	1.99	1.94	2.88	2.73	1.50	1.46	47.79	46.46	0.92	0.87
13X-6, 94–96	118.84	35.79	26.36	1.96	1.90	2.90	2.74	1.44	1.40	50.33	48.89	1.01	0.96

Table 13 (continued).

Core, section, interval (cm)	Depth (mbsf)	WC-d (%)	WC-w (%)	WBD[a] (g/cm^3)	WBD[b] (g/cm^3)	GD[a] (g/cm^3)	GD[b] (g/cm^3)	DBD[a] (g/cm^3)	DBD[b] (g/cm^3)	Por[a] (%)	Por[b] (%)	VR[a]	VR[b]
14X-1, 48–50	120.48	39.08	28.10	1.91	1.86	2.87	2.74	1.37	1.34	52.24	51.11	1.09	1.05
14X-1, 128–130	121.28	38.16	27.62	1.93	1.87	2.92	2.72	1.40	1.35	52.09	50.36	1.09	1.01
14X-2, 49–51	121.99	34.83	25.83	1.98	1.89	2.93	2.67	1.47	1.40	49.92	47.60	1.00	0.91
14X-2, 120–122	122.70	36.16	26.56	1.94	1.89	2.85	2.72	1.42	1.39	50.16	48.99	1.01	0.96
14X-3, 49–51	123.49	38.42	27.75	1.93	1.86	2.93	2.71	1.40	1.34	52.35	50.40	1.10	1.02
14X-3, 108–110	124.08	39.96	28.55	1.89	1.83	2.85	2.68	1.35	1.31	52.61	51.08	1.11	1.04
14X-4, 49–51	124.99	40.82	28.98	1.89	1.81	2.88	2.63	1.34	1.28	53.45	51.15	1.15	1.05
14X-4, 121–123	125.71	37.45	27.25	1.93	1.86	2.89	2.67	1.41	1.35	51.34	49.35	1.06	0.97
14X-5, 17–19	126.17	35.62	26.27	1.93	2.19	2.83	3.66	1.43	1.61	49.54	56.01	0.98	1.27
15X-1, 64–66	130.34	39.05	28.08	1.93	1.86	2.96	2.73	1.39	1.34	52.96	50.97	1.13	1.04
15X-1, 122–124	130.92	21.81	17.91	2.14	2.10	2.81	2.73	1.76	1.73	37.40	36.74	0.60	0.58
15X-2, 64–66	131.84	35.01	25.93	1.97	1.90	2.92	2.71	1.46	1.41	49.92	48.07	1.00	0.93
15X-3, 37–39	133.07	19.38	16.23	2.04	2.14	2.52	2.71	1.71	1.79	32.27	33.88	0.48	0.51
15X-3, 64–66	133.34	37.76	27.41	1.93	1.88	2.89	2.75	1.40	1.37	51.55	50.31	1.06	1.01
16X-1, 64–66	139.84	36.62	26.81	1.97	1.89	2.98	2.73	1.44	1.38	51.59	49.37	1.07	0.97
16X-2, 64–66	141.34	34.20	25.48	1.98	1.93	2.91	2.78	1.48	1.44	49.25	48.10	0.97	0.93
16X-3, 64–66	142.84	43.60	30.36	1.91	1.80	3.07	2.69	1.33	1.26	56.60	53.39	1.30	1.15
16X-4, 64–66	144.34	35.20	26.03	2.00	1.94	3.01	2.83	1.48	1.44	50.81	49.29	1.03	0.97
17X-1, 65–67	149.35	42.46	29.81	1.89	1.83	2.96	2.73	1.33	1.28	55.08	53.11	1.23	1.13
17X-2, 65–67	150.85	40.99	29.07	1.91	1.84	2.96	2.73	1.35	1.31	54.18	52.22	1.18	1.09
17X-3, 65–67	152.35	41.02	29.09	1.87	1.83	2.84	2.70	1.33	1.30	53.17	51.96	1.14	1.08
17X-4, 65–67	153.85	38.63	27.86	1.93	1.86	2.92	2.73	1.39	1.34	52.37	50.67	1.10	1.03
17X-5, 65–67	155.35	41.55	29.35	1.92	1.84	3.03	2.76	1.36	1.30	55.09	52.82	1.23	1.12
17X-6, 65–67	156.85	34.69	25.76	1.97	1.90	2.89	2.70	1.46	1.41	49.41	47.76	0.98	0.91
17X-7, 17–19	157.87	36.52	26.75	1.84	1.90	2.60	2.75	1.35	1.39	48.08	49.49	0.93	0.98
18X-1, 65–67	158.85	43.79	30.45	1.86	1.80	2.88	2.68	1.29	1.25	55.14	53.37	1.23	1.14
18X-2, 64–66	160.34	40.84	29.00	1.90	1.85	2.92	2.76	1.35	1.31	53.80	52.38	1.16	1.10
18X-3, 65–67	161.85	32.15	24.33	2.01	1.95	2.91	2.73	1.52	1.47	47.70	46.17	0.91	0.86
18X-4, 64–66	163.34	33.47	25.07	2.01	1.93	2.97	2.75	1.51	1.45	49.26	47.28	0.97	0.90
18X-5, 66–68	164.86	30.25	23.22	2.06	1.97	2.97	2.74	1.58	1.52	46.67	44.72	0.88	0.81
18X-6, 66–68	166.36	36.63	26.81	1.95	1.88	2.93	2.72	1.43	1.38	51.12	49.30	1.05	0.97
18X-7, 19–21	167.39	42.29	29.72	1.91	1.82	2.99	2.71	1.34	1.28	55.26	52.75	1.24	1.12
19X-1, 99–101	168.79	39.61	28.37	1.90	1.85	2.86	2.72	1.36	1.33	52.53	51.25	1.11	1.05
19X-2, 99–101	170.29	33.59	25.15	1.99	1.93	2.91	2.74	1.49	1.44	48.83	47.33	0.95	0.90
19X-3, 99–101	171.79	33.54	25.12	1.97	1.93	2.85	2.73	1.47	1.44	48.26	47.19	0.93	0.89
19X-4, 99–101	173.29	33.48	25.08	1.96	1.92	2.81	2.71	1.47	1.44	47.86	46.95	0.92	0.88
19X-5, 99–101	174.79	31.68	24.06	1.98	1.93	2.82	2.69	1.51	1.47	46.55	45.36	0.87	0.83
20X-1, 53–55	177.93	34.09	25.42	1.93	1.94	2.77	2.78	1.44	1.44	47.98	48.00	0.92	0.92
20X-2, 77–79	179.67	32.92	24.77	2.00	1.96	2.92	2.79	1.51	1.47	48.36	47.25	0.94	0.90
20X-3, 73–75	181.13	35.30	26.09	2.02	1.96	3.09	2.88	1.50	1.45	51.52	49.79	1.06	0.99
20X-4, 78–80	182.68	38.73	27.92	1.91	1.91	2.87	2.88	1.38	1.38	52.01	52.08	1.08	1.09
20X-4, 116–118	183.06	29.50	22.78	2.11	1.99	3.06	2.75	1.63	1.53	46.81	44.13	0.88	0.79
20X-5, 76–78	184.16	34.67	25.75	2.04	1.92	3.10	2.76	1.51	1.43	51.17	48.32	1.05	0.93
20X-6, 76–78	185.66	50.82	33.70	1.85	1.77	3.12	2.82	1.23	1.18	60.75	58.26	1.55	1.40
21X-1, 114–116	188.24	63.18	38.72	1.72	1.69	3.00	2.86	1.05	1.04	64.89	63.84	1.85	1.77
21X-2, 127–129	189.87	80.95	44.74	1.64	1.57	3.19	2.75	0.91	0.87	71.61	68.43	2.52	2.17
21X-3, 119–121	191.29	67.63	40.34	1.70	1.64	3.08	2.77	1.02	0.98	67.04	64.65	2.03	1.83
21X-4, 134–136	192.94	55.89	35.85	1.76	1.61	2.93	2.36	1.13	1.03	61.51	56.22	1.60	1.28
21X-5, 33–35	193.43	66.42	39.91	1.70	1.65	3.02	2.77	1.02	0.99	66.16	64.21	1.95	1.79
21X-6, 33–35	194.93	69.40	40.97	1.69	1.63	3.08	2.77	1.00	0.96	67.56	65.25	2.08	1.88
22X-1, 120–122	197.90	42.96	30.05	1.91	1.61	3.02	2.14	1.33	1.13	55.85	47.32	1.27	0.90
22X-2, 133–135	199.53	60.54	37.71	1.75	1.67	3.04	2.70	1.09	1.04	64.24	61.45	1.80	1.59
22X-3, 134–136	201.04	48.65	32.73	1.85	1.76	3.03	2.70	1.24	1.18	58.98	56.16	1.44	1.28
22X-4, 121–123	202.41	47.50	32.20	1.88	1.75	3.13	2.63	1.28	1.19	59.16	54.97	1.45	1.22
22X-5, 123–125	203.93	40.71	28.93	1.94	1.85	3.05	2.75	1.38	1.32	54.77	52.24	1.21	1.09
23X-1, 88–90	207.18	41.28	29.22	1.90	1.86	2.95	2.80	1.35	1.31	54.27	52.95	1.19	1.13
23X-2, 95–97	208.75	55.55	35.71	1.76	1.71	2.91	2.73	1.13	1.10	61.21	59.71	1.58	1.48
23X-3, 93–95	210.23	70.42	41.32	1.64	1.60	2.83	2.66	0.96	0.94	66.00	64.59	1.94	1.82
23X-4, 92–94	211.72	65.34	39.52	1.70	1.65	2.98	2.73	1.03	1.00	65.50	63.54	1.90	1.74
23X-5, 91–93	213.21	98.29	49.57	1.81	1.47	7.17	2.59	0.91	0.74	87.30	71.30	6.87	2.48
23X-6, 91–93	214.71	40.52	28.84	1.62	1.86	2.13	2.78	1.16	1.32	45.69	52.32	0.84	1.10
24X-1, 41–43	216.41	42.83	29.99	1.88	1.83	2.92	2.76	1.31	1.28	54.93	53.59	1.22	1.15
24X-2, 41–43	217.91	40.59	28.87	1.93	1.84	2.99	2.72	1.37	1.31	54.23	51.90	1.18	1.08
24X-3, 70–72	219.70	65.06	39.42	1.69	1.66	2.93	2.78	1.02	1.01	65.05	63.80	1.86	1.76
24X-4, 114–116	221.64	63.07	38.68	1.73	1.67	3.07	2.77	1.06	1.02	65.39	62.99	1.89	1.70
24X-5, 112–114	223.12	56.15	35.96	1.79	1.73	3.08	2.83	1.15	1.11	62.80	60.82	1.69	1.55
24X-6, 24–26	223.74	52.66	34.49	1.79	1.75	2.95	2.78	1.17	1.14	60.26	58.82	1.52	1.43
24X-7, 21–23	225.21	70.33	41.29	1.65	1.60	2.88	2.64	0.97	0.94	66.39	64.43	1.98	1.81
25X-1, 42–44	226.02	70.03	41.19	1.66	1.62	2.94	2.71	0.98	0.95	66.75	64.92	2.01	1.85
25X-2, 41–43	227.51	55.03	35.50	1.77	1.72	2.94	2.76	1.14	1.11	61.21	59.68	1.58	1.48
25X-3, 8–10	228.68	45.98	31.50	1.84	1.78	2.90	2.70	1.26	1.22	56.56	54.76	1.30	1.21
25X-4, 8–10	230.18	63.12	38.69	1.70	1.65	2.90	2.68	1.04	1.01	64.13	62.28	1.79	1.65
25X-5, 13–15	231.73	61.80	38.20	1.71	1.65	2.89	2.66	1.05	1.02	63.56	61.61	1.74	1.60
25X-6, 15–17	233.25	60.18	37.57	1.72	1.66	2.89	2.65	1.07	1.04	62.88	60.89	1.69	1.56
26X-1, 52–54	235.72	53.31	34.77	1.79	1.74	2.97	2.77	1.17	1.13	60.68	59.00	1.54	1.44
26X-2, 17–19	236.87	50.65	33.62	1.78	1.73	2.83	2.66	1.18	1.15	58.32	56.79	1.40	1.31
26X-3, 61–63	238.81	61.92	38.24	1.68	1.63	2.78	2.58	1.04	1.01	62.64	60.94	1.68	1.56
26X-4, 38–40	240.08	40.21	28.68	1.90	1.57	2.89	2.01	1.35	1.12	53.09	44.06	1.13	0.79
26X-5, 82–84	242.02	37.37	27.20	1.97	1.89	2.99	2.77	1.43	1.38	52.19	50.23	1.09	1.01
26X-6, 98–100	243.68	35.86	26.39	1.93	1.87	2.84	2.65	1.42	1.37	49.80	48.08	0.99	0.93
27X-1, 37–39	245.27	37.27	27.15	1.99	1.90	3.05	2.79	1.45	1.39	52.61	50.38	1.11	1.02
27X-2, 27–29	246.67	48.57	32.69	1.82	1.78	2.91	2.75	1.22	1.19	57.96	56.61	1.38	1.30
27X-3, 23–25	248.13	44.31	30.70	1.87	1.79	2.94	2.69	1.29	1.24	55.93	53.72	1.27	1.16
27X-4, 21–23	249.61	47.01	31.98	1.86	1.78	3.00	2.73	1.26	1.21	57.95	55.62	1.38	1.25
27X-5, 23–25	251.13	56.86	36.25	1.73	1.69	2.82	2.67	1.10	1.08	61.02	59.71	1.57	1.48
28X-1, 24–26	254.84	44.36	30.73	1.87	1.82	2.96	2.77	1.30	1.26	56.12	54.53	1.28	1.20
28X-2, 40–42	256.50	38.43	27.76	1.96	1.86	3.03	2.72	1.42	1.35	53.16	50.51	1.14	1.02
28X-3, 42–44	258.02	40.71	28.93	1.91	1.83	2.95	2.70	1.36	1.30	53.99	51.76	1.17	1.07
28X-4, 113–115	260.23	58.72	37.00	1.77	1.68	3.10	2.70	1.12	1.06	63.98	60.77	1.78	1.55

Table 13 (continued).

Core, section, interval (cm)	Depth (mbsf)	WC-d (%)	WC-w (%)	WBD[a] (g/cm^3)	WBD[b] (g/cm^3)	GD[a] (g/cm^3)	GD[b] (g/cm^3)	DBD[a] (g/cm^3)	DBD[b] (g/cm^3)	Por[a] (%)	Por[b] (%)	VR[a]	VR[b]
28X-5, 58–60	261.18	60.50	37.69	1.77	1.67	3.16	2.69	1.10	1.04	65.08	61.36	1.86	1.59
28X-6, 51–53	262.61	52.61	34.47	1.79	1.73	2.96	2.70	1.17	1.13	60.31	58.05	1.52	1.38
29X-1, 73–75	264.93	40.42	28.79	1.92	1.85	2.96	2.75	1.37	1.32	53.85	52.05	1.17	1.09
29X-2, 84–86	266.54	39.17	28.14	1.95	1.82	3.02	2.62	1.40	1.31	53.58	50.07	1.15	1.00
29X-3, 40–42	267.60	33.59	25.14	2.03	1.91	3.02	2.68	1.52	1.43	49.74	46.80	0.99	0.88
29X-4, 91–93	269.61	46.55	31.76	1.86	1.77	2.98	2.68	1.27	1.21	57.51	54.88	1.35	1.22
29X-5, 94–96	271.14	61.90	38.23	1.73	1.65	3.03	2.66	1.07	1.02	64.69	61.66	1.83	1.61
29X-6, 99–101	272.69	51.40	33.95	1.85	1.74	3.17	2.71	1.22	1.15	61.35	57.65	1.59	1.36
30X-1, 82–84	274.72	72.98	42.19	1.66	1.60	3.03	2.70	0.96	0.92	68.35	65.74	2.16	1.92
30X-2, 92–94	276.32	63.58	38.87	1.71	1.66	3.00	2.73	1.05	1.01	65.01	62.83	1.86	1.69
30X-3, 104–106	277.94	76.74	43.42	1.63	1.56	2.97	2.60	0.92	0.88	68.99	66.05	2.23	1.95
30X-4, 27–29	278.67	82.75	45.28	1.64	1.55	3.27	2.66	0.90	0.85	72.53	68.27	2.64	2.15
30X-5, 86–88	280.76	43.95	30.53	1.90	1.81	3.03	2.74	1.32	1.26	56.50	54.02	1.30	1.17
30X-6, 50–52	281.90	38.83	27.97	1.92	1.86	2.91	2.73	1.38	1.34	52.46	50.88	1.10	1.04
30X-7, 38–40	283.28	38.20	27.64	1.95	1.87	2.98	2.74	1.41	1.35	52.59	50.50	1.11	1.02
31X-1, 42–44	283.92	35.91	26.42	1.97	1.88	2.93	2.68	1.45	1.38	50.69	48.45	1.03	0.94
31X-2, 134–136	286.34	37.05	27.03	1.99	1.88	3.04	2.72	1.45	1.37	52.38	49.61	1.10	0.98
31X-3, 134–136	287.84	36.06	26.50	1.98	1.90	2.99	2.74	1.46	1.39	51.26	49.05	1.05	0.96
31X-4, 96–98	288.96	35.11	25.98	2.03	1.91	3.08	2.75	1.50	1.42	51.34	48.53	1.05	0.94
31X-5, 114–116	290.64	24.08	19.41	1.92	2.04	2.44	2.68	1.55	1.65	36.43	38.67	0.57	0.63
31X-6, 97–99	291.97	58.22	36.80	1.86	1.68	3.53	2.68	1.17	1.06	66.73	60.39	2.01	1.52
31X-7, 23–25	292.73	64.16	39.08	1.69	1.64	2.91	2.65	1.03	1.00	64.58	62.40	1.82	1.66
32X-1, 37–39	293.57	63.16	38.71	1.74	1.68	3.13	2.80	1.07	1.03	65.83	63.28	1.93	1.72
32X-2, 51–53	295.21	72.22	41.93	1.64	1.60	2.91	2.70	0.95	0.93	67.21	65.58	2.05	1.91
32X-3, 62–64	296.82	67.49	40.29	1.69	1.63	2.99	2.69	1.01	0.97	66.29	63.93	1.97	1.77
32X-4, 80–82	298.50	65.73	39.66	1.70	1.64	3.02	2.71	1.03	0.99	65.95	63.47	1.94	1.74
32X-5, 86–88	300.06	65.21	39.47	1.72	1.65	3.06	2.74	1.04	1.00	66.08	63.53	1.95	1.74
32X-6, 116–118	301.86	41.70	29.43	1.89	1.87	2.92	2.84	1.34	1.32	54.31	53.61	1.19	1.16
32X-7, 20–22	302.40	66.48	39.93	1.67	1.64	2.86	2.71	1.00	0.98	64.96	63.73	1.85	1.76
33X-1, 92–94	303.72	40.21	28.68	1.75	1.95	2.44	3.07	1.25	1.39	48.91	54.65	0.96	1.20
33X-2, 118–120	305.48	56.85	36.24	1.62	1.77	2.43	3.00	1.04	1.13	57.42	62.48	1.35	1.67
33X-3, 135–137	307.15	61.75	38.18	1.64	1.76	2.59	3.14	1.01	1.09	60.98	65.44	1.56	1.89
33X-4, 71–73	308.01	79.97	44.44	1.66	1.55	3.28	2.63	0.92	0.86	71.93	67.21	2.56	2.05
33X-5, 95–97	309.75	99.77	49.94	1.63	1.44	3.96	2.44	0.82	0.72	79.42	70.33	3.86	2.37
33X-6, 97–99	311.27	94.07	48.47	1.64	1.40	3.76	2.14	0.84	0.72	77.51	66.22	3.45	1.96
34X-1, 77–79	313.27	42.21	29.68	1.94	1.82	3.11	2.71	1.36	1.28	56.16	52.72	1.28	1.12
34X-2, 52–54	314.52	59.42	37.27	1.73	1.68	2.93	2.70	1.09	1.05	62.98	61.04	1.70	1.57
34X-3, 56–58	316.06	66.28	39.86	1.66	1.45	2.83	2.00	1.00	0.87	64.65	56.38	1.83	1.29
34X-4, 53–55	317.53	47.52	32.21	1.83	1.80	2.93	2.82	1.24	1.22	57.57	56.69	1.36	1.31
34X-5, 51–53	319.01	44.73	30.90	1.85	2.02	2.90	3.59	1.28	1.40	55.83	61.05	1.26	1.57
35X-1, 122–124	321.42	45.72	31.38	1.83	1.81	2.85	2.77	1.26	1.24	55.99	55.27	1.27	1.24
35X-2, 29–31	321.99	34.40	25.60	1.69	1.93	2.16	2.78	1.25	1.44	42.08	48.31	0.73	0.93
35X-3, 133–135	324.53	47.09	32.01	1.82	1.80	2.87	2.80	1.24	1.22	56.83	56.27	1.32	1.29
35X-4, 133–135	326.03	42.84	29.99	1.86	1.83	2.86	2.74	1.30	1.28	54.44	53.41	1.19	1.15
35X-5, 136–138	327.56	45.46	31.25	1.84	1.80	2.87	2.75	1.26	1.24	55.98	54.99	1.27	1.22
35X-6, 29–31	327.99	43.15	30.14	1.84	1.82	2.81	2.74	1.29	1.27	54.19	53.59	1.18	1.15
36X-1, 54–56	330.64	33.68	25.19	1.99	1.93	2.91	2.75	1.49	1.44	48.89	47.48	0.96	0.90
36X-2, 68–70	332.28	32.81	24.70	2.01	1.96	2.93	2.79	1.51	1.47	48.36	47.17	0.94	0.89
36X-3, 35–37	333.45	36.18	26.57	1.92	1.88	2.82	2.69	1.41	1.38	49.86	48.72	0.99	0.95
36X-4, 66–68	335.26	33.40	25.04	2.00	1.93	2.94	2.75	1.50	1.45	48.95	47.24	0.96	0.90
36X-5, 9–11	336.19	35.78	26.35	1.98	1.91	2.98	2.78	1.46	1.41	50.98	49.22	1.04	0.97
37X-1, 75–77	340.75	34.59	25.70	1.96	1.93	2.87	2.79	1.46	1.44	49.22	48.51	0.97	0.94
37X-2, 75–77	342.25	30.85	23.58	2.05	2.01	2.95	2.86	1.56	1.54	47.05	46.28	0.89	0.86
151-908B-													
1H-1, 55–57	0.55	41.44	29.30	1.87	1.87	2.83	2.83	1.32	1.32	53.33	53.32	1.143	1.142
1H-1, 106–108	1.06	44.53	30.81	1.85	1.83	2.89	2.81	1.28	1.26	55.65	54.94	1.255	1.219
1H-2, 26–28	1.76	31.24	23.81	1.94	1.93	2.68	2.67	1.48	1.47	44.98	44.90	0.817	0.815
1H-2, 106–108	2.56	63.44	38.81	1.66	1.70	2.75	2.91	1.02	1.04	62.97	64.28	1.701	1.799
1H-3, 6–8	3.06	40.69	28.92	1.88	1.86	2.85	2.78	1.34	1.32	53.08	52.47	1.131	1.104
2H-1, 64–66	4.14	27.18	21.37	2.03	2.01	2.78	2.73	1.60	1.58	42.43	41.98	0.737	0.723
2H-1, 102–104	4.52	35.93	26.43	1.94	1.92	2.85	2.79	1.43	1.41	49.96	49.40	0.999	0.976
2H-2, 30–32	5.30	38.55	27.82	1.90	1.87	2.83	2.73	1.37	1.35	51.59	50.65	1.066	1.026
2H-2, 64–66	5.64	36.42	26.70	1.94	1.91	2.89	2.77	1.43	1.40	50.64	49.62	1.026	0.985
3H-1, 62–64	13.62	45.00	31.04	1.85	1.82	2.89	2.81	1.27	1.26	55.92	55.22	1.269	1.233
3H-2, 68–70	15.18	29.32	22.67	2.01	1.98	2.79	2.73	1.55	1.53	44.42	43.87	0.799	0.781
3H-3, 65–67	16.65	38.97	28.04	1.88	1.88	2.80	2.79	1.36	1.35	51.54	51.44	1.063	1.059
3H-4, 63–65	18.13	27.60	21.63	2.04	1.99	2.80	2.68	1.60	1.56	42.97	41.93	0.754	0.722
3H-5, 57–59	19.57	28.32	22.07	1.96	2.00	2.64	2.74	1.53	1.56	42.15	43.05	0.729	0.756
3H-6, 25–27	20.65	26.72	21.08	2.07	2.04	2.84	2.78	1.63	1.61	42.51	42.03	0.740	0.725
3H-7, 33–35	22.23	31.41	23.90	1.94	1.98	2.70	2.80	1.48	1.51	45.23	46.19	0.826	0.858
4H-1, 91–93	23.41	35.35	26.12	1.91	1.90	2.75	2.72	1.41	1.40	48.64	48.44	0.947	0.939
4H-2, 54–56	24.54	29.05	22.51	2.01	1.45	2.79	1.65	1.56	1.13	44.13	31.90	0.790	0.468
4H-3, 123–125	26.73	34.12	25.44	1.94	1.91	2.79	2.72	1.45	1.43	48.16	47.52	0.929	0.905
4H-4, 81–83	27.81	24.54	19.70	2.06	2.04	2.75	2.69	1.66	1.64	39.65	39.16	0.657	0.644
4H-5, 81–83	29.31	37.27	27.15	1.70	1.86	2.25	2.68	1.24	1.36	45.05	49.34	0.820	0.974
4H-6, 81–83	30.81	38.29	27.69	1.90	1.51	2.82	1.84	1.37	1.09	51.32	40.78	1.054	0.689
4H-7, 26–28	31.76	42.98	30.06	1.85	1.81	2.83	2.71	1.29	1.27	54.24	53.19	1.185	1.137
5H-1, 99–101	32.99	38.56	27.83	1.71	1.86	2.30	2.70	1.23	1.34	46.39	50.40	0.865	1.016
5H-2, 99–101	34.49	36.63	26.81	1.71	1.88	2.27	2.71	1.25	1.38	44.77	49.16	0.811	0.967
5H-3, 99–101	35.99	35.61	26.26	1.92	1.88	2.79	2.68	1.42	1.39	49.22	48.26	0.969	0.933
5H-4, 99–101	37.49	24.87	19.92	1.93	2.14	2.47	2.95	1.55	1.72	37.51	41.68	0.600	0.715
5H-5, 99–101	38.99	26.81	21.14	1.88	2.47	2.43	3.96	1.49	1.94	38.87	50.86	0.636	1.035
5H-6, 99–101	40.49	37.16	27.09	1.89	1.87	2.76	2.69	1.38	1.36	49.99	49.41	1.000	0.977
5H-7, 48–50	41.48	32.65	24.62	1.93	1.92	2.72	2.69	1.46	1.45	46.47	46.13	0.868	0.856
6H-1, 32–34	41.82	23.64	19.12	2.06	2.05	2.71	2.68	1.67	1.65	38.45	38.16	0.625	0.617
6H-1, 99–101	42.49	29.78	22.95	1.81	1.97	2.35	2.71	1.40	1.52	40.60	44.05	0.683	0.787
6H-2, 31–33	43.31	32.85	24.73	1.57	1.95	1.90	2.76	1.18	1.46	37.87	46.93	0.610	0.884
6H-2, 99–101	43.99	24.12	19.43	2.08	2.05	2.77	2.71	1.68	1.65	39.48	38.91	0.652	0.637

Table 13 (continued).

Core, section, interval (cm)	Depth (mbsf)	WC-d (%)	WC-w (%)	WBD[a] (g/cm³)	WBD[b] (g/cm³)	GD[a] (g/cm³)	GD[b] (g/cm³)	DBD[a] (g/cm³)	DBD[b] (g/cm³)	Por[a] (%)	Por[b] (%)	VR[a]	VR[b]
6H-3, 99–101	45.49	36.73	26.86	2.17	1.89	3.67	2.72	1.58	1.38	56.78	49.40	1.314	0.976
6H-4, 98–100	46.98	23.61	19.10	2.10	2.05	2.79	2.67	1.70	1.65	39.14	38.11	0.643	0.616
6H-5, 88–90	48.38	34.71	25.77	1.96	1.92	2.88	2.76	1.46	1.43	49.38	48.30	0.975	0.934
6H-5, 99–101	48.49	32.84	24.72	1.92	1.94	2.70	2.75	1.45	1.46	46.35	46.87	0.864	0.882
6H-6, 90–92	49.90	28.97	22.46	2.02	1.98	2.80	2.71	1.56	1.54	44.17	43.39	0.791	0.767
6H-6, 99–101	49.99	30.19	23.19	1.74	1.25	2.20	1.34	1.34	0.96	39.36	28.29	0.649	0.395
6H-7, 40–42	50.90	34.77	25.80	1.95	1.90	2.83	2.69	1.44	1.41	48.98	47.71	0.960	0.912
7H-1, 99–101	51.99	36.71	26.85	1.71	1.66	2.26	2.15	1.25	1.22	44.79	43.55	0.811	0.771
7H-2, 99–101	53.49	28.97	22.46	2.02	1.98	2.81	2.72	1.56	1.54	44.24	43.46	0.793	0.769
7H-3, 99–101	54.99	28.91	22.43	2.02	1.99	2.82	2.74	1.57	1.54	44.29	43.58	0.795	0.772
7H-4, 99–101	56.49	26.27	20.80	2.06	2.02	2.79	2.71	1.63	1.60	41.73	41.01	0.716	0.695
7H-5, 76–78	57.76	23.96	19.33	2.11	2.06	2.82	2.72	1.70	1.66	39.71	38.91	0.659	0.637
7H-5, 99–101	57.99	33.46	25.07	1.97	1.92	2.86	2.72	1.48	1.44	48.29	47.06	0.934	0.889
7H-6, 99–101	59.49	33.02	24.82	1.81	2.04	2.43	3.04	1.36	1.53	43.86	49.44	0.781	0.978
7H-7, 36–38	60.36	32.22	24.37	1.99	1.96	2.85	2.77	1.50	1.48	47.25	46.51	0.896	0.870
8H-1, 49–51	60.99	28.18	21.98	2.10	2.05	2.97	2.85	1.64	1.60	44.98	43.89	0.817	0.782
8H-1, 99–101	61.49	28.95	22.45	2.03	1.97	2.84	2.69	1.58	1.53	44.54	43.14	0.803	0.759
8H-2, 99–101	62.99	32.82	24.71	1.97	1.93	2.83	2.73	1.49	1.46	47.56	46.63	0.907	0.874
8H-3, 99–101	64.49	35.91	26.42	1.96	1.90	2.92	2.75	1.44	1.40	50.55	49.04	1.022	0.962
8H-4, 99–101	65.99	22.27	18.21	2.16	2.12	2.86	2.78	1.76	1.73	38.33	37.67	0.622	0.604
8H-5, 99–101	67.49	37.40	27.22	1.92	1.90	2.84	2.79	1.39	1.38	50.87	50.42	1.035	1.017
8H-5, 130–132	67.80	36.40	26.69	1.94	1.90	2.87	2.76	1.42	1.39	50.51	49.47	1.021	0.979
8H-6, 99–101	68.99	47.96	32.41	1.82	1.59	2.89	2.17	1.23	1.08	57.48	50.35	1.352	1.014
9H-1, 25–27	70.25	34.69	25.75	1.96	1.91	2.86	2.74	1.45	1.42	49.15	48.08	0.967	0.926
9H-1, 109–111	71.09	35.24	26.06	1.95	1.91	2.86	2.75	1.44	1.41	49.54	48.56	0.982	0.944
9H-2, 35–37	71.85	23.37	18.94	2.20	2.12	3.00	2.83	1.78	1.72	40.58	39.22	0.683	0.645
9H-2, 109–111	72.59	38.24	27.66	1.92	1.88	2.87	2.76	1.39	1.36	51.75	50.76	1.073	1.031
9H-3, 33–35	73.33	34.32	25.55	1.96	1.54	2.86	1.87	1.46	1.15	48.91	38.48	0.957	0.625
9H-3, 109–111	74.09	32.47	24.51	1.96	1.95	2.79	2.75	1.48	1.47	46.90	46.57	0.883	0.871
9H-4, 53–55	75.03	33.13	24.88	1.99	1.94	2.88	2.74	1.49	1.45	48.22	46.99	0.931	0.886
10H-1, 99–101	76.39	34.33	25.56	1.97	1.93	2.88	2.76	1.47	1.43	49.11	48.00	0.965	0.923
10H-2, 99–101	77.89	35.61	26.26	1.95	1.90	2.89	2.73	1.44	1.40	50.06	48.68	1.002	0.948
10H-3, 99–101	79.39	33.56	25.13	1.96	1.93	2.82	2.73	1.47	1.44	48.03	47.23	0.924	0.895
10H-4, 101–103	80.91	46.62	31.79	1.84	1.80	2.93	2.78	1.26	1.23	57.15	55.81	1.334	1.263
10H-5, 101–103	82.41	23.41	18.97	2.10	2.07	2.77	2.71	1.70	1.68	38.78	38.26	0.634	0.620

Notes: WC-d = water content (% dry sample weight); WC-w = water content (% wet sample weight); WBD = wet-bulk density; GD = grain density; DBD = dry-bulk density; Por = porosity; VR = void ratio.

[a]Value calculated using Method B.

[b]Value calculated using Method C.

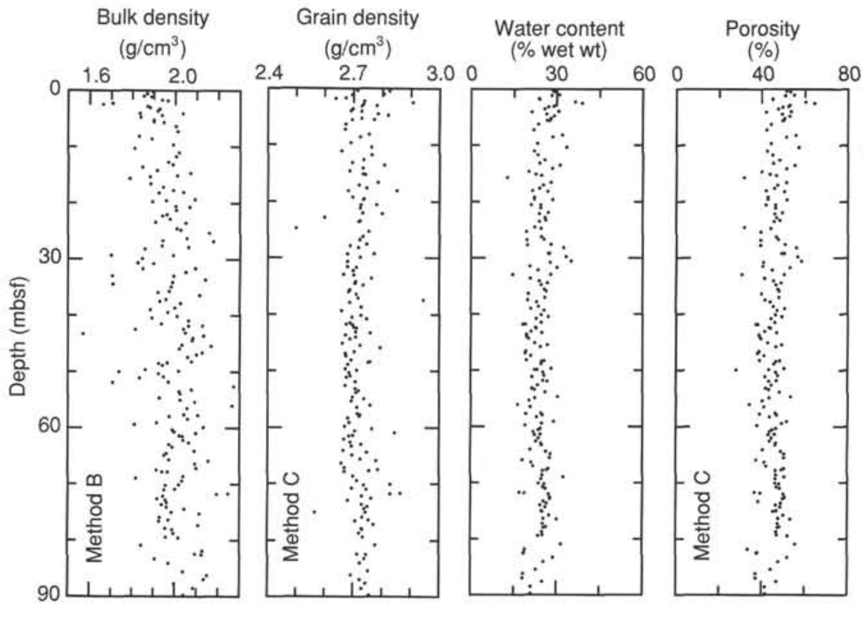

Figure 32. Comparison of index properties vs. depth in Holes 908A and 908B.

due to orbital forcing of climate; further work needs to be done when a better-constrained age model has been constructed.

Sedimentary Unit II below the unconformity is marked by the appearance of a significant siliceous microfossil component in the sediments. Typically, such opal-rich sediments have lower bulk densities and lower resistivities than other pelagic sequences. Opal, with a grain density of about 2.2 g/cm³, is less dense than carbonates (2.7 g/cm³), clays (2.3–2.7 g/cm³), or quartz (2.65 g/cm³). In addition, the open structure of the siliceous skeletons helps to retain water in the buried sediment, leading to higher porosity and, hence, lower resistivities. This is reflected in the logs from this hole, which exhibit a marked decrease in bulk density and resistivity and an increase in

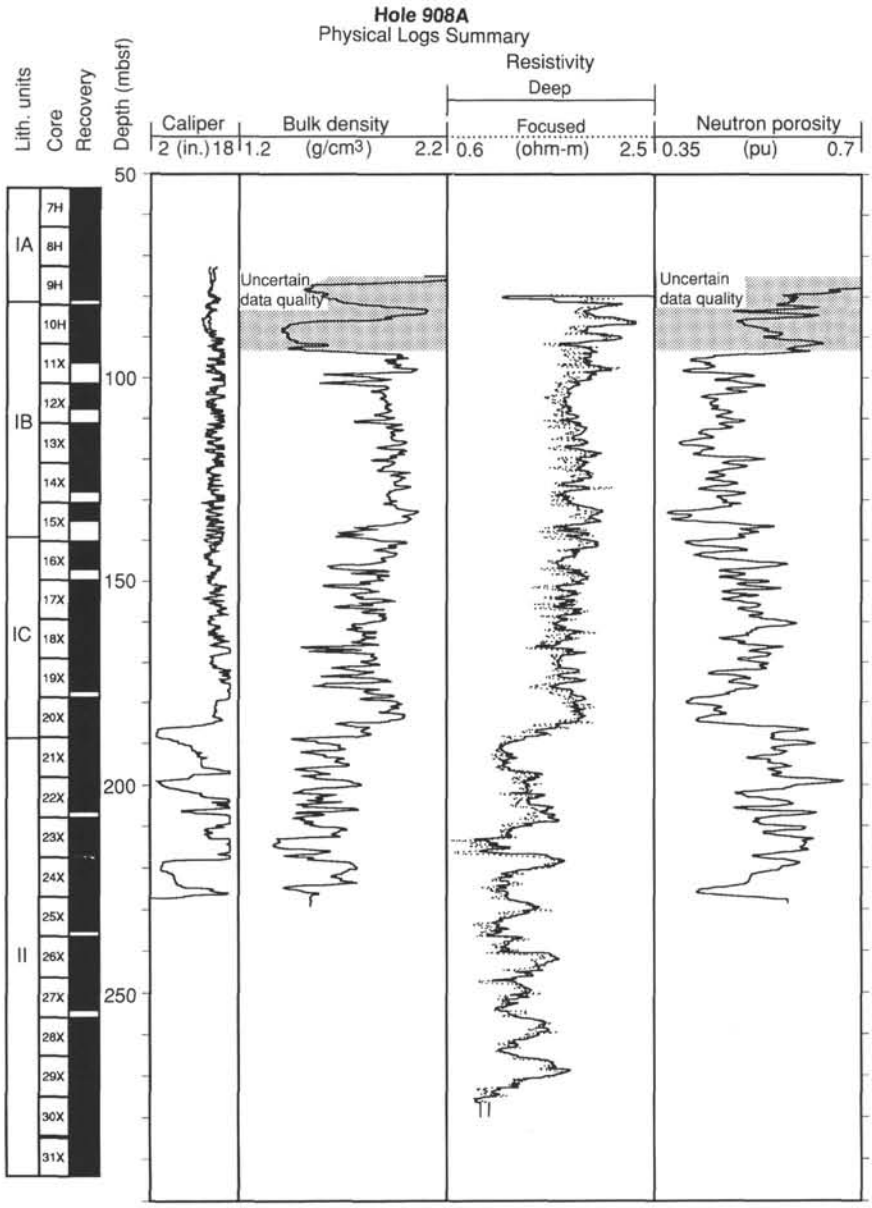

Figure 33. Orthogonal caliper data from the Formation MicroScanner (FMS) shown with: bulk density data from the high-temperature lithodensity tool (HLDT); deep phasor induction and spherically focused resistivity from the phasor dual induction tool (DIT); neutron porosity data from the compensated neutron porosity tool (CNT). The data are unsmoothed apart from the neutron porosity data, which have undergone a linear 10-point (1.52 m) moving average filter.

neutron porosity upon the downward transition to Unit II. The natural gamma-ray activity (Fig. 35) also decreases in Unit II, representing the diluting effect of the opaline component upon the clays.

The log data in Unit II exhibit more variability than in the upper Unit I, with a high-amplitude cyclic signal in the resistivity log, of 10–15 m wavelength. This may be a reflection of varying clay and opaline components, although core-based studies are not yet sufficiently detailed to confirm this. The same frequency cyclicity is seen in the porosity data from discrete measurements on core (see "Physical Properties" section, this chapter; Fig. 37). The variable nature of this unit also is exhibited by the highly rugose nature of the borehole in this section (Fig. 33).

Formation MicroScanner

The orthogonal calipers from the FMS (Fig. 33) show the fairly large and rugose nature of the borehole throughout the logged section. In zones with a large borehole diameter the contact of the FMS pads with the borehole wall was unreliable, resulting in poor quality images in small sections of the borehole. Because of operational difficulties, the FMS was unable to log below the unconformity at the base of Unit I. The raw images recorded in Unit I, however, are of good quality and exhibit a high-frequency banding of resistive beds interlayered with more conductive beds. An example of this is shown in Figure 36.

Porosity Estimates from Resistivity

We calculated porosity using the deep phasor induction resistivity log (IDPH) from the dual induction tool with set values of $a = 1$ and $m = 2.25$ for the Archie (1942) equation (see "Explanatory Notes" chapter, this volume). R_w is calculated based on its known relationships to temperature and salinity (Keller, 1982), temperature was taken from the Lamont-Doherty temperature logging tool, and interstitial salinities from core measurements (see "Inorganic Geochemistry" section, this chapter).

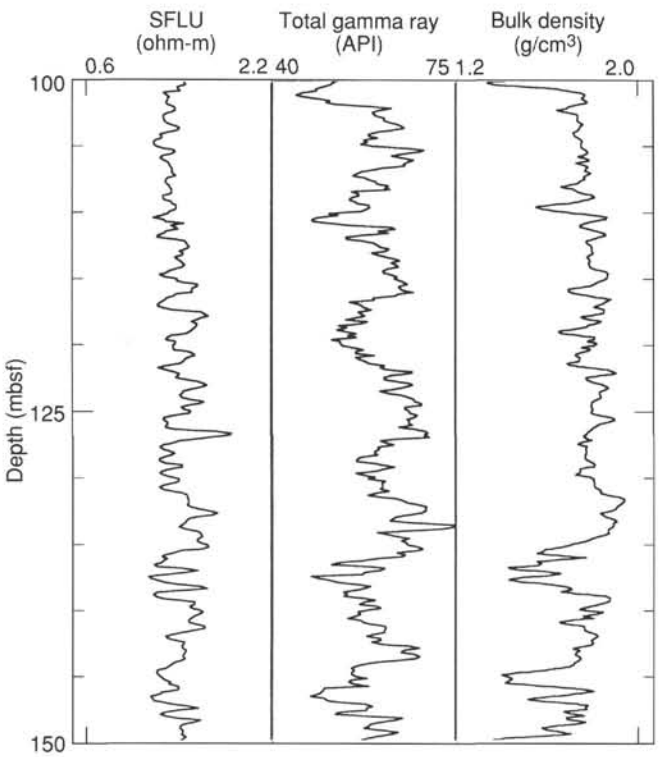

Figure 34. Comparison of the spherically focused resistivity, total gamma-ray, and high-resolution bulk density logs over the interval 100–150 mbsf in Hole 908A.

The calculated porosities have an excellent correlation with those determined from discrete core samples (Fig. 37).

SEISMIC STRATIGRAPHY

Introduction

A synthetic seismogram was generated from the velocity and density profiles at Site 908 to correlate reflectors in the seismic section to stratigraphic changes. The acoustic impedance profile (the product of density and velocity) and the profile of reflection coefficients (the rate of change of acoustic impedance) were determined both as a function of depth and of two-way acoustic traveltime (TWT). Convolution of the reflection coefficient profile with an assumed source acoustic wavelet resulted in a synthetic seismogram to compare with the measured seismic section.

The seismic section used for correlation is the line UB-24-81, collected by the University of Bergen, Norway.

Acoustic Wavelet

We did not have a record of the acoustic wavelet from the UB-24-81 line and, therefore, created a wavelet based upon the strong doublet exhibited at the seafloor. The wavelet used has a 25-ms period with an e-folding attenuation of 14 ms.

Reflection Coefficients

Discrete measurements of density and compressional velocity on the recovered cores (see "Physical Properties" section, this chapter) were combined with logging data (see "Downhole Measurements" section, this chapter) to form a profile of reflection coefficients for Hole 908A. The logs provided detailed velocity data on the interval between 85 and 259 mbsf. Discrete velocity data measured on core were used above and below this interval. The discrete velocity data below a depth of 70 mbsf were shifted by adding 120 m/s to the measured values to match the logs. With this shift, the two data sets correlate well (Fig. 30).

Density measurements from the logs were first edited to remove questionable data and then combined with discrete measurements on the core. The density log was edited by comparison with the resistivity logs from the hole. As low density should indicate high porosity in the sediments, low density should also correlate with low resistivity measurements. Where the two measurements did not correlate, density data were deleted. Because the lower part of the hole had large amounts of questionable data, we used discrete shipboard measurements below 187 mbsf. Discrete shipboard measurements were also used for the interval between 0 and 95 mbsf.

The resulting data were interpolated to a 1-m sample spacing and then used to generate acoustic impedance and reflection coefficient profiles for Site 908 (Fig. 38). Also shown on the figure are the lithostratigraphic units (see "Lithostratigraphy" section, this chapter). The unit boundaries are marked by impedance contrasts that give rise to relatively strong seismic reflectors. It is important to note that the unconformity between the Pliocene sediment packet and the Oligocene sediments (Unit I/II boundary) has a strong negative reflection coef-

Table 14. Summary of logging operations at Hole 908A.

14 Aug. 1993	
01:30	Last core on deck; prepare hole for logging. Pipe set at 79.3 mbsf.
09:15	Rig up NGT-DSI-DIT (+TLT).
10:00	RIH with NGT-DSI-DIT.
10:57	Start downgoing log from 120.5 mbsf to 179.5 (where tool temporarily unable to pass obstruction).
11:15	Continue RIH to 277.5 mbsf (where tool failed to pass obstruction).
11:37	Main upgoing log from 277.5 mbsf to mud line at 600 ft/hour.
13:10	Repeat upgoing log from 220.5-151.5 mbsf. POOH.
14:40	Rig up NGT-CNT-HLDT (+TLT).
15:15	RIH with NGT-CNT-HLDT. Stopped by bridge at 229.5 mbsf.
16:00	Main upgoing log from 229 mbsf to EOP (at 79 mbsf). POOH - problem getting tool back into pipe. On retrieving tool, cable seen to be crimped at torpedo joint; re-head cable.
17:20	Ream down hole to TD to clear bridges (apparent from HLDT caliper).
23:30	Rig up NGT-FMS.
15 Aug. 1993	
00:00	RIH with NGT-FMS. Unable to pass bridge at 177.5 mbsf.
00:45	Main upgoing log from 177 mbsf to EOP (pulled to 59 mbsf).
01:18	Repeat upgoing log from 174.5 to EOP (pulled to 59 mbsf).
01:35	Problem getting tool back into EOP. Pump to open flapper.
01:55	Tool reentered pipe; POOH.
02:15	Rig down. End of logging operations.

Notes: Times given in Universal Time Coordinated (UTC). Drillers TD (total depth) = 344.6 mbsf; WD (water depth) = 1284.5 mbrf; EOP (end of pipe) = 79 mbsf; RIH = run in hole; POOH = pull out of hole. For further explanations, see "Explanatory Notes" chapter, this volume.

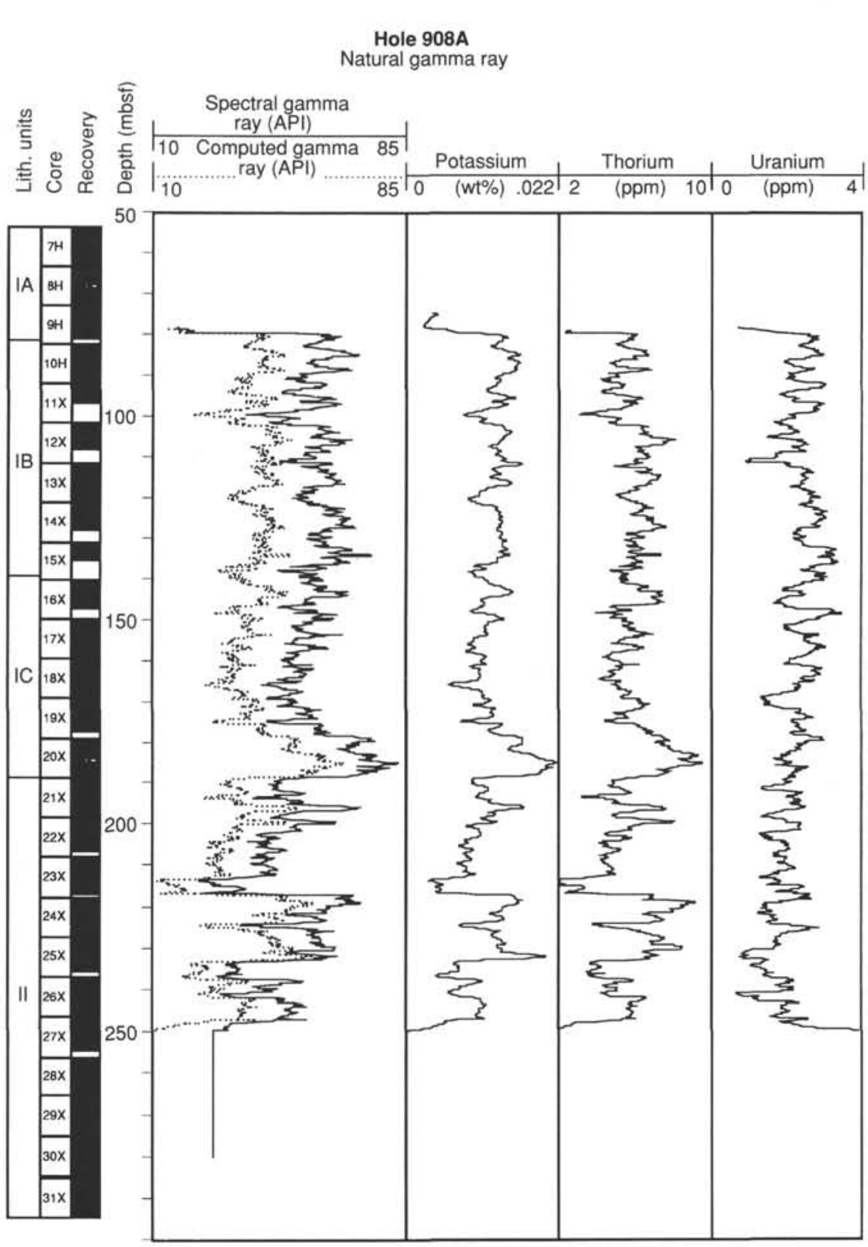

Figure 35. Data from the natural gamma-ray spectrometry tool (NGT) recorded on the seismic stratigraphy tool string.

ficient. The unconformity should appear on a seismic profile as a negative reflector.

The Synthetic Seismogram

Figure 39 shows the synthetic seismogram resulting from the convolution of the seismic wavelet with the reflection coefficient profile, whereas Figure 40 compares the synthetic seismogram with the recorded seismic section around Site 908. Also shown in Figure 39 are the lithologic unit boundaries translated from depth into equivalent TWT.

The synthetic seismogram has reflectors that include all the lithostratigraphic unit boundaries noted by the shipboard sedimentologists. The top of reflector C marks the Subunit IA/IB lithologic boundary. Lithologic Unit IA is characterized by the presence of greater than 10% sand; Unit IB is a mixed unit of silty clays and clayey silts. The Subunit IB/IC transition is at the base of reflector E and represents a strong negative contrast in acoustic impedance. At this boundary the sediments change to relatively homogeneous silty clays. The Unit I/II unconformity is marked by the base of reflector H, and the unconformity generates the negative reflector between H and I. The Oligocene sediments of lithologic Unit II are characterized by the high-amplitude reflectors I through P.

One of the reflectors in the upper sediment column (reflector D) may have been generated by free gas within the sediments. Methane concentrations in headspace gases in Hole 908A increased by two orders of magnitude at 100 mbsf (see "Organic Geochemistry" section, this chapter). Similarly, a strong negative change in acoustic impedance characterizes this level (Fig. 38). The negative reflection coefficient at 100 mbsf interacts with the seismic wavelet to produce a reflector displaced 10–15 ms deeper in the section.

The reflectors in the synthetic seismogram match those in the seismic record reasonably well (Fig. 40). The unconformity between

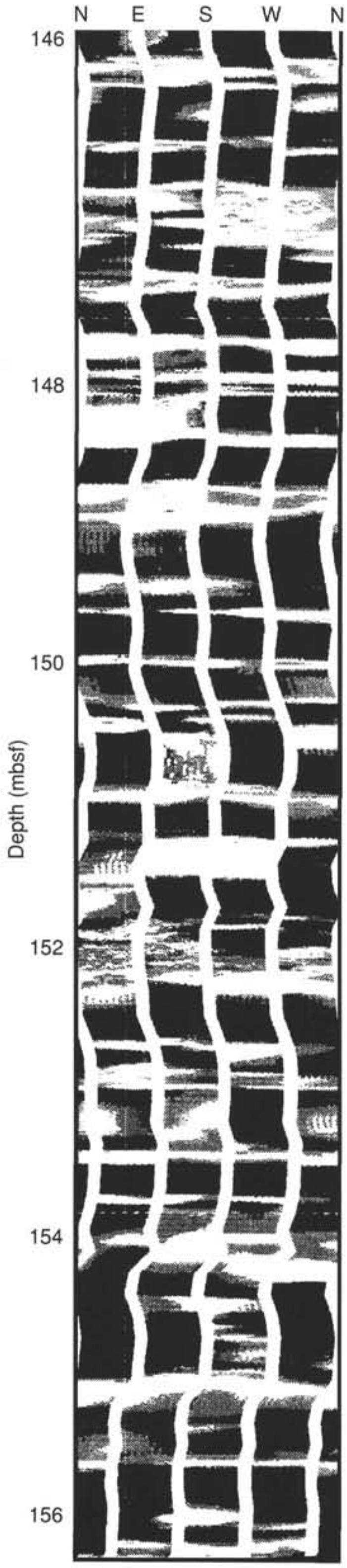

Figure 36. Section of microresistivity images from the FMS in Hole 908A. The images show the banded nature of the sediments in the lower part of Unit IC (148–156 mbsf). The lighter areas indicate resistive sediments, and the darker layers more conductive beds.

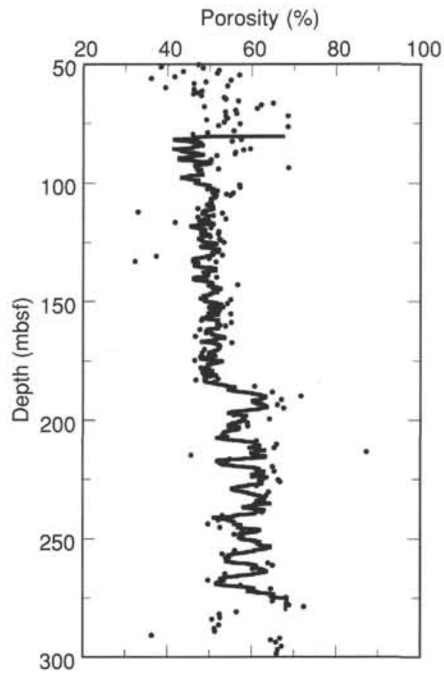

Figure 37. Porosity values derived from the deep phasor induction of the dual induction tool compared with porosity measurements on discrete core samples. The input resistivity data and the final porosity log are unsmoothed.

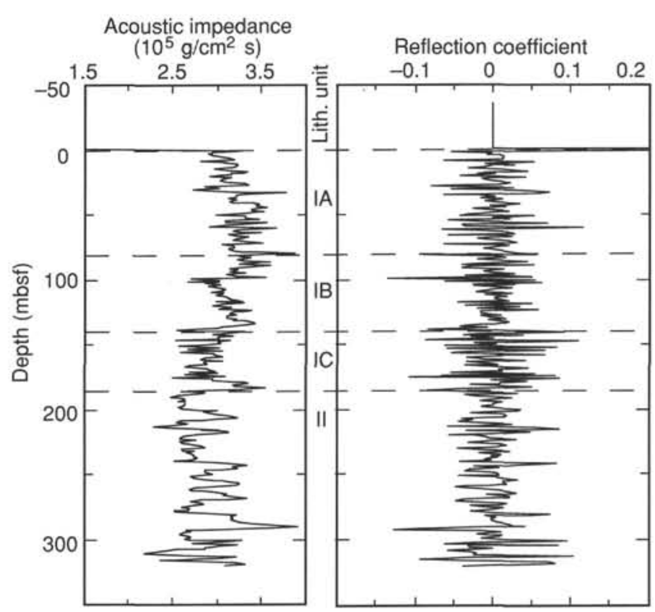

Figure 38. Acoustic impedance and reflection coefficient profiles at Site 908. Also shown are the lithostratigraphic unit boundaries from the "Lithostratigraphy" section (this chapter).

reflectors H and J is at the proper depth, and for the most part the other reflectors match those in the seismic section. Mismatches can be found between the seismic section and reflectors F and G within lithologic Unit IC and reflector K in Unit II, below the unconformity. However, Unit IC appears to be of variable thickness in the seismic record. The mismatch may represent some minor difference between the drill site and the location of the seismic profile. Similarly, the dipping beds of Unit II cause variable interference effects with the acoustic signal. Minor displacements between the drill site and the profile could produce the offsets we observe.

Ms 151IR-106

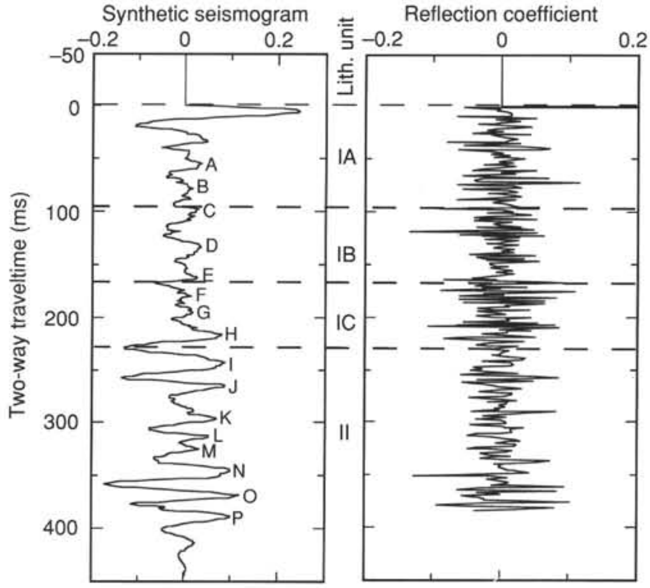

Figure 39. Reflection coefficient and synthetic seismogram shown against two-way traveltime. Locations of lithostratigraphic unit boundaries have been interpolated onto the figure, and seismic reflectors are identified.

NOTE: For all sites drilled, core-description forms ("barrel sheets") and core photographs can be found in Section 6, beginning on page 465. Forms containing smear-slide data can be found in Section 7, beginning on page 849. Thin-section descriptions are given in Section 8, beginning on page 885, and sediment thin sections in Section 9, beginning on page 895. Dropstone descriptions are included in Section 10, beginning on page 903.

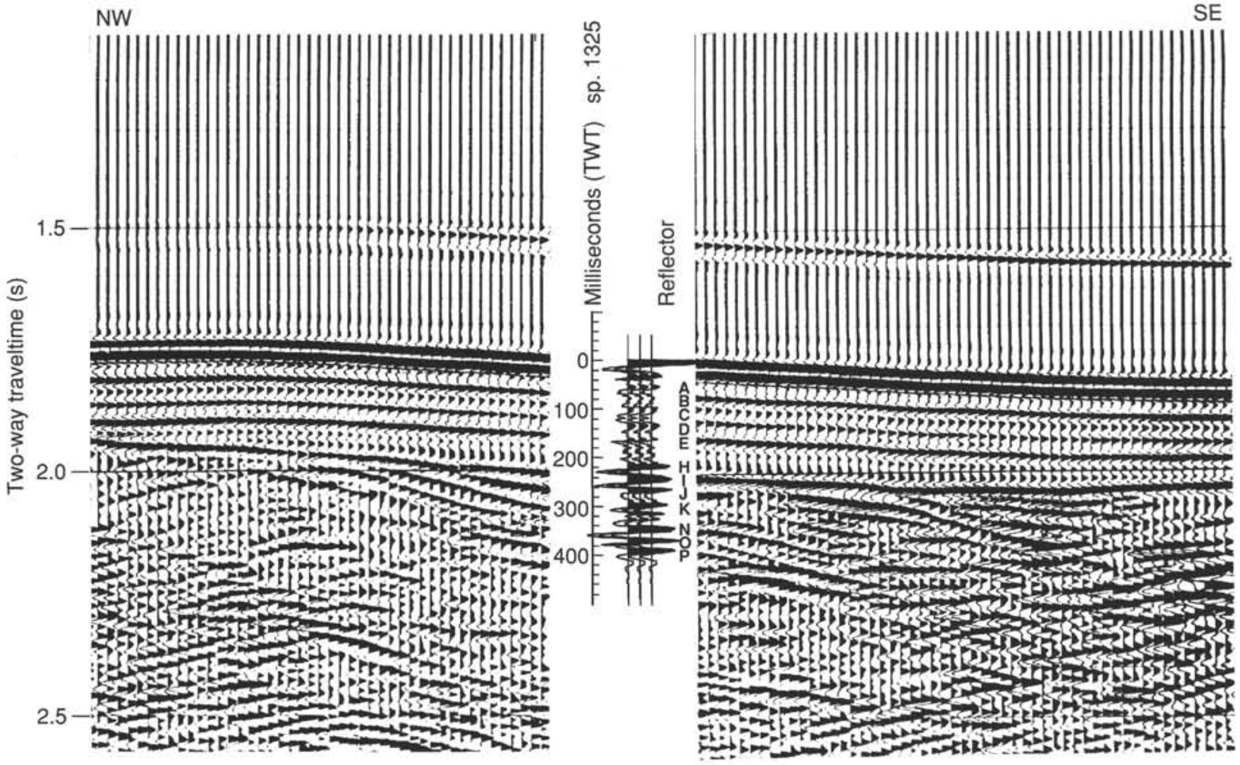

Figure 40. Comparison between synthetic seismogram from Site 908 and seismic section UB-24-81. The base of reflector H marks the unconformity between the detrital Pliocene sediments and the biosiliceous Oligocene sediments underneath (lithostratigraphic Unit I/II boundary).

SHORE-BASED LOG PROCESSING

Hole 908A

Bottom felt: 1284.5 mbrf (used for depth shift to seafloor)
Total penetration: 344.6 mbsf
Total core recovered: 313.96 m (91%)

Logging Runs

Logging string 1: DIT/DSI/NGT
Logging string 2: HLDT/CNTG/NGT
Logging string 3: FMS/GPIT/NGT (2 passes)

Wireline heave compensator was used to counter ship heave resulting from the mild sea state conditions.

Drill Pipe/Bottom-hole Assembly/Casing

The following drill pipe depths are as they appear on the logs after differential depth shift (see **Depth shift** section) and depth shift to the seafloor. As such, there might be a discrepancy with the original depths given by the drillers on board. Possible reasons for depth discrepancies are ship heave, use of wireline heave compensator, and drill-string and/or wireline stretch.

DIT/DSI/NGT: bottom of drill pipe at 77.5 mbsf.

HLDT/CNTG/NGT: bottom of drill pipe at 75 mbsf.

FMS/GPIT/NGT: bottom of drill pipe at 59.5 mbsf.

Processing

Depth shift: The FMS/GPI/NGT (main pass) was used as the reference run for depth shifting. All logs have also been depth shifted to the seafloor (–1284.5 m). A list of the amount of differential depth shifts applied at this hole is available upon request.

Gamma-ray processing*:* NGT data have been processed to correct for borehole size and type of drilling fluid.

Acoustic data processing: The data recorded with the DSI tool were adversely affected by the rugose nature of the borehole (see caliper data), and the compressional log was difficult to obtain. For this reason, only compressional and shear-wave data that show some correlation with other logs (i.e., the resistivity logs) can be considered reliable. Waveform processing is necessary to recover some of the invalid data recorded in the lower part of the hole.

Quality Control

Valid hole diameter measurements were recorded by the caliper on the HLDT tool (CALI), and the caliper on the FMS string (C1 and C2). As the HLDT caliper closed at 92 mbsf, any density measurement above that depth is suspicious, as no real-time correction for borehole size could be performed and because the tool was not making proper contact with the borehole wall.

Invalid gamma-ray readings were detected at 32, 55, 64, and 69 mbsf (HLDT/CNTG/NGT string).

Note: Details of standard shore-based processing procedures are found in the "Explanatory Notes" chapter, this volume. For further information about the logs, please contact:

Cristina Broglia
Phone: 914-365-8343
Fax: 914-365-3182
E-mail: chris@ldeo.columbia.edu

Elizabeth Pratson
Phone: 914-365-8313
Fax: 914-365-3182
E-mail: beth@ldeo.columbia.edu

Hole 908A: Resistivity-Velocity-Natural Gamma Ray Log Summary

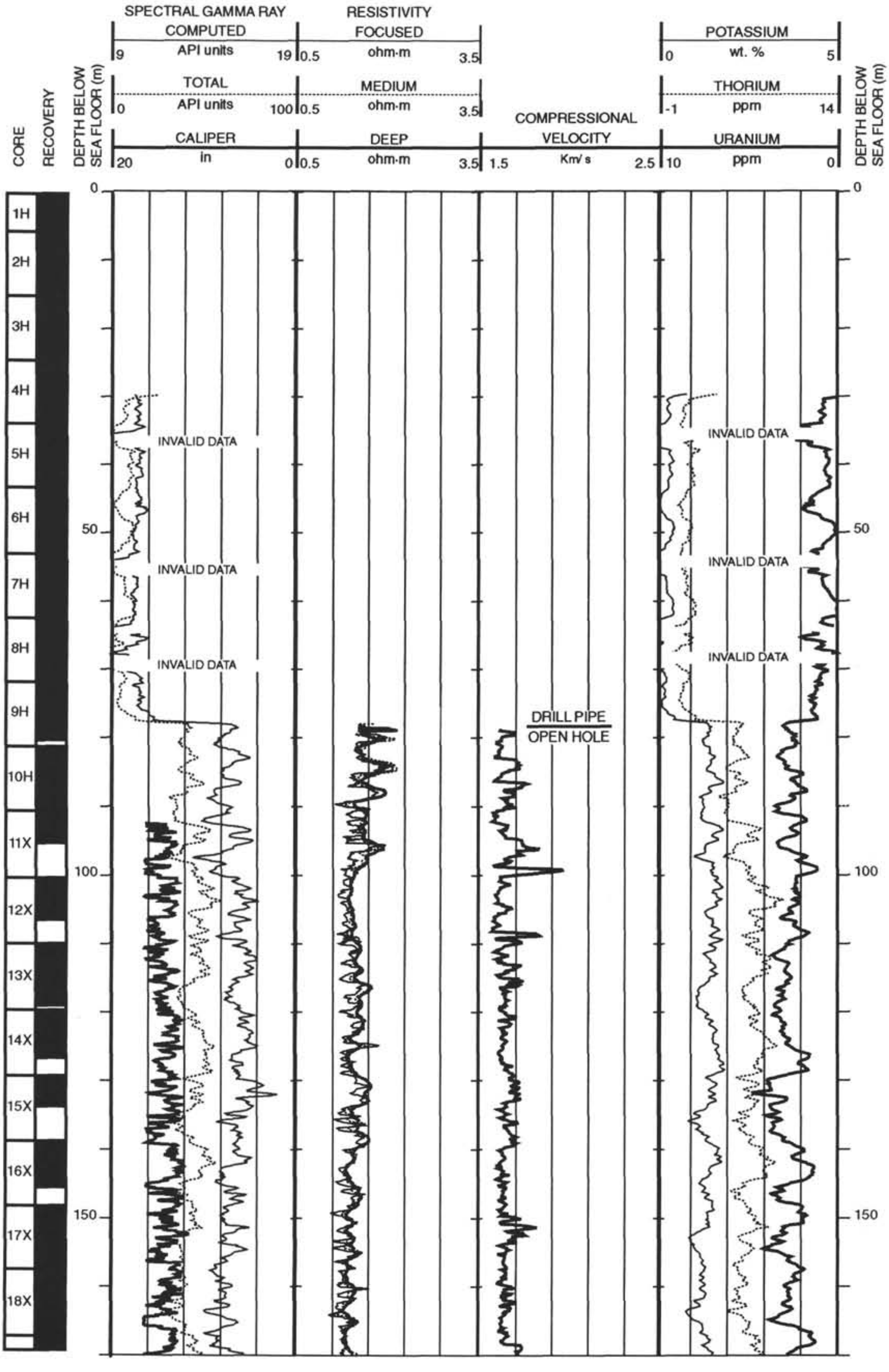

Hole 908A: Resistivity-Velocity-Natural Gamma Ray Log Summary

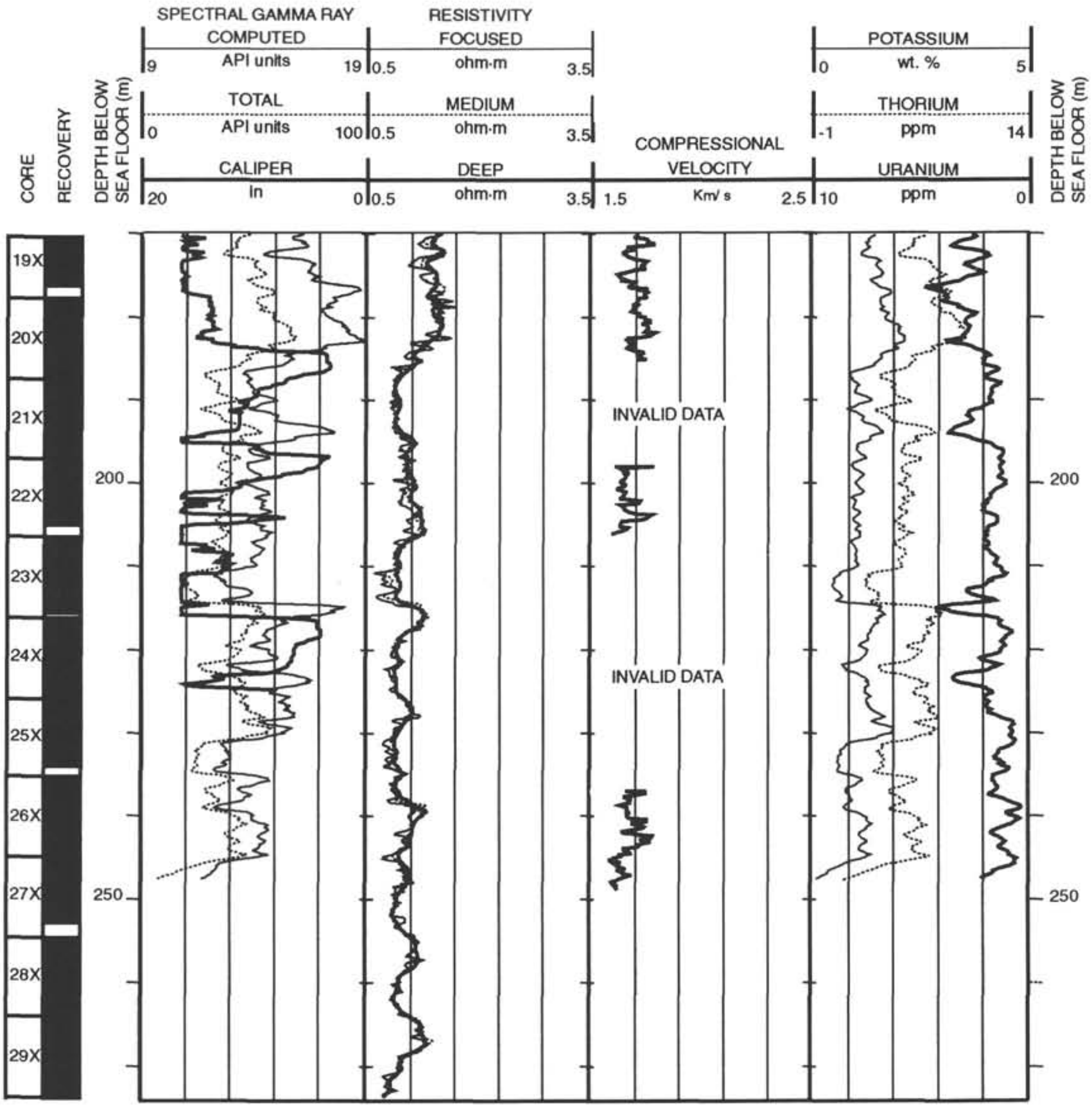

Hole 908A: Density-Porosity-Natural Gamma Ray Log Summary

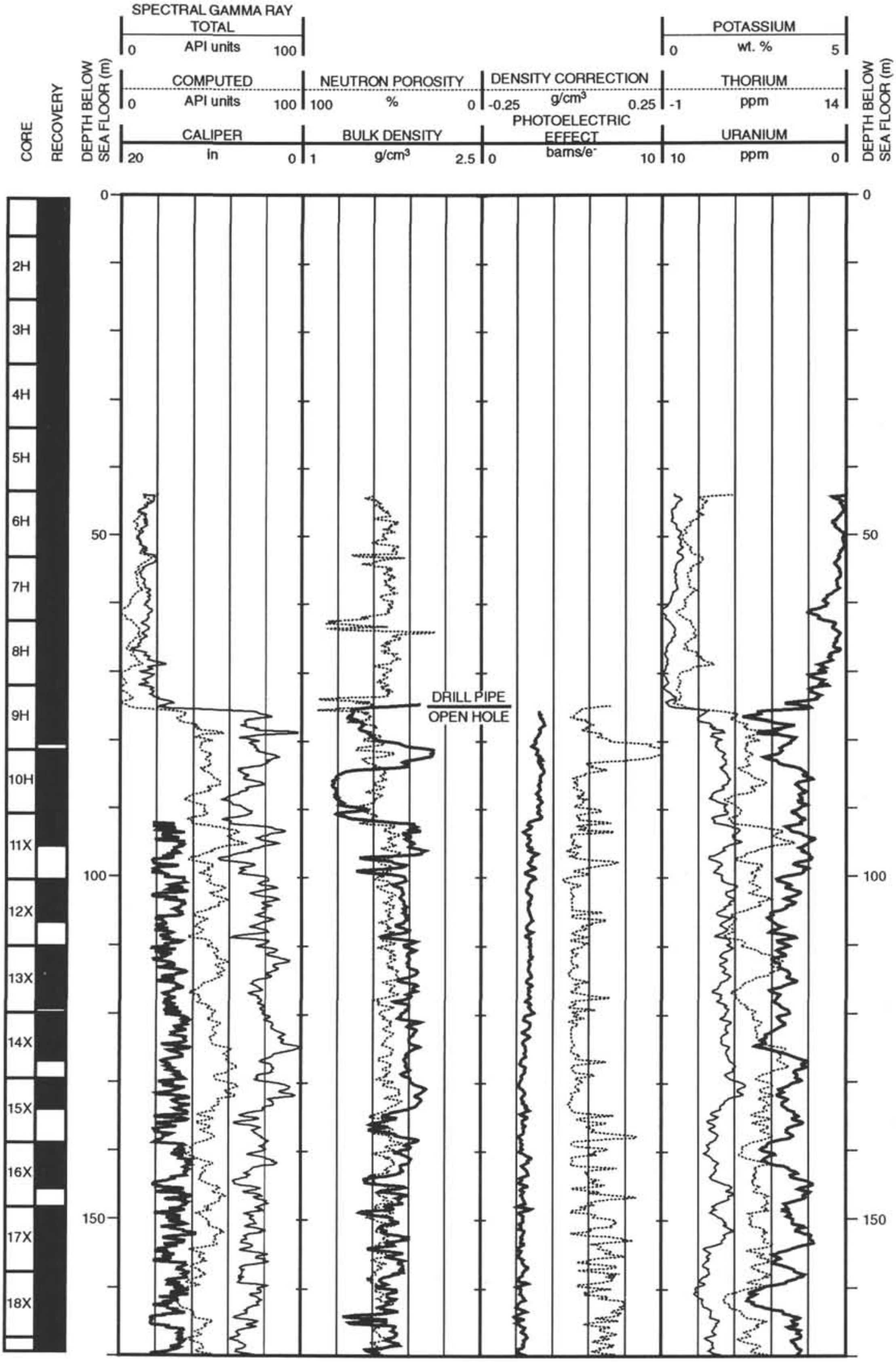

Hole 908A: Density-Porosity-Natural Gamma Ray Log Summary